UNIVERSITY OF OKLAHOMA

GRADUATE COLLEGE

OBSERVATION OF SINGLE TOP QUARK WITH ASSOCIATED Z BOSON PRODUCTION AT THE LARGE HADRON COLLIDER USING THE ATLAS DETECTOR

A DISSERTATION

SUBMITTED TO THE GRADUATE FACULTY

in partial fulfillment of the requirements for the

Degree of

DOCTOR OF PHILOSOPHY

By

DYLAN FRIZZELL
Norman, Oklahoma
2019

Downloaded from SHAREOK. Persistent Handle URL: https://hdl.handle.net/11244/322834

OBSERVATION OF SINGLE TOP QUARK WITH ASSOCIATED Z BOSON PRODUCTION AT THE LARGE HADRON COLLIDER USING THE ATLAS DETECTOR

A DISSERTATION APPROVED FOR THE
HOMER L. DODGE DEPARTMENT OF PHYSICS AND ASTRONOMY

BY THE COMMITTEE CONSISTING OF

Dr. Phil Gutierrez, Chair

Dr. Brad Abbott

Dr. Peter Barker

Dr. Chung Kao

Dr. Bruce Mason

© Copyright by DYLAN FRIZZELL 2019
All Rights Reserved.

I would like to dedicate the work that went into this dissertation to my family.
Mom, Dad, Jessy, Cooper, Poppy, Nanny, Papa H, and Memaw; I love you.

Acknowledgements

This work could not be accomplished without the guidance and support from my OU family. This group of people is the most supportive and caring colleagues I could have ever asked for. My adviser, Phil Gutierrez, has always given me the freedom to pursue my ideas and interests, and the support and guidance to make my dreams reality. Thank you Phil, without your help I could not have succeeded in performing this measurement, among countless other achievements. John Stupak is and always will be, a role model displaying how a successful high energy physicist should operate and collaborate. Mike Strauss is truly my friend. I will never forget sitting up and chatting about physics, politics, life, and family in the apartment. Brad Abbott is such a brilliant man and natural leader I speculate sometimes if he has the ability to read minds. Without Pat Skubic's lifetime of accomplishment and monumental achievement I have no doubt the OU HEP program would be a shadow of what it is today. I would like to give the largest gratitude I can offer to these five men.

I would also like to thank the OU HEP support staff: Horst Severini, Chris Walker, and Rusty Boyd for teaching me necessary technical skills, and facilitating my research. I would like to thank Muhammad Alhroob for helping me push the analysis through the finish line. I would like to thank Howie Baer and especially Chung Kao for teaching me practically everything I know about particle physics, and I would like to give a special thanks to two former OU graduate students: Hasib Ahmed and Othmane Rifki. Your guidance and thoughts on negotiating the world of HEP collaborations were the most helpful advice I may have ever received.

I would like to thank all of my Argonne family as well. Jessica Metcalfe, Sergei Chekanov, Doug Benjamin, Jinlong Zhang, Sasha Paramonov, Nancy Rezek, Larry Nodulman, Matt Zhang, Rui Wang, Jeremy Love, Tom LeCompte, and especially Bingxuan Liu. I would like to also give a distinguished thanks to my friend Jimmy Proudfoot. Your insight and guidance into the bigger picture of what is important was one of the most eye opening experiences of all of my time as a graduate student. You are one of the greatest leaders I have witnessed in my lifetime.

I would like to give an incredible thanks to my SWOSU family. Tony Stein, Terry Goforth, and especially Wayne Trail; you are responsible for corrupting me! Thank you. To Brad Bryant, who I called when I wanted to quit graduate school, thank you for teaching me how to deal with difficult people and become more self-aware.

And thank you to my CERN family. Ian Brock, Irina Cioara, Alex Sherman, Joseph Lambert, Marius Blaut, Chris Boever, and Tanja Holm: This work is not

mine but ours, and ours to share with all of ATLAS and the world. Thank you for your efforts and support throughout this process. I would like to give a special thanks to Lidia Dell'Asta in addition to these accolades. Your friendship will be one of my greatest memories of my time at CERN. I definitely could not have done this without you.

And lastly I have to thank my friends: Tom Weston, Francesco Di Bello, Blake Forland, and Valentina Vecchio. Thank god there is an ocean between us now, at least for a little while.

Table of Contents

List of Figures xix

List of Tables xxii

Abstract xxii

1 Introduction 1
- 1.1 Standard Model . . . 2
  - 1.1.1 Structure of the Standard Model . . . 2
  - 1.1.2 Electroweak Sector . . . 5
  - 1.1.3 Higgs Mechanism . . . 7
  - 1.1.4 Quantum Chromo-Dynamics . . . 10
  - 1.1.5 Proton Parton Distribution Function . . . 11
  - 1.1.6 Theoretical Prediction of tZq . . . 12
  - 1.1.7 Measurement Strategy . . . 18

2 Experimental Apparatus 19
- 2.1 The Large Hadron Collider . . . 19
- 2.2 A Toroidal LHC Apparatus (ATLAS) . . . 21
- 2.3 Inner Detector (ID) . . . 23
  - 2.3.1 Pixel Detector . . . 24
  - 2.3.2 Silicon Strip Detector . . . 27
  - 2.3.3 Transition Radiation Tracker . . . 27
- 2.4 Calorimetry . . . 29
  - 2.4.1 Electromagnetic Calorimetry . . . 30
  - 2.4.2 Hadronic Calorimetry . . . 31
- 2.5 Muon System . . . 32
  - 2.5.1 Muon Spectrometer and Toroid Magnets . . . 33
- 2.6 Trigger System . . . 34

3 Physics Object Definitions 35
- 3.1 Electrons . . . 36
- 3.2 Muons . . . 37
- 3.3 Jets . . . 38
  - 3.3.1 b-jets . . . 39
- 3.4 Missing Transverse Energy . . . 40
- 3.5 Overlap Removal . . . 40

4 Data and Monte Carlo 42
- 4.1 Data Sample . . . 42
- 4.2 Monte Carlo Simulation . . . 43
- 4.3 Signal Sample . . . 44
  - 4.3.1 tZq Production . . . 44
- 4.4 Background Samples . . . 45
  - 4.4.1 $t\bar{t}$ Production . . . 46
  - 4.4.2 Single top-quark Production . . . 47

4.4.3 $t\bar{t}H$ production . . . 48
4.4.4 $t\bar{t}V$ Production . . . 48
4.4.5 tWZ Production . . . 49
4.4.6 Diboson Production . . . 50
4.4.7 Z + jets Production . . . 51

5 Event Selection **52**
5.1 Full Event Reconstruction . . . 52
5.2 Signal Regions (SRs) and Their Relation to CR/VRs . . . 54
5.2.1 SRs Plots and Yields . . . 58
5.3 Control Regions . . . 60
5.3.1 Diboson CRs Plots and Yields . . . 61
5.3.2 $t\bar{t}Z$ CRs Plots and Yields . . . 64
5.3.3 $t\bar{t}$ CRs Plots and Yields . . . 66
5.4 Validation Regions . . . 68
5.4.1 $t\bar{t}$ VRs Prefit Yields . . . 68
5.4.2 Diboson VRs Prefit Yields . . . 69

6 Modeling Fake Leptons **71**
6.1 Fake Lepton Origin Studies . . . 71
6.2 *b*-jet Replacement Method . . . 73
6.2.1 BJR normalization . . . 77
6.2.2 BJR validation . . . 77
6.2.3 Shape comparison between various fake sources . . . 77

7 Multivariate Analysis **80**
7.1 Input variable distributions . . . 84
7.2 Neural-network output distributions in the SRs . . . 93

8 Systematic Uncertainties **95**
8.1 Sources of Systematic Uncertainty . . . 95
8.1.1 Object energy scale/resolution . . . 95
8.1.2 Monte Carlo and PDF modeling: . . . 98
8.1.3 Background rate uncertainty: . . . 99
8.1.4 BJR shape uncertainty: . . . 99
8.1.5 Luminosity . . . 101
8.1.6 Uncertainty on pile-up reweighting . . . 101
8.2 Symmetrizing, Smoothing, and Pruning . . . 101

9 Statistical Analysis **103**
9.1 Likelihood Function and Fitted Parameters . . . 103
9.2 Fitted Regions . . . 104
9.3 Fit Results . . . 105
9.4 Post-fit modeling in VRs . . . 115
9.5 Interpretation of Results . . . 117

10 Conclusion **118**

References **120**

A Signal Region Plots **129**

B $t\bar{t}$ Validation Regions Plots **135**

C Diboson Validation Regions Plots **141**

D *b*-jet Replacement Validation Plots **147**

E Supplemental Variable Definitions **152**

F Fit Results Material **153**

List of Figures

1.1 The Standard Model of particle physics classifies all known matter in the universe and models how it interacts. 3

1.2 Example proton PDF. 11

1.3 Feynman graphs to calculate the lowest order amplitudes. 14

1.4 Cross section calculation as a function of collision center of mass energy, $\sqrt{s}$. The dashed lines are leading order (LO) the solid are NLO. The top quark has a significantly higher cross section than the anti-top due to the higher multiplicity of up quarks in the proton. 17

2.1 The LHC is part of an intricate accelerator complex maintained and operated by CERN that has been the heart of over 50 years of experiments. 19

2.2 The ATLAS detector is comprised of several layers of sub-detectors specialized in different particle measurements. 22

2.3 The pseudorapidity is used to represent the polar angle in a way that provides a Lorentz invariant distribution. 23

2.4 The ATLAS inner detector provides tracking and vertex reconstruction. It is instrumental in providing energy measurements, b-tagging, and pileup suppression. The inner detector is comprised of three main sub-components: Pixels, SCT, and TRT. 25

2.5 The ATLAS inner detector by subsystem. 26

2.6 The ATLAS calorimeter system. 30

2.7 The EM calorimeter uses lead absorbing material fashioned in such a way to increase interaction cross section. 31
2.8 Fractional jet energy resolution uncertainty as a function of transverse momentum. 32
2.9 The magent system of the ATLAS detector. 33
2.10 The muon detector system provides additional measurements of charged particles that are able to traverse the entire ATLAS detector. 34

3.1 Different particle types can be reconstructed using specific signatures left in the ATLAS detector. 35
3.2 Hadronic jets originating from b hadrons typically exhibit a secondary vertex due to the longer lifetime of b hadrons relative to those with lighter quarks. 39

5.1 Summary of the analysis regions. The CR $t\bar{t}$ regions require a veto on the OSSF lepton pair. 56
5.2 Comparison of data and MC predictions for reconstructed event-related quantities for events in the SR-2j1b and SR-3j1b. The uncertainty shown is the backgrounds' modeling uncertainty. . . 59
5.3 Comparison of data and MC predictions for reconstructed event-related quantities for events in the CR-2j0b and CR-3j0b. The uncertainty shown is the backgrounds' modeling uncertainty. . . 63

5.4 Comparison of data and MC predictions for reconstructed event-related quantities for events in the CR-3j2b and CR-4j2b. The uncertainty shown is the backgrounds' modeling uncertainty. . . 65

5.5 Comparison of data and MC predictions for reconstructed event-related quantities for events in the CR-ttbar-TTT-2j1b and CR-ttbar-TTT-3j1b. The uncertainty shown is the backgrounds' modeling uncertainty. 67

6.1 Origin of the fake electrons in the $t\bar{t}$ sample. The fraction of the different sources is shown on the y-axis. The different signal, validation and control regions are shown on the x-axis. 73

6.2 Origin of the fake electrons in the $Z+$jets sample. The fraction of the different sources is shown on the y-axis. The different signal, validation and control regions are shown on the x-axis. The SR-3j1b region suffers from extremely low statistics. 74

6.3 Distribution of the energy vs. the the decay angle of leptons coming from b-hadron decays, in the rest frame of the b-hadron. 76

6.4 Comparison of data and MC predictions for reconstructed electron events in the SR-2(3)j1b-LTT. For further plots see Appendix D. 78

6.5 Comparison of shapes of different fake sources for $t\bar{t}$ (top) and $Z+$jets (bottom) events in 2jXb (left) and 3jXb (right) regions with three tight leptons. 79

7.1 Neural-network ROC curve of the training and test samples of the 2 jet SR (left) and of the 3 jet SR (right). The hashed curves are created from the training samples of each fold and the solid curves are created from the test samples. 84
7.2 Normalised kinematic plots of neural-network training variables of the 2j1b SR, in order of significance. "bjet_btagging" refers to the pseudo-continuous b-tagging score. 85
7.3 Normalised kinematic plots of neural-network training variables of the 2j1b SR, in order of significance. 86
7.4 Normalised kinematic plots of neural-network training variables of the 3j1b SR, in order of significance. 87
7.5 Normalised kinematic plots of neural-network training variables of the 3j1b SR, in order of significance. "bjet_btagging" refers to the pseudo-continuous b-tagging score. 88
7.6 Stacked kinematic plots of neural-network training variables of the 2j1b SR, in order of significance. "bjet_btagging" refers to the pseudo-continuous b-tagging score. 89
7.7 Stacked kinematic plots of neural-network training variables of the 2j1b SR, in order of significance. 90
7.8 Stacked kinematic plots of neural-network training variables of the 3j1b SR, in order of significance. 91

7.9 Stacked kinematic plots of neural-network training variables of the 3j1b SR, in order of significance. "bjet_btagging" refers to the pseudo-continuous b-tagging score. 92

7.10 Shapes of the NN output in the SRs, in the 2j1b SR (left) and in the 3j1b SR (right). 93

7.11 Output of the NN in the SRs, in the 2j1b SR (top) and in the 3j1b SR (bottom). The uncertainty shown contains all sources of statistical and systematic error. 94

8.1 Z + jets BJR shape uncertainty. 100

9.1 Analysis post-fit results of SR regions. 107

9.2 Analysis post-fit results of CR regions. 108

9.3 Estimate of the correlation matrix of all parameters in the fit that show a single correlation greater than 10%. 109

9.4 Analysis post-fit values of unconstrained normalization parameters. 110

9.5 Analysis post-fit 'γ' parameters associated with MC statistics. . 110

9.6 Ranking of each parameters impact on the POI. The pre- and post-fit impact of the parameter is shown via the blue bands, underneath its pull distribution. 111

9.7 Comparison of data and MC predictions for the most significant variables to the neural network in the SR-2j1b region using postfit values of fitted parameters. 113

9.8 Comparison of data and MC predictions for the most significant variables to the neural network in the SR-3j1b region using postfit values of fitted parameters. 114

9.9 Analysis post-fit results of VR regions. 116

A.1 Comparison of data and predictions for reconstructed lepton-related quantities for events in the 2j1b SR. The uncertainty shown is the backgrounds' modeling uncertainty. 129

A.2 Comparison of data and predictions for reconstructed jet-related quantities for events in the 2j1b SR.The uncertainty shown is the backgrounds' modeling uncertainty. 130

A.3 Comparison of data and predictions for reconstructed event-related quantities for events in the 2j1b SR. The uncertainty shown is the backgrounds' modeling uncertainty. 131

A.4 Comparison of data and predictions for reconstructed lepton-related quantities for events in the 3j1b SR. The uncertainty shown is the backgrounds' modeling uncertainty. 132

A.5 Comparison of data and predictions for reconstructed jet-related quantities for events in the 3j1b SR. The uncertainty shown is the backgrounds' modeling uncertainty. 133

A.6 Comparison of data and predictions for reconstructed event-related quantities for events in the 3j1b SR. The uncertainty shown is the backgrounds' modeling uncertainty. 134

B.1 Comparison of data and predictions for reconstructed lepton-related quantities for events in the 2j1b VR-ttbar. The uncertainty shown is the backgrounds' modeling uncertainty. 135

B.2 Comparison of data and predictions for reconstructed jet-related quantities for events in the 2j1b VR-ttbar.The uncertainty shown is the backgrounds' modeling uncertainty. 136

B.3 Comparison of data and predictions for reconstructed event-related quantities for events in the 2j1b VR-ttbar. The uncertainty shown is the backgrounds' modeling uncertainty. 137

B.4 Comparison of data and predictions for reconstructed lepton-related quantities for events in the 3j1b VR-ttbar. The uncertainty shown is the backgrounds' modeling uncertainty. 138

B.5 Comparison of data and predictions for reconstructed jet-related quantities for events in the 3j1b VR-ttbar. The uncertainty shown is the backgrounds' modeling uncertainty. 139

B.6 Comparison of data and predictions for reconstructed event-related quantities for events in the 3j1b VR-ttbar. The uncertainty shown is the backgrounds' modeling uncertainty. 140

C.1 Comparison of data and predictions for reconstructed lepton-related quantities for events in the 2j1Lb VR. The uncertainty shown is the backgrounds' modeling uncertainty. 141

C.2 Comparison of data and predictions for reconstructed jet-related quantities for events in the 2j1Lb VR.The uncertainty shown is the backgrounds' modeling uncertainty. 142
C.3 Comparison of data and predictions for reconstructed event-related quantities for events in the 2j1Lb VR. The uncertainty shown is the backgrounds' modeling uncertainty. 143
C.4 Comparison of data and predictions for reconstructed lepton-related quantities for events in the 3j1Lb VR. The uncertainty shown is the backgrounds' modeling uncertainty. 144
C.5 Comparison of data and predictions for reconstructed jet-related quantities for events in the 3j1Lb VR. The uncertainty shown is the backgrounds' modeling uncertainty. 145
C.6 Comparison of data and predictions for reconstructed event-related quantities for events in the 3j1Lb VR. The uncertainty shown is the backgrounds' modeling uncertainty. 146

D.1 Comparison of data and MC predictions for reconstructed electron events in the SR-2j1b-LTT. 148
D.2 Comparison of data and MC predictions for reconstructed electron events in the SR-3j1b-LTT. 149
D.3 Comparison of data and MC predictions for reconstructed muon events in the SR-2j1b-LTT. 150

D.4 Comparison of data and MC predictions for reconstructed muon events in the SR-3j1b-LTT. 151

F.1 The profiled likelihood curve as a function of the POI. 153

F.2 The pull distributions of all systematic uncertainty parameters. . 154

List of Tables

1.1 Eigenstates of unbroken electroweak fields for the first generation of the standard model. The higher generations have the same eigenvalues but differing masses. 6

1.2 Values of weak isospin and hypercharge for the Higgs fields. . . . 8

5.1 Object reconstruction. More details about the reconstruction process can be found in the text. 54

5.2 Overview of the requirements applied for selecting events in the signal, validation and control regions. The 'Loose' b-jet requirement means that one jet passes the 85 % efficient b-tagging working point requirement but does not pass the 70 % efficient working point. . 57

5.3 Numbers of expected events in the SR-2j1b (Left) and SR-3j1b (Right) broken down by process. The uncertainty shown contains only the statistical component. 58

5.4 Numbers of expected events in the CR-2j0b (Left) and CR-3j0b (Right) broken down by process. The uncertainty shown contains only the statistical component. 61

5.5 Numbers of expected events in the CR-3j2b (Left) and CR-4j2b (Right) broken down by process. The uncertainty shown contains only the statistical component. 64

5.6 Numbers of expected events in the CR-ttbar-TTT-2j1b (Left) and CR-ttbar-TTT-3j1b (Right) broken down by process. The uncertainty shown contains only the statistical component. 66

5.7 Numbers of expected events in the VR-ttbar-2j1b (Left) and VR-ttbar-3j1b (Right) broken down by process. The uncertainty shown contains only the statistical component. 68

5.8 Numbers of expected events in the VR-diboson-2j1Lb (Left) and VR-diboson-3j1Lb (Right) broken down by process. The uncertainty shown contains only the statistical component. 69

6.1 Definition of electron and muon selection criteria for "loose" and "tight". 72

7.1 Variables used as input to the neural-network of the 2j1b SR ordered by their importance. The 2nd column gives the correlation the loss function.*More detailed definitions of some variables in App. E.* . 81

7.2 Variables used as input to the neural-network of the 3j1b SR ordered by their importance. The 2nd column gives the correlation with the loss function.*More detailed definitions of some variables in App. E.* 82

9.1 Overview of the regions included in the fit. 105

9.2 Post-fit SR and CR yields. 106

9.3 Table of systematics' impact on the POI uncertainty grouped together based on origin. 112

9.4 Post-fit VR yields. 115

Abstract

The Standard Model of particle physics is the most well tested theory in modern physics. It provides the most fundamental description of the natural world using only a handful of particles and their interactions. At typical energies present at the Earth's surface, the Standard Model allows all of chemistry, electricity, magnetism, light, and even matter itself as we know it. At higher temperatures interesting things begin to happen: new particles begin to show themselves, forces appear to change, and completely new interactions can emerge. The Standard Model has successfully described everything we have encountered so far as we explore the dynamics of higher energy systems. As we continue to push into higher and higher energies the standard model also predicts what is yet to be observed. It is our job as scientists to search for and measure these predictions in hopes of someday finding something unexpected, and with it an opportunity to learn.

The top-quark is the heaviest known fundamental particle in the Standard Model, and the least studied of all the quarks. It's production at the Large Hadron Collider in association with a Z boson is a process predicted by the Standard Model that is only recently observable due to the achievement of modern experimental capacity. This thesis presents the observation and cross section measurement of such a process at the Large Hadron Collider using proton-proton collision data collected by the ATLAS experiment from 2015 to 2018 at a center-of-mass energy of $\sqrt{s} = 13\,\text{TeV}$, corresponding to an integrated luminosity of $139\,\text{fb}^{-1}$. Only the trilepton decay channel is considered, and events containing three identified

charged leptons (electrons and muons) two or three jets, one of which is identified as originating from a b-quark are selected. The major backgrounds mimicking this signal are from $t\bar{t}Z$, diboson, $t\bar{t}$ and $Z+$jets production. A series of Bayesian neural networks are used to improve the background rejection before extracting and measuring the signal using a binned maximum-likelihood estimator. The measured cross-section for $\mathrm{t}\ell^+\ell^- q$ production including non-resonant dilepton pairs with $m_{\ell\ell} > 30\,\mathrm{GeV}$ is $97 \pm 13\,(\mathrm{stat.}) \pm 7\,(\mathrm{syst.})\,\mathrm{fb}$. The statistical significance in favor of this processes' existence is estimated to be 9.1 σ. This directly matches the expected sensitivity of the analysis and surpasses the common benchmark 5 σ level of significance typically used to claim direct observation.

Chapter 1

Introduction

What makes up the universe and how do things interact so as to render the world seen today? The culmination of mankind's understanding of this question as of the 21st century is most succinctly portrayed in a mathematical model known as the Standard Model (SM) of particle physics. This model describes all known fundamental constituents of matter and how they interact within the framework of a quantum field theory. It is an effective model that despite its success is almost certainly incomplete due to its shortcomings on multiple fronts such as the lack of explanation for: the origin of neutrinos' mass, sufficient matter/anti-matter asymmetry in the universe, and seemingly unnatural tuning of the Higgs boson's mass [1, 2, 3, 4, 5]. The SM can be used to make predictions of interactions that are not yet observed but should exist if the model is valid. Testing these predictions gives insight into deeper understanding of the big questions about the universe, and provides hints into the physics beyond the standard model (BSM). This thesis is the result of careful search and measurement of such a prediction.

This chapter will outline the SM as a theoretical framework for making predictions of high energy collider experiments. Chapter 2 will present the [1]ATLAS detector and the Large Hadron Collider (LHC), which was the apparatus used to measure these predictions. Chapter 3 describes how fundamental physics objects are reconstructed from the detector information. Chapter 4 describes simulations

[1] **A** **T**oroidal **L**HC **A**pparatu**S**

used to model interactions inside the detector. Chapter 5 details the analysis strategy and procedure. Chapter 7 describes the multi-variate technique used. Chapter 8 includes systematic uncertainties evaluated for this thesis. Chapter 9 describes the statistical analysis and results. Chapter 10 interprets the implications of this result.

1.1 Standard Model

1.1.1 Structure of the Standard Model

The Standard Model is a quantum field theory formalized in its current recognizable form around the 1960s [6, 7, 8, 9, 10].

It is a theory of quantized fields existing in a 4 dimensional Minkowski space-time that exhibit local gauge invariance of internal symmetries of the group $SU(3)_{\text{color}} \times SU(2)_{\text{L}} \times U(1)_{\text{Y}}$. The $SU(3)_{\text{color}}$ gauge symmetry alone is referred to as Quantum Chromo-Dynamics (QCD) or strong interactions, and the $SU(2)_{\text{L}} \times U(1)_{\text{Y}}$ symmetries, along with influence from the Higgs potential [11, 12], describe electroweak interactions.

The particles of the standard model are shown in Fig. 1.1. Quarks and leptons are known as fermions and have a spin quantum number of 1/2. Force mediators are all bosons that have a spin quantum number of 1. Fermions carry quantum numbers for weak isospin and hypercharge and interact through the exchange of a photon via electromagnetic interactions and through the exchange of a W or Z boson via weak interactions. The quarks additionally carry a color charge

and can also interact via strong interactions mediated by the gluon. There are three "generations" of particles that behave similarly but have differing masses. For each standard model particle there exists an anti-matter partner that has opposite charge and parity (CP) quantum numbers typically denoted with "bar" notation, $\psi \rightarrow \bar{\psi}$.

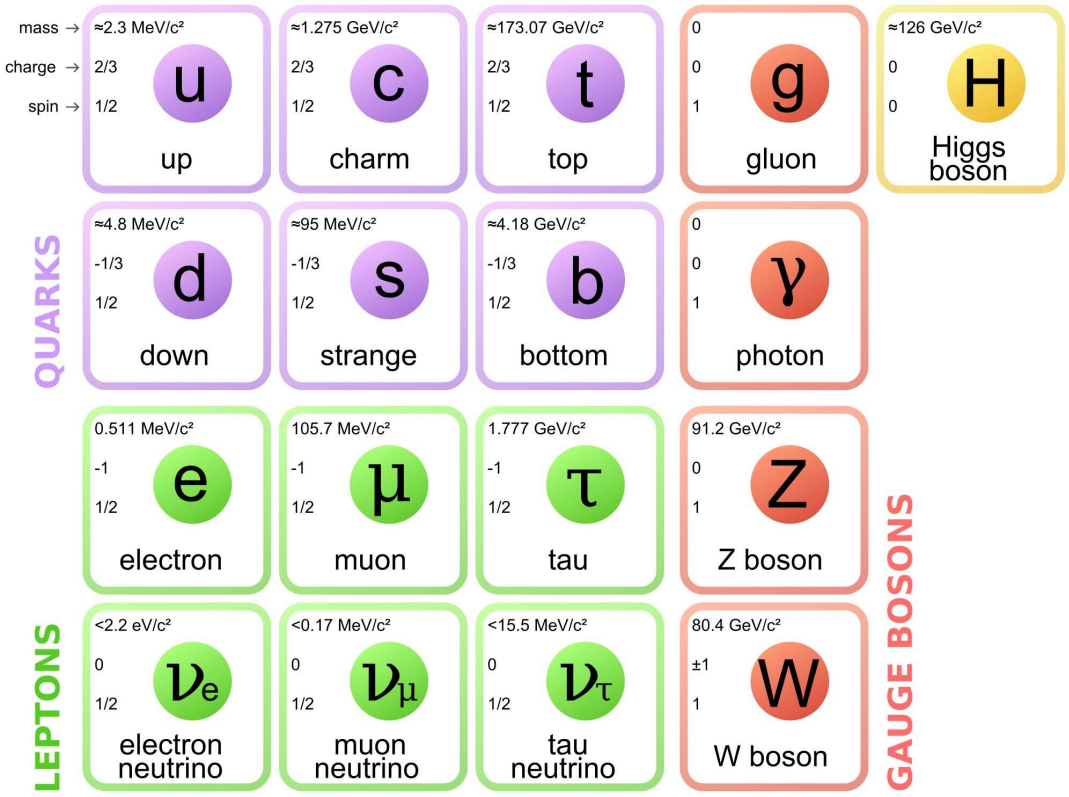


Figure 1.1: The Standard Model of particle physics classifies all known matter in the universe and models how it interacts.

The Higgs boson, which is a quantum of the Higgs field was recently discovered by both ATLAS and Compact Muon Solenoid (CMS) collaborations at the Large Hadron Collider (LHC) [13, 14]. It has no charge from gauge symmetries and no spin. The Higgs field is the cornerstone of the SM and its spontaneously broken

symmetry is the mechanism responsible for giving mass to the W and Z bosons as well as the fermions [11, 12].

1.1.2 Electroweak Sector

The electroweak portion of the standard model contains fermion fields that observe the symmetries $SU(2)_{\mathrm{L}} \times U(1)_{\mathrm{Y}}$. Left handed[2] fermions exhibit a chiral $SU(2)$ symmetry and are grouped in a doublet that transforms as

$$\Psi_L \rightarrow [1 - igT_k\alpha^k(x)]\Psi_L. \tag{1.1}$$

Where T_k are the group generators, α is the phase associated to an infinitesimal transformation, and g is the coupling strength. The transformation mixes the electron field with the neutrino field and the up with the down type quarks. Both the right and left handed fermions transform under the $U(1)_{\mathrm{Y}}$ transformation:

$$\Psi_{L,R} \rightarrow [1 - ig\prime Y\beta(x)]\Psi_{L,R}. \tag{1.2}$$

The fermions span a basis set with the quantum numbers shown in Table 1.1. The electric charge is defined as $Q = T_3 + \frac{1}{2}Y$. Neutrinos are the only known particles to exist only in left handed chiral states.

[2] "Left handed" refers to the chirality of the fermion field and determines whether the particles transforms via the right or left handed representation of the Poincaré group. For massless particles the helicity and chirality are functionally equal.

Fermion field	**Isospin**(T_3)	$\frac{1}{2}\times$ **Hypercharge**(Y)
ν_{eL}	$\frac{1}{2}$	-$\frac{1}{2}$
e_{eL}	-$\frac{1}{2}$	-$\frac{1}{2}$
u_L	$\frac{1}{2}$	$\frac{1}{6}$
d_L	-$\frac{1}{2}$	$\frac{1}{6}$
e_R	0	-1
u_R	0	$\frac{2}{3}$
d_R	0	-$\frac{1}{3}$

Table 1.1: Eigenstates of unbroken electroweak fields for the first generation of the standard model. The higher generations have the same eigenvalues but differing masses.

The unbroken electroweak Lagrangian for a single **massless** fermion field can then be shown as

$$\mathcal{L}_{EW} = -\frac{1}{4}W_m^{\mu\nu}W_{\mu\nu}^m - \frac{1}{4}B^{\mu\nu}B_{\mu\nu} + \bar{\Psi}i\gamma^\mu D_\mu \Psi. \tag{1.3}$$

W is the gauge field of the weak isospin, $SU\left(2\right)_{\mathrm{L}}$, B is of the hypercharge, $U\left(1\right)_{\mathrm{Y}}$, and the covariant derivative is expressed as

$$D_\mu = \partial_\mu + igW_\mu^m T_m + ig\prime\frac{1}{2}B_\mu Y. \tag{1.4}$$

This gives four degrees of freedom in the electroweak gauge bosons: one for each of the three $SU\left(2\right)_{\mathrm{L}}$ generators, and one for the weak hypercharge. The theory allows for self interactions of the gauge bosons due to the non-abelian part of the first term of the lagrangian. Linear superpositions of these gauge fields provide the physical force mediators observed in nature: $W^{\pm}$, Z, and γ,

which are responsible for the electric and weak forces. The angle of mixing of the W_3 and B fields into the Z and γ basis is an empirical parameter called the electroweak mixing angle, θ_W, and coupling constants are redefined according to this angle to give the couplings in terms of observables such as the electric charge, $e = g\ \sin\theta_W$ [15]. The $W^{\pm}$ interaction is unique in that it changes the flavor[3] of a fermion upon interaction. The top quark for example effectively always decays via this interaction into a W boson and a b quark.

1.1.3 Higgs Mechanism

The symmetries of the electroweak sector of the SM are spontaneously broken by a process known as the Higgs Mechanism [15]. This idea was suggested in 1964 by Higgs, Englert, and Brout [11, 12] and the idea was awarded the Nobel prize in 2013 after the observation of the Higgs boson, a predicted consequence of the Higgs field, was announced in 2012 by both the ATLAS and CMS collaborations [16, 17]. The Higgs mechanism adds an isodoublet of two complex fields to the lagrangian,

$$\Phi = \begin{pmatrix} \phi^+ \\ \phi^0 \end{pmatrix}, \tag{1.5}$$

with quantum numbers shown in Table 1.2.

[3] Up type quark to down type, or charged lepton to neutrino.

	T_3	$\frac{1}{2}Y$
ϕ^+	$\frac{1}{2}$	$\frac{1}{2}$
ϕ^0	$-\frac{1}{2}$	$\frac{1}{2}$

Table 1.2: Values of weak isospin and hypercharge for the Higgs fields.

These fields are added to the lagrangian, including square and quartic potential energy terms,

$$\mathcal{L}_{Higgs} = |D_\mu \Phi|^2 - \mu^2 |\Phi|^2 - \lambda |\Phi|^4. \tag{1.6}$$

The potential energy has a non-zero minimum expectation value, v, when μ^2 is negative which is conveniently expressed as $v/\sqrt{2} = (-\mu^2/2\lambda)^{\frac{1}{2}}$. Redefining the Higgs fields as displacements from the vacuum expectation value (vev) the symmetry is spontaneously broken and the Higgs doublet resembles

$$\Phi = \exp\left(\frac{i\zeta_m(x)\tau^m}{2v}\right) \begin{pmatrix} 0 \\ (v + H(x))/\sqrt{2} \end{pmatrix}. \tag{1.7}$$

where the $\boldsymbol{\zeta}$ fields are real fields with zero vev. Since the SM is symmetric under global gauge transformations, they can be applied to remove the overall phase factor and leave only the neutral component of the Higgs field non-zero in what is called the unitary gauge. These extra components effectively reappear when expanding the first term of Eq. 1.6 as a longitudinal component, and thus mass, of the $W^\pm$ and Z bosons [18, 19]. Due to the potential term, the Higgs boson also self-interacts causing the left out degree of freedom to manifest itself as a scalar massive neutral boson.

The leptons of the SM gain a mass term in the unitary gauge via interactions with the Higgs field through a Yukawa interaction

$$\mathcal{L}_{Yukawa} = -\frac{m_f\sqrt{2}}{v}[\bar{\psi}_{f,R}(\Phi^\dagger\Psi_{f,L}) + (\bar{\Psi}_{f,L}\Phi)\psi_{f,R}], \tag{1.8}$$

where the lepton and neutrino exist in a left handed doublet. There are no right-handed neutrinos in the SM, and as a consequence no neutrino masses or lepton flavor mixing. The value of the mass of each fermion is an empirical parameter. Unlike the mass of the W and Z bosons, the SM offers no understanding of the origin or relationship of these numbers.

The quarks also gain mass from similar Yukawa interactions from the Higgs field, but due to the existence of both right and left handed up and down type quarks the SM allows for generation mixing of the quarks. A more general parameterization of the quarks' Yukawa sector is used which includes these off diagonal terms in the Cabbibo-Kobayashi-Maskawa (CKM) matrix [20, 21]. The mass terms are, similar to the leptons, an empirical parameter.

The top quark is of particular interest due to its practically complete lack of generation mixing and its empirical mass that is two orders of magnitude larger than the other quarks, putting it closer to the mass of the massive bosons of the electroweak sector. It is the most massive particle in the SM and the only known fundamental particle heavier than the Higgs boson.

1.1.4 Quantum Chromo-Dynamics

QCD is a result of a $SU(3)$ non-Abelian gauge symmetry affecting quarks, and is mediated by particles known as gluons [22]. The Lagrangian density for the strong interaction is given by

$$\mathcal{L}_{QCD} = -\frac{1}{4} G_{A\mu\nu} G_A^{\mu\nu} + \sum_{i=\text{flavors}} \overline{q}_i \left(i \not{D} - m_i \right) q_i, \tag{1.9}$$

where the covariant derivative of QCD, D_μ, is defined as

$$D_\mu = \partial_\mu + i g_S \frac{\lambda_A}{2} G_{A\mu}. \tag{1.10}$$

where λ_A represents the eight group generators, G is the gluon gauge field, and g_S is the strong coupling constant, which is completely empirical. The quarks are charged with one of three color quantum states: red, blue, green, or their anticolors. The indices of the gluons, $A, B, C = 1, \cdots, 8$, correspond to the quantum states of the color-neutral gluon created by combining colors and anticolors. Because the gluon also carries a color charge, its field strength increases as the distance between two quarks grows. As a result of this, quarks exist only in bound, color neutral states known as hadrons.

A notable exception of this is the top quark which due to an extremely short lifetime decays via the weak interaction before hadronization [23, 24]. At extremely high energies the running coupling[4] $\alpha_S = \frac{g_S}{4\pi}$ becomes smaller, and as a result, the interaction between confined quarks decreases to the point that quarks behave as a free particle in scattering experiments like those used in proton-proton collision at

[4] As the energy of collisions increases, and thus the total energy transfered in the interaction, the fundamental charge effectively changes due to charge screening effects. To refer to the changing of this value as a function of energy transfer it is said the coupling "runs".

the LHC [15, 25]. When calculating scattering cross sections for hadron collisions, the probability of which partons participate in interactions are calculated and taken into account by parton distribution functions (PDFs) which are constructed from theoretical arguments along with heavy influence from experiments [26].

1.1.5 Proton Parton Distribution Function

The measurement contained in this thesis relies on predictions made to describe high energy proton-proton collisions.

Because of the composite structure of the proton, as well as the presence of QCD radiation, a common technique is used to calculate the momentum density of different interacting initial state particles eligible for interaction. This includes not only the valence u and d quarks that comprise the proton itself, but also radiating gluons and short lived heavy quarks present from gluon splitting.

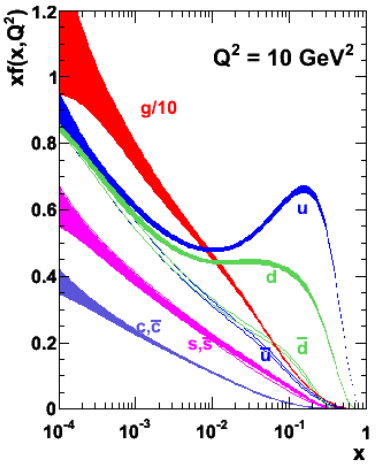


Figure 1.2: Example proton PDF.

These so called parton distribution functions (PDFs) are based on theoretical arguments but rely heavily on input from experiment for empirical parameters [27]. An example PDF (MSTW08 PDF) taken from Ref. [28] illustrates the distribution of probability for a parton with momentum fraction x of a high energy proton to partake in an interaction with momentum transfer Q^2 is shown in Fig. 1.2. This

probability is taken into account when predicting the number of expected events at the LHC as demonstrated in chapter 5 of Ref. [15].

For the purpose of this thesis two broad categories of PDFs are discussed: (four-flavor scheme) 4FS and (five-flavor scheme) 5FS. This refers to the number of initial state partons considered in the PDF. The 4FS includes in the distribution gluons and u, d, c, and s quarks. The 5FS also includes the b quark which is an important initial state parton in the tZq process. All partons in the PDFs used in this thesis are approximated to be massless.

1.1.6 Theoretical Prediction of tZq

The SM can be used in the QFT perturbative framework to calculate scattering cross sections of interactions of all known fundamental particles, including the production cross section for a top quark associated with a Z boson, tZ, from proton-proton collisions which is the topic of this thesis [29]. In the context of a theoretical prediction, tZ refers to production of both top and anti-top quark collectively. tZ is a very well motivated production cross section to be measured at the LHC for multiple reasons with some of the most important being:

- The tZ process is predicted by and should be measured in order to further validate the SM.
  - The tZ production cross section has a very precise prediction at the LHC [30]. The tZ cross section depends crtically on two SM parameters: the charge of the electron, and the weak mixing angle. These two

SM parameters are known to great precision allowing practically all theoretical uncertainty to come from the parameterization of QCD hadronization in the form of the renormalization and factorization scales (μ_r,μ_f)[5], therefore any measured deviation from prediction indicates contributions from nown physical processes [31, 32, 33, 34, 35].

- the tZ process is an important background for a future tH measurement that should have its existence verified and its modeling validated before a tH measurement is pursued [35].
  - tH is a very interesting process in its own right which probes the top quark Yukawa coupling but is beyond the scope of this thesis.
- the tZ process is also an important background for precision ttZ and ttW measurements. The uncertainty on its cross section will be an important systematic uncertainty for measuring other rare processes in the top sector as part of a larger campaign of testing the top sector of the SM [36].
- The tZ process is extremely sensitive to what is known as flavor changing neutral currents (FCNC), which is a forbidden phenomenon in the SM. Essentially the transition from $t \rightarrow (c, u)$ through emission of a neutral Z boson instead of the typical $t \rightarrow b$ through emission of a charged $W^{\pm}$ due to some BSM contribution would greatly enhance the measured tZ cross section, making this measurement a prime target for indirect searches for

[5]The renormalization scale is the value at which the running coupling is evaluated. The factorization scale is similar but deals with calculations handling initial state gluon radiation.

new physics [37].

- It is a useful channel to measure for future effective field theory (EFT) interpretations [38].

At the LHC the production of tZ is accompanied by the existence of an additional spectator quark in the final state: $\mathbf{tZq}$. This is because the LHC is primarily a proton-proton collider and the tZq process is dominated almost entirely by t-channel[6] interactions. This requires the initial state interaction is quarks or gluons, and one of the initial quarks survives to the final state as shown in Fig. 1.3.

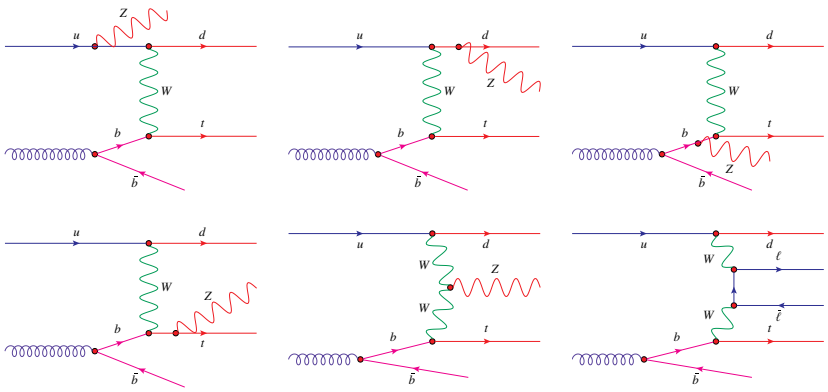


Figure 1.3: Feynman graphs to calculate the lowest order amplitudes.

The production of tZq at the LHC begins in the initial state with an $u(d)$ quark from within a proton scattering off of a $b(\bar{b})$ quark created from a gluon splitting that was emitted from the other proton in the collision. The charged weak interaction of this $b(\bar{b})$ quark produces the $t(\bar{t})$ quark. The associated Z boson

[6] In particle physics the propagator of QFT interactions is relativistically classified as space-like, s channel, or time-like, t- and u-channel.

is then either radiated from any quark in the interaction, or more preferentially, from the $W^+(W^-)$ boson t-channel propagator.

The $t(\bar{t})$ quark will decay via a $W^+(W^-)$ boson and a $b(\bar{b})$ quark. The $W^+(W^-)$ boson will then further decay into two quarks or into a lepton and neutrino. The Z boson will decay, at leading-order (LO), in a CP conserving way into either a quark/anti-quark or lepton pair of the same generation. Because the measurement of $\mathrm{tZ}q$ will require the distinguish-ability of this process from other background processes, **this thesis will only consider decay channels that provide three leptons** which have less background contamination and better energy resolution of the detected leptons, see Section 2.2.

To further accommodate the concern of quantum interference of non-resonant contributions, the process simulated and measured at the LHC is $\mathrm{t}\ell^+\ell^- q$ where the Z boson is forced to decay leptonically and these contributions are included. This includes possible quantum interference between Feynman diagrams containing a real Z boson and those with a lepton propagator as shown in the last diagram of Fig. 1.3.

The most accessible final state for trilepton $\mathrm{t}\ell^+\ell^- q$ is one light quark, one $b(\bar{b})$ quark, three leptons two of which must come from the same generation (or flavor) with opposite sign to reflect the presence of the Z boson, and noticeable energy imbalance resulting from the undetected neutrino from the W boson decay. The other bottom type quark from the gluon splitting typically has very low energy, and as a result has a direction of travel nearly parallel with the collision axis and goes undetected.

The theoretical calculation is presented by Campbell, Ellis, and Röntsch at next to leading order (NLO) and more recently approximated at next to next to leading order (NNLO) by Kidonakis [35, 30]. The results from the former are shown in Fig. 1.4. The total expected cross section for $\mathrm{tZ}q$ at the LHC running at 13 TeV is around 800 fb. After applying the branching ratio to the trilepton final state [34], the $\mathrm{t}\ell^+\ell^-q$ cross section is ∼100 fb. This predicts that over the entire time that the LHC has been running at 13 TeV (2015-2019) only about 14,000 events have been produced within the ATLAS detector. This is incredibly small when one considers that just one of the background processes, $t\bar{t}$, will occur more than 10 million times! More detailed information on the cross section, event generation, and simulation of $\mathrm{t}\ell^+\ell^-q$ and its backgrounds is given in Section 4.3. **Due to the fact that this thesis targets a $\mathrm{t}\ell^+\ell^-q$ signature that exhibits an overwhelming majority of events containing an on-shell real Z boson, the process described in this section will be referred to by its more colloquial "$\mathrm{tZ}q$" throughout this thesis with the exception of Section 4.3.1 which describes the simulated sample in detail.**

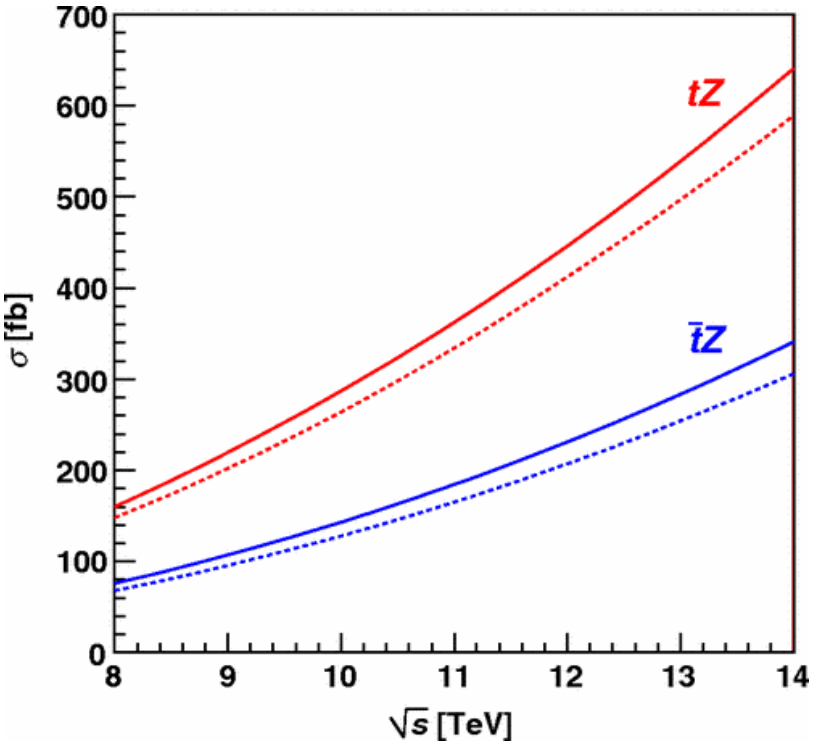


Figure 1.4: Cross section calculation as a function of collision center of mass energy, $\sqrt{s}$. The dashed lines are leading order (LO) the solid are NLO. The top quark has a significantly higher cross section than the anti-top due to the higher multiplicity of up quarks in the proton.

1.1.7 Measurement Strategy

In order to test the prediction of the standard model, the trilepton final state of $\mathrm{tZ}q$ is examined and simulated. All background processes that mimic the signature of $\mathrm{tZ}q$ are also simulated and taken into account. Selection requirements are used to maximize the ratio of signal to background events examined. Control and validation regions with similar kinematics are used to ensure the background modeling is accurate and robust. To increase sensitivity to the $\mathrm{tZ}q$ signal, a Bayesian neural network is used to further separate signal from background events. Once the modeling is satisfactory the simulated number of expected events is compared to data. The comparison is then analyzed via the framework of a binned maximum-likelihood estimator with a free floating parameter of interest that varies the total normalization of the $\mathrm{tZ}q$ yield. The result of this statistical analysis is used to extract the cross section of the $\mathrm{tZ}q$ process.

Chapter 2

Experimental Apparatus

2.1 The Large Hadron Collider

The LHC is the largest machine ever built by mankind [39]. It is a superconducting synchrotron constructed in a circle with approximate circumference of 27 km. The main synchrotron is roughly 100m underground beneath the border of France and Switzerland and operated by Conseil Européen pour la Recherche Nucléaire (CERN).

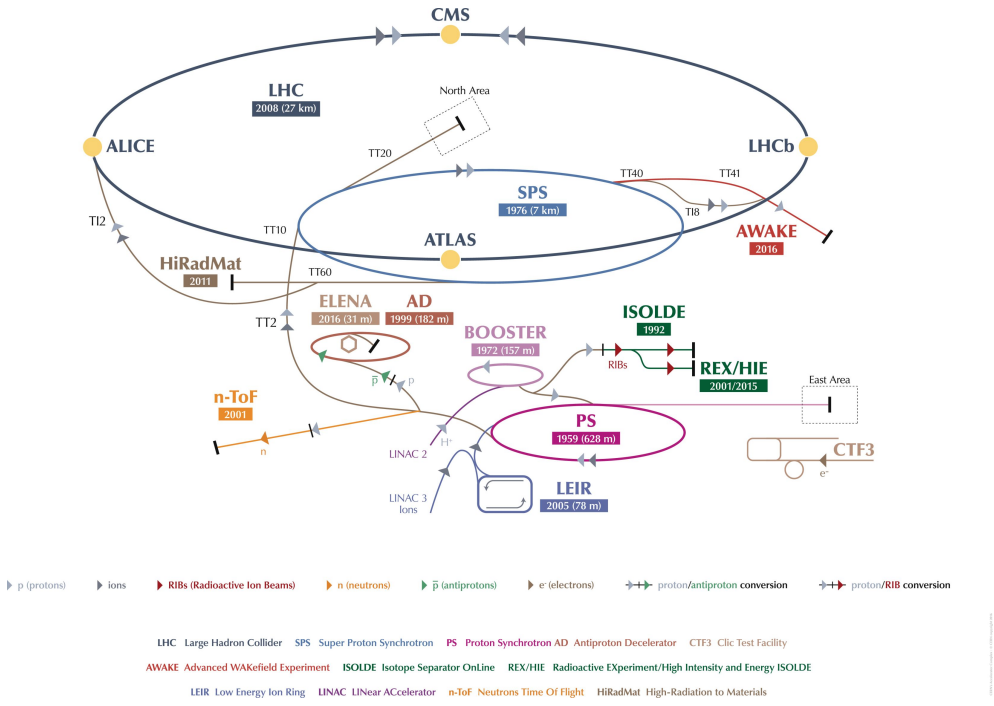


Figure 2.1: The LHC is part of an intricate accelerator complex maintained and operated by CERN that has been the heart of over 50 years of experiments.

The LHC uses superconducting dipole magnets cooled to -271.43^{o} C with a field strength of $\sim$8 Tesla to steer two beams of hadrons, typically protons, in opposite directions inside of a vacuum pipe at pressure of 10^{-10} mbar, and allow them to collide at four designated collision points at four main detectors of the LHC: ATLAS [40], CMS [41], LHCb (Large Hadron Collider Beauty) [42], and ALICE (A Large Ion Collider Experiment) [43].

Protons for multiple CERN experiments from 1978 until its recent decomission in 2018, were initially accelerated through the Linac2 linear accelerator [44]. For scattering experiments at the LHC, the protons' energy is progressively increased as they travel from the Linac2, the PS Booster, the PS, the SPS, and finally the LHC itself where they reach a final maximum energy of 6.5 TeV. The protons are equally spaced in 2808 bunches that are about 30 cm long. The bunches of each beam are focused by quadrapole magnets to a diameter of 16 μm before crossing every 25 nanoseconds (50 ns in 2015) at the four designated interaction points, generating approximately 600 million collisions per second.

The rate of expected events of any given particle physics process or interaction is estimated by

$$\frac{dN}{dt} = \sigma\mathcal{L}, \tag{2.1}$$

where σ is the theoretical cross section that and $\mathcal{L}$ is the instantaneous luminosity of the beam, which is defined as the number of particles passing through a given area per second. The total luminosity over some given time is referred to as the integrated luminosity, L, and is used to estimate the number of events with a

given cross section should occur during that time. It is easy to see that luminosity is a crucial parameter of experiments at the LHC. Primarily the instantaneous luminosity is periodically measured via Van der Meer scans, and for ATLAS data taking, luminosity measurements are also performed using the LUCID-2 sub-detector [45, 46]. Combining all possible measurements, the total integrated luminosity over Run 2 (2015-2018) has been measured to be 139 fb^{-1} with an uncertainty of 1.7% [47].

2.2 A Toroidal LHC Apparatus (ATLAS)

The ATLAS detector, shown in Fig. 2.2, at the LHC covers nearly the entire solid angle around the collision point and was originally designed to search for and measure properties of the Higgs boson, as well as search for indications of BSM physics [48]. It is about 7000 tons, twenty-five meters in diameter, and forty-four meters long. It is generally cylindrical in shape and is the largest detector of its kind ever built. It consists of an inner tracking detector surrounded by a thin superconducting solenoid, electromagnetic and hadronic calorimeters, and a muon spectrometer incorporating three large superconducting toroidal magnets. The inner-detector system (ID) is immersed in a 2 T axial magnetic field and provides charged-particle tracking in the range $|\eta| < 2.5$.

ATLAS uses a right-handed coordinate system with its origin at the nominal interaction point (IP) in the center of the detector and the z-axis along the beam pipe. The x-axis points from the IP to the centre of the LHC ring, and the y-axis

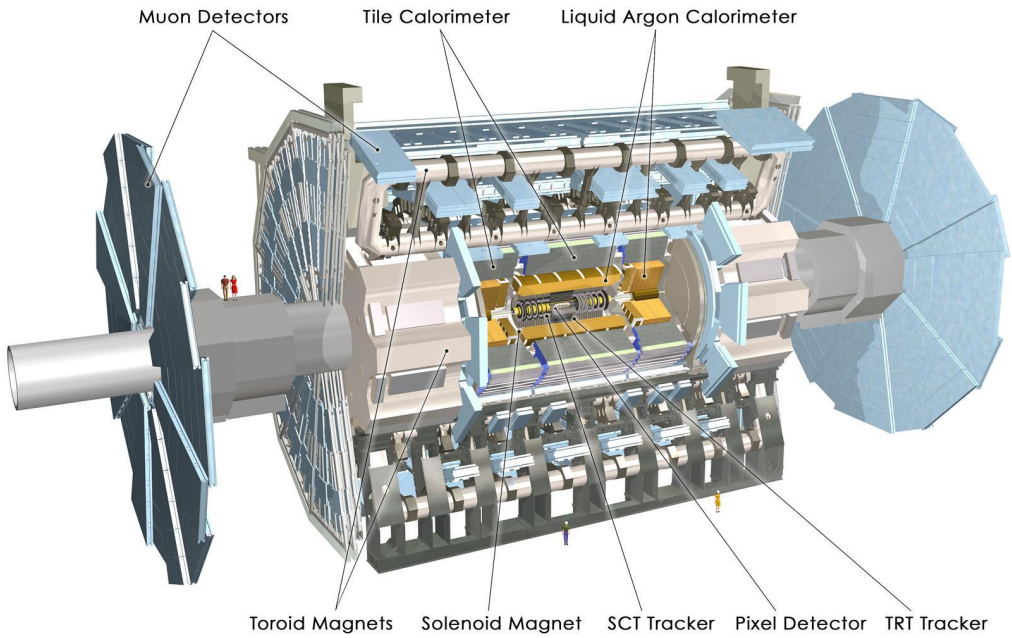


Figure 2.2: The ATLAS detector is comprised of several layers of sub-detectors specialized in different particle measurements.

points upwards. Cylindrical coordinates (r, ϕ) are used in the transverse plane, ϕ being the azimuthal angle around the z-axis. The pseudorapidity (η) is used to represent the polar angle so that Lorentz invariant distributions can be achieved, Fig. 2.3. It is defined in terms of the polar angle θ as $\eta = -\ln\tan(\theta/2)$. Angular distance is measured in units of $\Delta R \equiv \sqrt{(\Delta\eta)^2 + (\Delta\phi)^2}$.

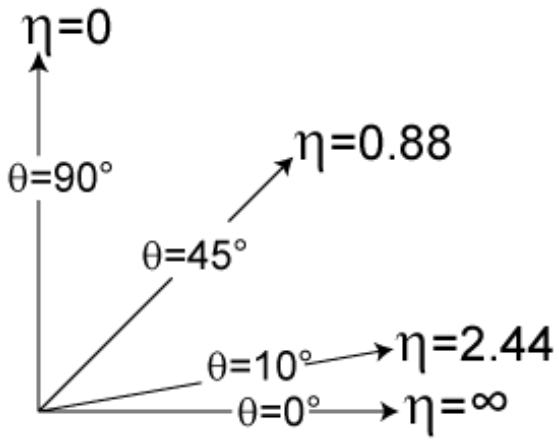


Figure 2.3: The pseudorapidity is used to represent the polar angle in a way that provides a Lorentz invariant distribution.

2.3 Inner Detector (ID)

The ATLAS inner detector is comprised of silicon pixels, strips, and a gaseous transition radiation detector that each record a position measurement of a charged particle as it passes through the ID. The silicon detectors use small reverse biased $p-n$ junctions of differing geometries that a traversing charged particle will deposit charge into. This charge is then amplified and discriminated against a known calibration to provide binary occupancy information. The gas-filled tube detectors use an ionizable gas that creates a cascade of ions when a charged

particle passes through it. These ions are then collected by an axial charged anode wire down the center of the gas tube. The drift velocity of the cascade decay can be used to estimate the radial distance the traversing particle is from the central anode of each tube. A cross section of the barrel portion of the ID is shown in Fig. 2.4.

The function of the inner detector is to provide track reconstruction of charged particles' trajectory by systematically combining position measurements. The solenoidal magnetic field present in the ID allows the momentum of a detected charged particle to be inferred. The relative momentum resolution for charged particles is measured to be a function of the transverse momentum of the track: $\sigma_p/p = (4.83 \pm 0.16) \times 10^{-4}\ \text{GeV}^{-1} \times p_T$ [49]. For this thesis typical momentum resolutions are less than 0.5%. Reconstructed tracks can also be used to reconstruct interaction vertices. This tracking and vertexing is mandatory for providing good overall energy measurement, identification of b-jets (Chapter 3.3.1), and suppressing the influence of particles originating from sources other than the primary vertex of interest (pileup). The ATLAS ID is planned to be replaced in 2026 by an all silicon tracking detector, the Inner TracKer (ITK) with extended $|\eta|$ coverage and increased granularity [50].

2.3.1 Pixel Detector

The high-granularity silicon pixel detector covers the vertex region and typically provides four measurements per track, the first hit being normally in the insertable B-layer (IBL) installed before the start of Run 2 [51, 52, 53]. The pixel detector

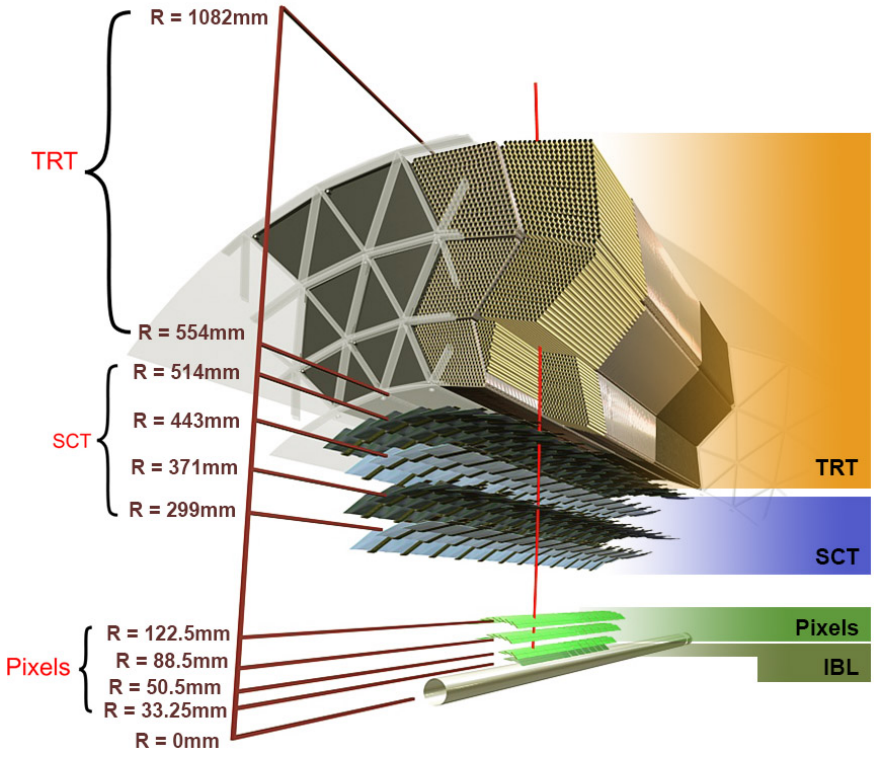


Figure 2.4: The ATLAS inner detector provides tracking and vertex reconstruction. It is instrumental in providing energy measurements, b-tagging, and pileup suppression. The inner detector is comprised of three main sub-components: Pixels, SCT, and TRT.

gives a 3-dimensional measurement of the location of a charged particle as it travels outward from the interaction point (IP). Each pixel has dimensions of 50 μm (Rϕ) $\times$ 400 μm (z) except for the pixels of the IBL which are 50 μm (Rϕ) $\times$ 250 μm (z) which combined equates to over 90 million readout channels. Using sophisticated tracking algorithms, trajectories to the IP can be reconstructed with a precision of 10 μm (Rϕ) $\times$ 115 μm (z) for typical particle tracks. The pixel detector is comprised of cylindrically symmetric layers covering the $|\eta|$ range of 0 to 1.4 and discs that extend coverage to $|\eta|$ of 2.5, see Fig. 2.5. The pixel detector is subject to the highest levels of radiation of all ATLAS components with the IBL designed to accommodate over $10^{15} n_{eq}/cm^2$ non-ionizing energy loss (NIEL), where n_{eq}/cm^2 is the equivalent flux from neutron radiation.

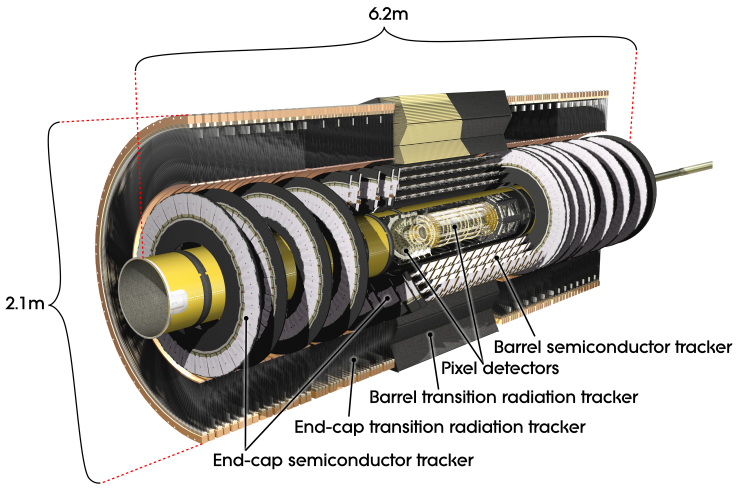


Figure 2.5: The ATLAS inner detector by subsystem.

2.3.2 Silicon Strip Detector

Moving radially out from the pixel detector, the next layer of the ATLAS detector is the silicon microstrip tracker (SemiConductor Tracker, SCT) which provides up to eight measurements per track which are used in their reconstruction. Each of the four SCT detector layers is comprised of two silicon strip sensors 80 μm $\times$ 6.4 cm that are rotated 40 mrad relative to one another in order to extract a z dimension. Each layer can provide position resolution of 17 μm in r - ϕ and 580 μm along the z axis. The SCT barrel layers and discs combined have a coverage of up to $|\eta| = 2.5$ [54].

2.3.3 Transition Radiation Tracker

The silicon detectors are complemented by the transition radiation tracker (TRT) which is the inner detector component furthest from the IP which is comprised of approximately 30,000 gas-filled[1], 4 mm in diameter straw tube detectors [55, 56, 57]. The TRT is comprised of a barrel and radial extension components that provide a ϕ measurement of charged particles trajectory in the range of $|\eta| < 1.0$ and $1.0 < |\eta| < 2.0$, respectively. As charged particles traverse the gas detector, ionization of the gas occurs. A potential difference between the outer circumference of the straw tube and an axial gold-plated tungsten wire causes electrons to drift toward the anode wire. This drift time is used to infer the radius of the charged particle from the center of the tube and thus measure its position. The single point resolution of the TRT for a typical reconstructed track is $\sim$130 μm per

[1]The gas mixture used in the TRT is nominally 70% Xe, 27% CO_2 and 3% O_2

straw. The space between the different detector tubes is filled with polymer fiber material that stimulates the emissions of soft X-rays when relativistic particles traverse the detector, particularly when transitioning through material boundaries. This transition radiation effect is most prevalent in electrons, which allows the TRT to provide pion/electron discrimination information.

2.4 Calorimetry

The ATLAS calorimeters are made up of two types of sampling calorimeters where incident particles interact with an absorbing material and create a shower of subsequent electromagentic radiation in the active medium: liquid argon (LAr) or scintillating tiles. A fraction of the energy produced by the incident particle's shower is measured by active detector sensors. After carefully calibrating the calorimeter, the energy of the full shower created by the incident particle can then be inferred. Calorimeter cells are divided up into sections of η and ϕ and are designed to completely contain all emitted electromagnetic and hadronic matter of collisions at the projected maximum center-of-mass energy of the LHC, 14 TeV. The entire calorimeter system covers the pseudorapidity range $|\eta| < 4.9$.

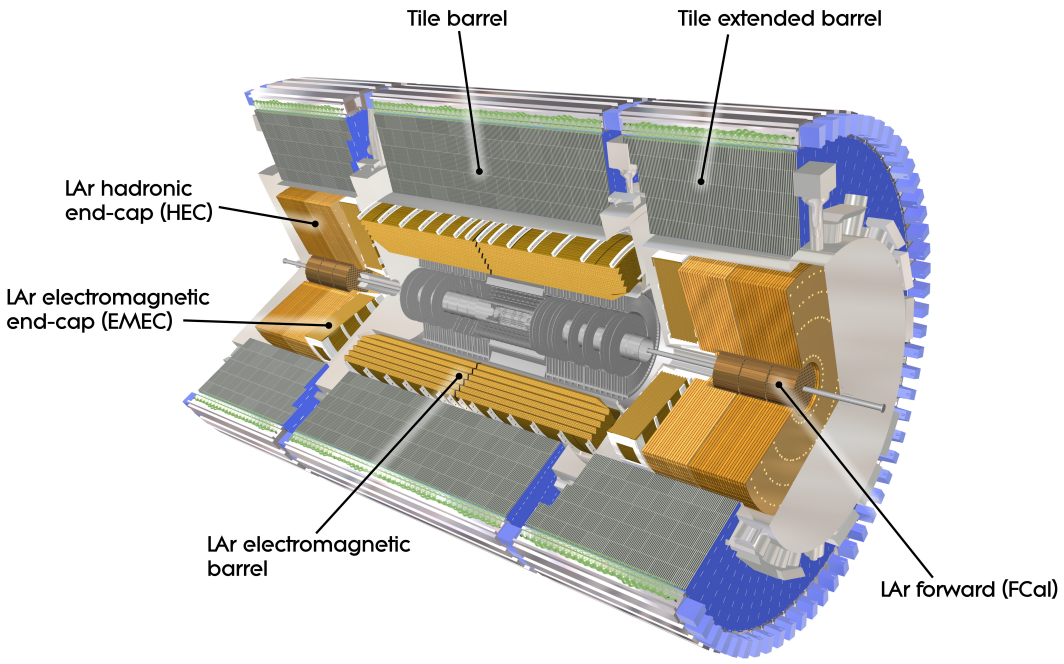


Figure 2.6: The ATLAS calorimeter system.

2.4.1 Electromagnetic Calorimetry

Within the region $|\eta| < 3.2$, electromagnetic (EM) calorimetry is provided by barrel and endcap lead/liquid-argon (LAr) calorimeters shown in Fig. 2.7, with an additional thin LAr presampler covering $|\eta| < 1.8$, to correct for energy loss in material upstream of the calorimeters. The calorimeter geometry is granulated into sections ranging from 0.003×0.025 in $\eta \times \phi$ in the central barrel to 0.1×0.1 in the furthest endcap layers. The EM calorimeter primarily measures the energy of electrons and photons as they traverse the ATLAS detector with an uncertainty of 2-4% [58]. Because electrons have a shorter interaction length[2]

[2]Interaction length is the distance a particle must travel in a medium to decrease its energy by a factor of $1/e$.

than typical hadrons produced at the LHC, the EM calorimeters are positioned closer to the IP than the tile calorimeters, which primarily measure the energy of hadrons. Due to the geometry of the EM calorimeter, there exists a crack region, $1.37 < |\eta| < 1.52$, with critically degraded energy resolution of electrons and photons [59, 60].

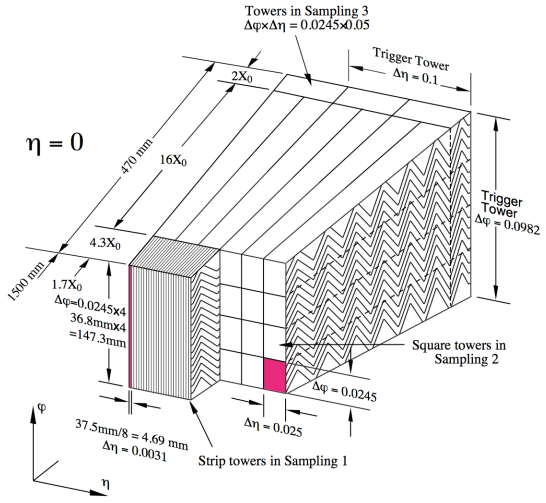


Figure 2.7: The EM calorimeter uses lead absorbing material fashioned in such a way to increase interaction cross section.

2.4.2 Hadronic Calorimetry

Hadronic calorimetry is provided in the central region by the steel/scintillating-tile calorimeter, segmented into three barrel structures within $|\eta| < 1.7$, and two copper/LAr hadronic wheel calorimeters covering the range $2.5 < |\eta| < 3.2$. The region up to $|\eta| = 4.9$ is completed by the LAr forward calorimeter (FCal) with copper and tungsten absorbing material. The hadronic calorimeter provides clusters of energy deposits, typically in three radial segments with $\eta \times \phi$

resolution of 0.1 $\times$ 0.1 for the inner two segements and 0.2 $\times$ 0.2 for the outer segments [61, 62]. During event reconstruction the energy clusters are combined into objects known as jets that signal the presence of a quark or gluon emitted from the IP. More detail on jet reconstruction is provided in Chapter 3. The resolution of the total energy of a reconstructed jet is estimated as in [63], and the most recent estimates for central jets are shown in Fig. 2.8.

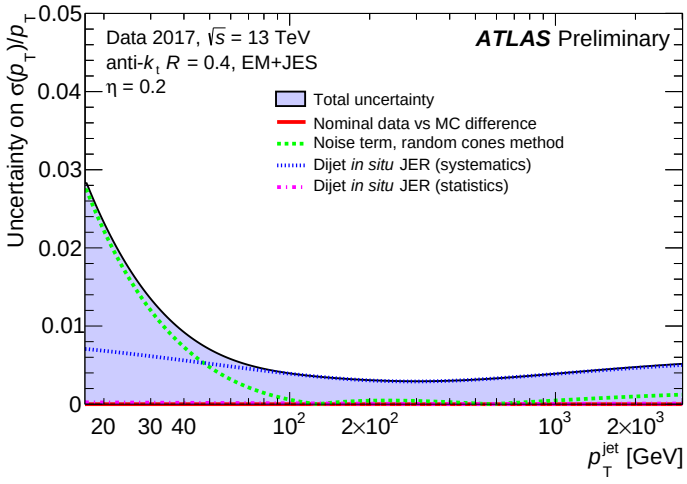


Figure 2.8: Fractional jet energy resolution uncertainty as a function of transverse momentum.

2.5 Muon System

Muons typically travel through the entire ATLAS detector depositing only small amounts of energy. This allows for additional position measurements at the furthest radial position of the ATLAS detector that can be used to match with hits in the ID and reconstruct muons' trajectory, as well as provide reliable triggering for events of interest containing muons. More on triggering is given in

Section 2.6.

2.5.1 Muon Spectrometer and Toroid Magnets

The muon spectrometer (MS) comprises separate trigger and high-precision gas-based tracking chambers measuring the deflection of muons in a magnetic field. The magentic field is generated by superconducting air-core toroids that are cooled to to 4.5 K with liquid He shown in Fig. 2.9. The field integral of the toroids ranges between 2.0 and 6.0 T m across most of the detector [64].

A set of precision chambers covers the region $|\eta| < 2.7$ with three layers of gaseous monitored drift tubes, complemented by cathode-strip chambers in the forward region, where the background is highest. The muon trigger system covers the range $|\eta| < 2.4$ with resistive-plate chambers (RPCs)[3] in the barrel, and thin-gap chambers in the endcap regions [65, 66].

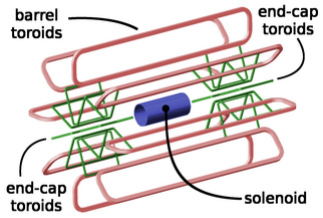


Figure 2.9: The magent system of the ATLAS detector.

The magnetic field present in the MS allows momentum inference that can also be combined with the estimates from the ID. The typical momentum resolution for a reconstructed muon is 2-4% depending on its magnitude and η [67, 68]. The muon system is shown in Fig. 2.10.

[3]The RPC uses a gas-filled chamber between an anode and cathode that provides a discrete signal when a traversing charged particle ionizes the gas and creates electrical continuity between the anode and cathode.

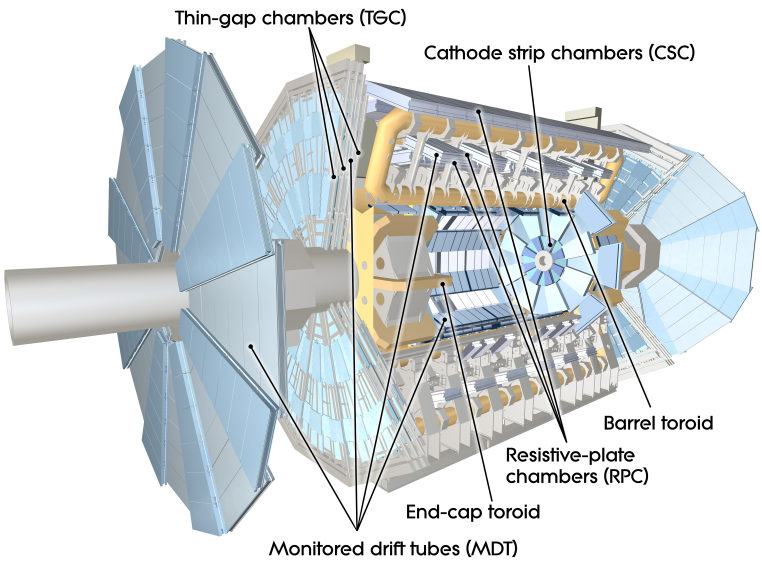


Figure 2.10: The muon detector system provides additional measurements of charged particles that are able to traverse the entire ATLAS detector.

2.6 Trigger System

The LHC provides more collisions per second than could easily be fully collected and analyzed. As a result, only events with sufficiently interesting characteristics such as an energetic, isolated muon seen in the MS or a large deposition of energy in the EM calorimeter, are recorded. The trigger system can generally be described as split into a fast, low level,custom hardware based trigger that identifies significant stimulation of a part of the detector, and a software-based high level trigger (HLT) that performs quick partial object reconstruction and evaluates the credibility that an energetic hard scattering event has occurred [69]. The first-level trigger reduces the 40 MHz bunch crossing rate to below 100 kHz, which the high-level trigger further reduces in order to record events to disk at about 1 kHz. The triggers used in this thesis are described in Chapter 4.

Chapter 3

Physics Object Definitions

For the purpose of this thesis, four physics objects are reconstructed from raw detector information: electrons, muons, jets, and missing transverse energy ($E_{\mathrm{T}}^{\mathrm{miss}}$). Each object leaves a unique signature in the detector that allows their type, charge, direction, and momentum to be determined with sufficient accuracy and efficiency in order to reconstruct entire scattering events that take place within the ATLAS detector. Fig. 3.1 shows an example of expected topologies for different particle

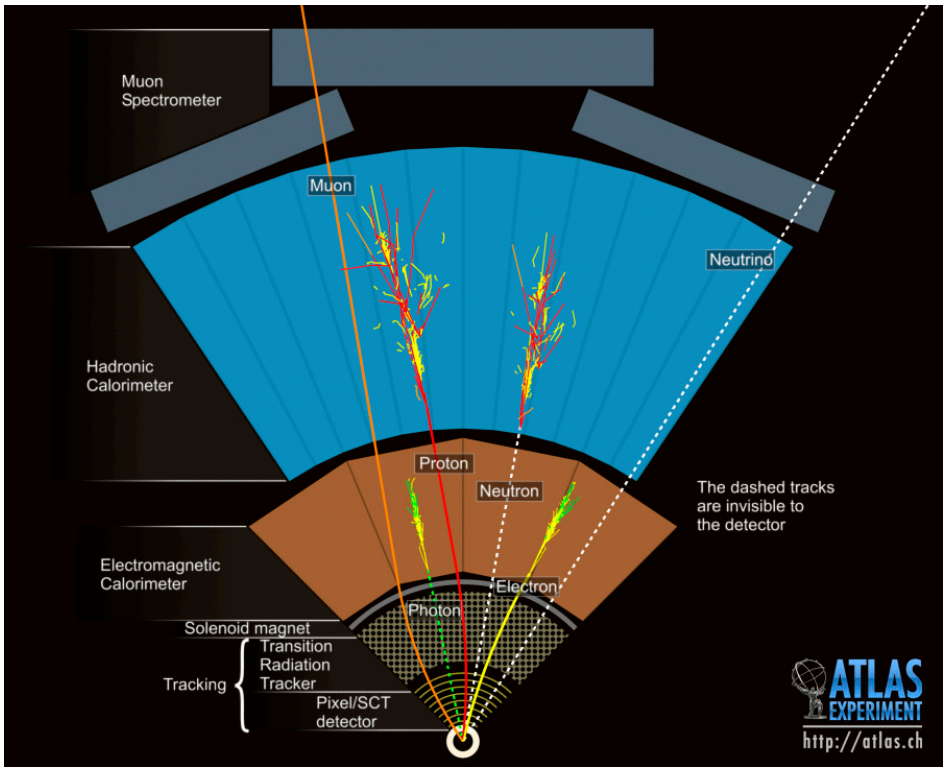


Figure 3.1: Different particle types can be reconstructed using specific signatures left in the ATLAS detector.

types[1] In general, the object identification follows the standard recommendations of the ATLAS combined performance (CP) groups for data collected by ATLAS in 2015–2018 [70]. The reconstruction is performed with the `AnalysisTop-21.2.58` package [71].

3.1 Electrons

Electron candidates are reconstructed from energy deposits in the EM calorimeter associated with ID tracks [72, 58, 73]. The clusters are required to be in the pseudorapidity $|\eta| < 2.47$ region, excluding the transition region between the barrel and end-cap EM calorimeters, $1.37 < |\eta| < 1.52$. The candidate electrons are required to have transverse energy $E_{\mathrm{T}} > 15\,\mathrm{GeV}$. Further requirements on the electromagnetic shower shape, calorimeter energy to tracker momentum ratio, and other discriminating variables are combined into a likelihood-based object quality cut, optimised for strong background rejection. Specifically, three categories are considered: `LooseLH`, `MediumLH`, and `TightLH`, in order of increasing background rejection power.

All electron candidates in this thesis must pass the `TightLH` selection to reject electrons from photon conversion, hadronic particle decays, and fake electrons. Some studies to validate the modeling of electron backgrounds utilize the `LooseLH` selection (Section 6.1).

Electrons are further required to be isolated from other nearby physics objects,

[1] In this illustration, both protons and neutrons generate calorimeter deposits that would form jets, transverse momentum information from neutrinos is obtained via $E_{\mathrm{T}}^{\mathrm{miss}}$, and photon objects are not used in this thesis. The radius of curvature is used to determine particles' charge.

using a `Gradient` working point. This working point varies the electron selection efficiency depending on the electron p_{T}, i.e. lower efficiency at low p_{T} and higher efficiency as the p_{T} rises. For example, the isolation is 90 % efficient for electrons with $p_{\mathrm{T}} = 25\,\mathrm{GeV}$ and 99 % efficient for electrons with $p_{\mathrm{T}} = 60\,\mathrm{GeV}$.

Electron tracks are also required to be consistent with the beam line applying the requirements: $|d_0^{\mathrm{BL}}\ \text{significance}| < 5$ and $|\Delta z_0 \sin\theta| < 0.5\,\mathrm{mm}$. In this requirement "$d_0^{\mathrm{BL}}$ significance" is the number of standard deviations the beam line impact parameter[2] is away from the mean, and Δz_0 is the the z component of the impact parameter with respect to the primary vertex.

3.2 Muons

Muon candidates can be reconstructed both using only the Muon Spectrometer (MS) information (standalone muons) or, as used in this thesis, combining the MS reconstruction with Inner Detector (ID) tracks (combined muons) [74]. To increase the background rejection, some additional requirements are applied on track-parameter quality. Various working points are provided: `Loose`, `Medium`, and `Tight`.

The muon candidates in this analysis must pass the `Medium` identification definition, based, for muons with $|\eta| < 2.5$ and $p_{\mathrm{T}} > 15\,\mathrm{GeV}$, on requirements of hits in MS subsystems, and on the compatibility between ID and MS momentum measurements to remove fake muons.

[2] The impact parameter is the value of closest approach between two objects, typically a continuous curve and a point, or two curves.

The isolation requirement is the same as that of electrons, the `Gradient` working point, which results in a similar p_{T}-dependent efficiency.

Muon tracks are also required to be consistent with the beam line applying the requirements: $|d_0^{\mathrm{BL}}$ significance$| < 3$ and $|\Delta z_0 \sin\theta| < 0.5\,\mathrm{mm}$.

3.3 Jets

Jets are reconstructed from topological calorimeter clusters at the EM scale using the anti-k_t algorithm with radius parameter of 0.4 [75]. They are required to have $p_{\mathrm{T}} > 35\,\mathrm{GeV}$ and $|\eta| < 4.5$.

In order to reject forward jets originating from additional proton-proton interactions, a forward jet vertex tagger (fJVT) requirement is applied. This combines information about jet shapes and topological jet correlations in pile-up interactions, in order to maximize the number of selected jets coming from the hard scattering and reduce pileup jets contamination. This has an efficiency of selecting hard scattered jets of up to 97 % and a pileup-jet efficiency of 53.4 % for jets with p_{T} between 40 GeV and 50 GeV [76].

To further suppress pile-up, a discriminant called the jet-vertex-tagger (JVT) is constructed using a two dimensional likelihood method. Jets are rejected if the JVT variable is below a given threshold for jets with $p_{\mathrm{T}} < 50\,\mathrm{GeV}$ and $|\eta| < 2.4$, corresponding to 92% efficiency and 2% fake rate [77].

3.3.1 b-jets

Jets initiated from a b hadron (b-jets) have a unique topology that includes a secondary decay vertex due to the slightly longer lifetime of typically produced b hadrons as shown in Fig. 3.2 [78]. This unique characteristic, along with other

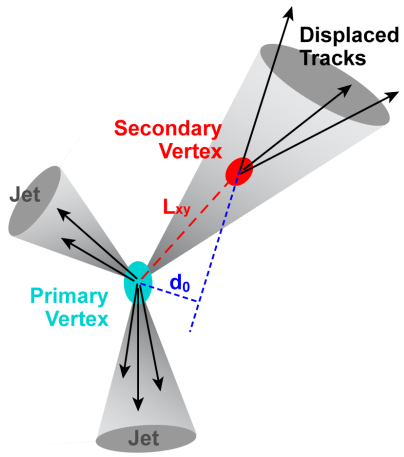


Figure 3.2: Hadronic jets originating from b hadrons typically exhibit a secondary vertex due to the longer lifetime of b hadrons relative to those with lighter quarks.

features, allows for b-jets to be identified, or "tagged". This is useful in the search and measurement of tZq due to the effectively 100% branching fraction of the t quark to a b. For this analysis b-jets are identified using the `MV2c` algorithm. The `MV2c10` variant is used, corresponding to the current recommendations [79]. It is based on a neural network using the output weights of the JetFitter, IP3D and SV1 algorithms as input, which are described in [80]. Pseudo-continuous b-tagging [81] working points are used with a default working point near 70 % efficiency and some validation regions use a working point near 85 %.

3.4 Missing Transverse Energy

The missing transverse momentum, $E_{\mathrm{T}}^{\mathrm{miss}}$, is a measure of the transverse momentum imbalance due to escaping neutrinos. The $E_{\mathrm{T}}^{\mathrm{miss}}$ is calculated as the magnitude of the negative vector sum of the transverse momenta of all identified jets (with $p_{\mathrm{T}} > 20\,\mathrm{GeV}$), electrons and muons (with $p_{\mathrm{T}} > 25\,\mathrm{GeV}$) in the event, as well as a soft term built from tracks that are associated to the hard-scatter vertex but are not associated to any of the reconstructed objects. The soft term is included in order to account for low-momentum particles that are not identified among the final state objects [82, 83, 84].

3.5 Overlap Removal

Physics object reconstruction algorithms can identify the same group of detector stimulations as two different physics objects. An example of this would be an electron reconstructed from calorimeter cells, and a hadronic jet reconstructed using those same calorimeter deposits. The protocol to handle this overlap in reconstruction is known as overlap removal, and the procedure for this thesis is in the following. First, an electron sharing a track with a muon is removed to avoid cases where a muon mimics an electron through radiation of a hard photon. Next, the closest jet to each electron within an η–ϕ cone of size $\Delta R = 0.2$ is removed to reduce the proportion of electrons being reconstructed as jets. Next, electrons with a distance $\Delta R < 0.4$ from any of the remaining jets are removed to reduce backgrounds from non-prompt, non-isolated electrons coming from

heavy-flavor hadron decays. Jets with fewer than three associated tracks and distance $\Delta R < 0.4$ from a muon are then removed to reduce fake jets from muons depositing energy in the calorimeters. Finally, muons with a distance $\Delta R < 0.4$ from any of the surviving jets are removed to avoid contamination of non-prompt muons from heavy-flavor hadron decays.

Chapter 4

Data and Monte Carlo

4.1 Data Sample

The analysis described in this thesis uses data collected from 2015 to 2018 by the ATLAS detector at a centre-of-mass energy of 13 TeV. The complete sample includes all 25 ns data periods from 2015, as well as the whole 2016, 2017 and 2018 datasets. The total integrated luminosity is $139\,\text{fb}^{-1}$. The selected data periods were collected during stable beam LHC operations and with the ATLAS detector fully functioning.

Events are considered only if they are accepted by at least one of the single-muon or single-electron triggers described in Refs. [69, 85, 86] and Section 2.6.

The electron triggers select a calorimeter cluster matched to a ID track. Electrons must then satisfy identification criteria based on a multivariate technique using a likelihood discriminant. In 2015, reconstructed electrons had to satisfy a medium identification and have $E_{\text{T}} > 24\,\text{GeV}$. In 2016, 2017 and 2018, electrons had to satisfy a tight identification together with an isolation criteria and have $E_{\text{T}} > 26\,\text{GeV}$. During the four years, to avoid efficiency losses due to identification and isolation at high p_{T}, two other triggers were also available, selecting medium electrons with $E_{\text{T}} > 60\,\text{GeV}$ and selecting loose electrons with $E_{\text{T}} > 120\,\text{GeV}$ ($140\,\text{GeV}$ in 2016 and 2017).

Muons are triggered on by matching performed by the HLT of tracks recon-

structed in the muon spectrometer and in the inner detector. In 2015, muons had to satisfy a loose isolation requirement and have $p_{\mathrm{T}} > 20\,\mathrm{GeV}$. In 2016, 2017 and 2018, the isolation criterion was tightened and the threshold increased to $p_{\mathrm{T}} > 26\,\mathrm{GeV}$. During the four years, to avoid efficiency losses due to isolation at high p_{T}, another muon trigger without any isolation requirement was available, selecting muons with $p_{\mathrm{T}} > 50\,\mathrm{GeV}$.

4.2 Monte Carlo Simulation

In order to simulate the signature that a pp collision might leave in the ATLAS detector, a Monte Carlo (MC) technique is used [87]. MC generators use randomized sampling from a theoretical probability distribution to predict possible final state particles and their kinematics. Effects from final state QCD radiation and recombination (hadronization), as well as EM radiation, are simulated to estimate the final state hadronic shower behavior. The entire physics simulation is propagated through a GEANT4-based [88] model of the ATLAS detector and a full simulation of particle-detector interactions and responses are produced for the $\mathrm{tZ}q$ signal as well as each of the backgrounds. These simulated samples are used to construct a statistical model of which to compare to data and perform parameter estimation (Chapter 9).

The generated MC samples containing top-quarks are produced with the top-quark mass, m_t, parameter set to 172.5 GeV and a branching fraction of the top-quark decay to a W boson and a b quark set to 1. In all samples, decays

into τ leptons are included and if the τ decays leptonically such events are taken into account in the analysis. The effect of pileup interactions on the samples is accounted for separately for simulations during 2015-16, 2017, and 2018 LHC run conditions as described in Ref. [89]. In the following, samples used in the analysis are explained in detail, both for the signal and for the background sources.

4.3 Signal Sample

4.3.1 tZq Production

The tZq sample is simulated using the MadGraph5_aMC@NLO v2.3.3 [90] MC generator at NLO with the 4FS NNPDF3.0NLO [91] PDF. The generator is interfaced with Pythia8.230 [92] to perform hadronization using a custom ATLAS parameter tune: "A14" [93]. Non-resonant events with leptons away from the Z mass peak are included, and an invariant mass cut on the two opposite sign but same flavor leptons is applied, requiring $m_{ll} > 30\,\text{GeV}$. The top quark is decayed at LO using MadSpin [94, 95] to preserve spin correlations. Following the discussion in Ref. [96], the functional form of the renormalization and factorization scale is set to $4\sqrt{m_{\text{b}}^2 + p_{\text{T,b}}^2}$, where the b-quark is the external one produced from gluon splitting in the event. The decays of bottom and charm hadrons are simulated using the EvtGen program [97].

Following the recommendations from theorists during an LHC Top Working Group [98], the cross-section is calculated separately using the 5FS PDF with the renormalization and the factorization scales set to a fixed value derived from

the mass of the t quark and Z boson: $\mu_{\mathrm{R}} = \mu_{\mathrm{F}} = (m_t + m_Z)/4$. The total SM $\mathrm{t}\ell^+\ell^- q$ cross-section including non-resonant interference at NLO is 101.7 fb, with $m_{ll} > 30\,\mathrm{GeV}$. The renormalization and factorization scale uncertainties on the calculated cross section are $^{+5.2}_{-1.3}\%$ and the PDF uncertainty is $^{+1.0}_{-1.0}\%$. The 4FS simulated sample is normalized to the 5FS cross-section.

The uncertainty due to initial-state-radiation (ISR) is estimated by comparing the nominal $\mathrm{tZ}q$ sample with two additional samples, which have the same setting as the nominal one, but variations to the custom "A14" Pythia8.230 tuning: "Var3c 14". The Var3c A14 tune variation corresponds to the variation of α_{s} for ISR in the A14 tune [93]. This effect is correlated with the renormalization and factorization scales. To account for this, the two scales are varied simultaneously by factors 2.0 and 0.5 respectively with the "Var3c 14 DOWN" and "Var3c 14 UP" tune variations. To evaluate the PDF uncertainties for the nominal PDF, the 100 variations for NNPDF2.3LO are taken into account as recommended from the authors [91].

4.4 Background Samples

Simulated samples are included in the analysis in order to account for all the SM predicted background channels. Throughout this thesis $\mathrm{t\bar{t}}$ and tW are treated together due to their indistinguishably at NLO. The same argument is used for grouping $\mathrm{t\bar{t}Z}$ and tWZ. $\mathrm{t\bar{t}}H$ and $\mathrm{t\bar{t}W}$ are grouped as a "small backgrounds" process for technical ease. It is assumed any bias introduced by combining these

is insignificant due to their almost negligible contribution. Each of the following backgrounds have enough of a significant yield to the signal regions defined in Section 5.2 to warrant individual simulation.

4.4.1 $t\bar{t}$ Production

One of the most important backgrounds to consider in the analysis is that of $t\bar{t}$. In the event of both t quarks decay leptonically and a fake lepton provides a third, the $t\bar{t}$ process can contaminate phase space occupied by tZq. The extremely high cross section of $t\bar{t}$ compared to tZq means that even if the conditions are rare for an event to pass selection, there is still a significant background yield.

The production of $t\bar{t}$ events is modeled using the PowhegBox v2 [99, 100, 101, 102] generator at NLO with the NNPDF3.0NLO [91] PDF and the h_{damp} parameter[1] set to 1.5 m_t [103]. The generator is interfaced with Pythia8.230 [92] using the A14 tune and the NNPDF23LO PDF set. It is required that both the W bosons from the t quarks decay leptonically.

The uncertainty due to final-state radiation (FSR) and ISR is estimated by comparing the nominal $t\bar{t}$ sample with two additional samples in the same way as tZq above, with the additional requirement of varying the h_{damp} parameter to 3.0 m_t for the "Var3c 14 UP" variation [104].

The impact of the parton shower (PS) and hadronization model is evaluated by comparing the nominal generator setup with a sample interfaced with

[1] The h_{damp} parameter controls the transverse momentum p_{T} of the first additional QCD emission beyond the leading-order Feynman diagram in the parton shower and therefore regulates the high-p_{T} emission against which the $t\bar{t}$ system recoils.

HERWIG7.04 [105, 106], using the H7UE set of tuned parameters [106] and the MMHT2014LO PDF set [107]. The difference in the two PS models is taken as a systematic uncertainty.

To assess the uncertainty due to the choice of the event generator and its matching to the hadronization model, the POWHEG sample is compared to a generator setup of MADGRAPH5_AMC@NLO +PYTHIA8. For the calculation of the hard-scattering, MADGRAPH5_AMC@NLO v2.6.0 is interfaced with PYTHIA8.230, using the A14 set of tuned parameters and the 4FS NNPDF23LO PDF.

4.4.2 Single top-quark Production

The s- and t-channels have no overlap with the tZq final state, so only the tW channel of single top production is considered. Fully leptonic decays with an additional fake lepton as well as extra QCD radiation can allow the tW process to contaminate primarily the signal region observing two jets (Section 5.2). tW contributes nearly a negligible amount, but its contribution and quantum interference impact on $t\bar{t}$ is included in the analysis.

Single-top tW associated production is modeled using the POWHEGBOX v2 generator at NLO in QCD in the 5FS with the NNPDF3.0NLO PDF set. The diagram removal (DR) scheme [108] was employed to handle the interference with $t\bar{t}$ production. The generator is interfaced with PYTHIA8.230 using the A14 tune using the NNPDF23LO PDF set.

4.4.3 $t\bar{t}H$ production

The $t\bar{t}H$ process is a very small background in the analysis mostly due to its extremely small cross section. Events where a H boson decays into leptons, generally first cascading from τ decays, and one of the $b-$jets from the t decays is mis-tagged can be present in phase space occupied by tZq. The production of $t\bar{t}H$ events is modeled using the PowhegBox generator at NLO with the NNPDF3.0NLO PDF set. The generator is interfaced with Pythia8.230 using the A14 tune and the NNPDF2.3LO PDF set. In the samples used the W bosons from the t quarks can decay hadronically or leptonically.

4.4.4 $t\bar{t}V$ Production

The $t\bar{t}Z$ process is a large contribution to the background modeling of the tZq analysis. The $t\bar{t}Z$ decay with three leptons also has four jets, two of them originating from a b at LO. If one of the $b-$jets falls outside detector acceptance or two jets are mis-reconstructed as one, the $t\bar{t}Z$ process will be present in the signal region observing three jets (Section 5.2). In the case of a four-lepton decay channel with one being mis-reconstructed, contributions from extra QCD radiation can allow $t\bar{t}Z$ background in either signal region, again allowing one of the $b-$jets is also mis-tagged. The production of $t\bar{t}V$ ($V = W, Z$) events is modelled using the MadGraph5_aMC@NLO v2.3.3 [90] generator at NLO with the 4FS NNPDF3.0NLO PDF. The generator is interfaced with Pythia8.210 using the A14 tune using the NNPDF2.3LO PDF set.

The uncertainty due to ISR is estimated by comparing the nominal $t\bar{t}V$

sample with additional samples similar to tZq and $t\bar{t}$ above. The impact of FSR is evaluated by varying the renormalization scale for QCD emission in the hadronization by a factor of 0.5 and 2.0, respectively. An additional $t\bar{t}Z$ sample is produced to evaluate the uncertainty on MC generator choice with the SHERPA 2.2.1 [109] generator at NLO accuracy.

4.4.5 tWZ Production

The tWZ process is an irreducible background in the signal region containing three jets when one of the two W bosons decays hadronically. It can also be present in the two-jet signal region when one of the jets is mis-reconstructed (Section 5.2). The production of tWZ events is modeled using the MADGRAPH5_AMC@NLO v2.3.3 generator at NLO with the NNPDF3.0NLO PDF. The generator is interfaced with PYTHIA8.212 using the A14 tune and the NNPDF2.3LO PDF set. In the sample used, it is required that the Z boson decays leptonically.

The uncertainty due to ISR and FSR is estimated the same as tZq, $t\bar{t}Z$ above. An uncertainty on the choice of generator model is estimated by comparing the nominal MADGRAPH5_AMC@NLO v2.3.3 sample with one generated using SHERPA v2.2 [109]. An additional tWZ systematic is created to estimate the uncertainty due to the interference between $t\bar{t}Z$ and tWZ. This systematic variation handles the interfering diagrams with the "DR2" scheme whereas the nominal sample uses the "DR1" [108].

4.4.6 Diboson Production

The samples simulating WW, WZ and ZZ events with at least two charged leptons are all considered. In the trilepton topology, WZ + jets events are the ones that significantly contribute to the background composition. Fully leptonically and semileptonically decaying diboson samples are simulated with the SHERPA v2.2 [109] generator. In this setup multiple matrix elements are matched and merged with the SHERPA PS algorithm based on Catani-Seymour dipole [110, 111] using the MEPS@NLO prescription [112, 113, 114, 115]. The virtual QCD correction for matrix elements at NLO accuracy are provided by the OPENLOOPS library [116, 117]. Samples are generated using the `NNPDF3.0nnlo` set [91], along with the dedicated set of tuned PS parameters developed by the SHERPA authors. An uncertainty on the choice of generator model is estimated by comparing the nominal sample with one generated using POWHEGBOX v2.

The diboson background in this thesis is split into VV + HF (heavy flavor) and VV + LF (light flavor) based on the types of jets associated: if one of the associated jets originated from b-quark or c-quark then it is considered as VV + HF, otherwise it is considered as VV + LF. The jet type is determined using a simple matching algorithm. The algorithm defines a cone of $\Delta R < 0.3$ associated with each jet. If a b-hadron with ($p_{\mathrm{T}} > 5\,\mathrm{GeV}$) is found within this cone the jet is identified as a b-jet. If no b-hadrons are found, the algorithm will then search for c-hadrons, then τ leptons. If none of these identifiers are found the jet is labeled as a light jet.

4.4.7 Z + jets Production

While Z + jets production contains events where the two leptons come from a Z boson, in order to pass signal region selections a third lepton must be a fake lepton (Section 5.2). The Z + jets background is unique in that it is the only significant source of fake leptons suspected to originate from photon conversions (Section 6.1). QCD V+ jets production is simulated with the SHERPA v2.2 [109] generator. Similar to the diboson production, matrix elements are matched and merged with the SHERPA parton shower based on Catani-Seymour dipole using the MEPS@NLO prescription, and the virtual QCD correction for matrix elements at NLO accuracy are provided by the OPENLOOPS library. Samples are generated using the `NNPDF3.0nnlo` set, along with the dedicated set of tuned PS parameters developed by the SHERPA authors. A generator-level cut requiring the invariant mass of the two leptons to be $\geq 40\,\text{GeV}$ is applied.

Chapter 5

Event Selection

In order to verify modeling of physics processes in the relevant areas of kinematic phase space, a set of signal, control, and validation regions are defined. Each region is defined by a set of selection cuts on the reconstructed variables. These include variables reconstructed from intermediate-state particles calculated from final state observables.

5.1 Full Event Reconstruction

At lowest order, the final state of the trilepton channel of the SM
tZq process consists of three charged leptons (two coming from the Z decay and one from the leptonic W decay), one neutrino, one b quark, as well as one light quark (expected to go preferentially in the forward direction).

Reconstructing the mother particles (Z boson and t quark) is important in order to identify specific features that help to separate signal from background. For example, the Z-boson mass distribution can contribute to the reduction of top-quark backgrounds, as these do not include a Z boson in the final state, while the q pseudorapidity distribution has a very different shape in
tZq events than in $t\bar{t}Z$ events, which constitute one of the largest backgrounds.

In order to reconstruct the Z boson, an opposite-sign, same-flavor (OSSF) lepton pair is needed. In the μee and e$\mu\mu$ channels, this is uniquely identified. For the eee and $\mu\mu\mu$ events, both possible combinations are considered and the

pair that has the invariant mass closest to the Z-boson mass is chosen.

The W boson, that is expected to decay leptonically, is reconstructed from the remaining lepton and the missing momentum of the event, which is attributed to the W's neutrino. The missing part of the neutrino four-vector is the longitudinal component along the z-axis (E_Z^{miss}), which can be obtained by using the mass constraint of the W boson on the constituent's four-vectors

$$(P^{\text{W}})^2 = (P^{\ell} + P^{\text{miss}})^2 = M_{\text{W}}^2\,, \tag{5.1}$$

where the M_{W} is the W boson mass, 80.4 GeV.

The solution of the quadratic equation given in Equation 5.1 in terms of the E_Z^{miss} can be expressed as follows

$$E_Z^{\text{miss}} = \frac{\alpha \cdot P_{\text{Z}}^{\ell} \pm \sqrt{(E^{\ell})^2 \cdot [\alpha^2 - p_{\text{T}}^{\ell} \cdot E_{\text{T}}^{\text{miss}}]}}{(p_{\text{T}}^{\ell})^2}\,, \tag{5.2}$$

where α is given by

$$\alpha = \frac{M_{\text{W}}^2}{2} + \overrightarrow{p_{\text{T}}}^{\ell} \cdot \overrightarrow{E_{\text{T}}^{\text{miss}}}\,. \tag{5.3}$$

When the quantity under the square root is positive ($\alpha^2 \geq p_{\text{T}}^{\ell} \cdot E_{\text{T}}^{\text{miss}}$), then there are two real solutions, and the smallest one in magnitude is taken, since the W boson is expected to be produced with small rapidity. If there is one complex solution the real solution is chosen, and for some of the events, Equation 5.2 has two imaginary solutions (when $\alpha^2 < p_{\text{T}}^{\ell} \cdot E_{\text{T}}^{\text{miss}}$). In this case the transverse mass, $m_{\text{T}}(\text{W})$, is greater than M_{W} and $m_{\text{T}}(\text{W})$ is explicitly set to equal M_{W} and the neutrino 4-vector is rescaled. This is attributed to imperfect detector resolution. For the t-quark reconstruction, the previously reconstructed W boson, together with the b-tagged jet are used.

A summary of relevant symbols representing the reconstructed objects is presented in Table 5.1.

Table 5.1: Object reconstruction. More details about the reconstruction process can be found in the text.

Symbol	Description
ℓ_1^{Z}	Highest p_{T} lepton from the reconstructed Z boson
ℓ_2^{Z}	Lowest p_{T} lepton from the reconstructed Z boson
Z	Reconstructed Z boson
ℓ^{W}	Lepton from the reconstructed W boson from the t-quark decay
W	Reconstructed W boson from the t-quark decay
b_1	b-tagged jet
t	Reconstructed t quark
$\mathrm{j_f}$	Forward jet (see Section 5.2 for more details)
$\mathrm{j_r}$ or $\mathrm{j_{Rad}}$	Radiation jet (see Section 5.2 for more details)
$\ell_{1/2/3}$	p_{T} ordered leptons
$\mathrm{j}_{1/2/3}$	p_{T} ordered jets

5.2 Signal Regions (SRs) and Their Relation to CR/VRs

As already mentioned in Section 1.1.6 the tZq signal most preferentially occupies an area of final-state phase space that consists of three leptons, $E_{\mathrm{T}}^{\mathrm{miss}}$, and two jets, one of which originates from a b-quark and the other tends to be more forward.

QCD calculations at NLO suggest that there can exist significant QCD radiation present in the event which can manifest itself in the form of a third reconstructed jet.

In order to increase acceptance as much as reasonably possible, two orthogonal signal regions (SRs) are defined as shown in Table 5.2. In one region events with three leptons, one b-tagged jet (using the 70 % working point, Section 3.3), and one untagged jet[1] are selected. This region will be referred to as *SR-2j1b* in the following. In the second signal region, events are selected identically to the first except for the inclusion of a second untagged jet. This region will be referred to as *SR-3j1b* in the following. Of the two untagged jets the one that gives, with the b-jet, the highest invariant mass, $m_{\mathrm{bj_f}}$, is selected to be the *forward* jet. The remaining jet is called *radiation* jet. In the SR-2j1b, the forward jet is uniquely defined. The same nomenclature is used for the jets in the validation and control regions.

The three leptons are sorted by their p_{T}, irrespective of flavour, and required to have transverse momenta of at least 28, 20 and 20 GeV, respectively. At least one of the leptons needs to be matched as one that initiated the event trigger. All leptons must be reconstructed in the central detector region ($|\eta| < 2.5$).

Jets are required to have $p_{\mathrm{T}} > 35$ GeV. Since the untagged jet (or one of the two untagged jets in the SR-3j1b) tends to be in the forward direction, jets are accepted up to $|\eta|$ of 4.5, compared to $|\eta| < 2.5$, which is the cut applied to the

[1] An "untagged" jet is a jet that fails the b-jet selection. Given that the requirement is to have exactly one b-tagged jet with 70 % WP, the other jet is untagged in the sense that it is required to fail the 70 % WP selection.

b-tagged jet.

Additionally, in order to suppress backgrounds that do not contain a Z boson, a cut is applied on the invariant mass of the two OSSF leptons associated to the Z. This is required to be between 81 and 101 GeV.

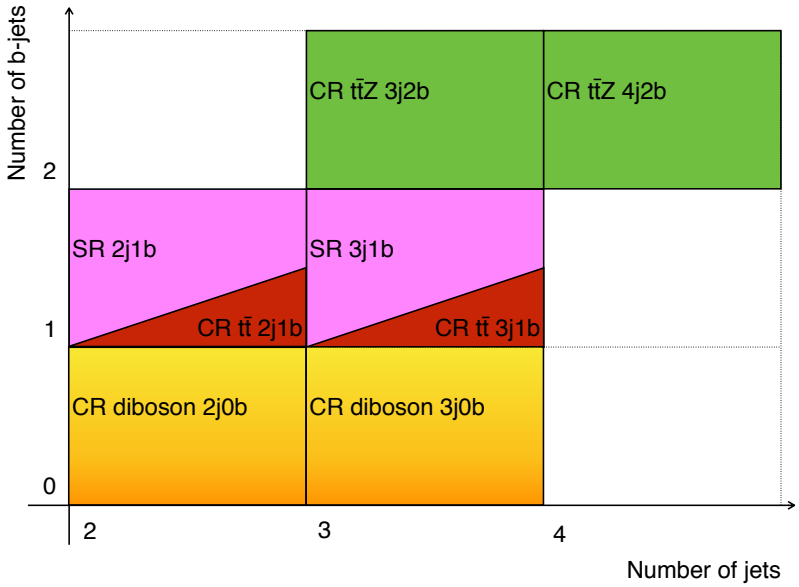


Figure 5.1: Summary of the analysis regions. The CR $t\bar{t}$ regions require a veto on the OSSF lepton pair.

The full selection cuts applied in the signal regions are listed in Table 5.2. In this table, also the selection cuts for the definition of validation and control regions are reported. These regions are constructed such that they are enriched in three of the main sources of background: diboson, $t\bar{t}Z$ and $t\bar{t}$ production. Their definitions are very close, but still orthogonal, to the signal regions to ensure good modeling near important phase space. Fig. 5.1 visualizes the signal and control regions, in terms of jet and b-jet multiplicities. The validation and control regions are described in detail in 5.3 and 5.4.

Common selections			
Exactly 3 leptons with $\|\eta\| < 2.5$			
$p_{\mathrm{T}}(\ell_1) > 28\,\mathrm{GeV}$, $p_{\mathrm{T}}(\ell_2) > 20\,\mathrm{GeV}$, $p_{\mathrm{T}}(\ell_3) > 20\,\mathrm{GeV}$			
$p_{\mathrm{T}}(\mathrm{jet}) > 35\,\mathrm{GeV}$			
SR 2j1b	Diboson 2j0b CR	$\mathrm{t\bar{t}Z}$ 3j2b CR	$\mathrm{t\bar{t}}$ 2j1b CR
≥ 1 OSSF pair	≥ 1 OSSF pair	≥ 1 OSSF pair	≥ 1 OSDF pair
$\|m_{\ell\ell} - m_Z\| < 10\,\mathrm{GeV}$	$\|m_{\ell\ell} - m_Z\| < 10\,\mathrm{GeV}$	$\|m_{\ell\ell} - m_Z\| < 10\,\mathrm{GeV}$	No OSSF pair
2 jets, $\|\eta\| < 4.5$	2 jets, $\|\eta\| < 4.5$	3 jets, $\|\eta\| < 4.5$	2 jets, $\|\eta\| < 4.5$
1 b-jet, $\|\eta\| < 2.5$	0 b-jets	2 b-jets, $\|\eta\| < 2.5$	1 b-jet, $\|\eta\| < 2.5$
	Diboson 2j1Lb VR	$\mathrm{t\bar{t}}V + \mathrm{t\bar{t}}$ 2j1b VR	
	≥ 1 OSSF pair	≥ 1 OSSF pair	
	$\|m_{\ell\ell} - m_Z\| < 10\,\mathrm{GeV}$	$\|m_{\ell\ell} - m_Z\| > 10\,\mathrm{GeV}$	
	2 jets, $\|\eta\| < 4.5$	2 jets, $\|\eta\| < 4.5$	
	1 'Loose' b-jet, $\|\eta\| < 2.5$	1 b-jet, $\|\eta\| < 2.5$	
SR 3j1b	Diboson 3j0b CR	$\mathrm{t\bar{t}Z}$ 4j2b CR	$\mathrm{t\bar{t}}$ 3j1b CR
≥ 1 OSSF pair	≥ 1 OSSF pair	≥ 1 OSSF pair	≥ 1 OSDF pair
$\|m_{\ell\ell} - m_Z\| < 10\,\mathrm{GeV}$	$\|m_{\ell\ell} - m_Z\| < 10\,\mathrm{GeV}$	$\|m_{\ell\ell} - m_Z\| < 10\,\mathrm{GeV}$	No OSSF pair
3 jets, $\|\eta\| < 4.5$	3 jets, $\|\eta\| < 4.5$	4 jets, $\|\eta\| < 4.5$	3 jets, $\|\eta\| < 4.5$
1 b-jet, $\|\eta\| < 2.5$	0 b-jets	2 b-jets, $\|\eta\| < 2.5$	1 b-jet, $\|\eta\| < 2.5$
	Diboson 3j1Lb VR	$\mathrm{t\bar{t}}V + \mathrm{t\bar{t}}$ 3j1b VR	
	≥ 1 OSSF pair	≥ 1 OSSF pair	
	$\|m_{\ell\ell} - m_Z\| < 10\,\mathrm{GeV}$	$\|m_{\ell\ell} - m_Z\| > 10\,\mathrm{GeV}$	
	3 jets, $\|\eta\| < 4.5$	3 jets, $\|\eta\| < 4.5$	
	1 'Loose' b-jet, $\|\eta\| < 2.5$	1 b-jet, $\|\eta\| < 2.5$	

Table 5.2: Overview of the requirements applied for selecting events in the signal, validation and control regions. The 'Loose' b-jet requirement means that one jet passes the 85 % efficient b-tagging working point requirement but does not pass the 70 % efficient working point.

5.2.1 SRs Plots and Yields

The two signal regions show similar signal to background ratios when studying simulated events. The event yields in the SRs after the full selection can be found in Table 5.3 and histogram distributions of reconstructed variables from the top quark and Z boson are given in Fig. 5.2.

Process	Number of events	Number of raw events
$t\bar{t}Z$	62.7 ± 1.4	45837
$t\bar{t}W$	4.3 ± 0.3	1513
$t\bar{t}H$	2.1 ± 0.1	4487
tWZ	17.9 ± 1.0	2992
VV + HF	101.3 ± 1.0	39010
VV + LF	22.7 ± 0.6	5137
Z + jets	10.2 ± 0.0	173703
$t\bar{t}$	23.7 ± 0.1	172074
tW	1.1 ± 0.0	1969
tZq	81.1 ± 0.7	307562
Total expected	327.0 ± 2.3	754284
Data	359	359

Process	Number of events	Number of raw events
$t\bar{t}Z$	96.6 ± 1.9	77643
$t\bar{t}W$	2.2 ± 0.2	765
$t\bar{t}H$	2.4 ± 0.1	4442
tWZ	20.2 ± 1.1	3601
VV + HF	59.4 ± 0.6	24821
VV + LF	12.3 ± 0.4	3164
Z + jets	4.8 ± 0.0	77167
$t\bar{t}$	11.1 ± 0.0	73697
tW	0.4 ± 0.0	736
tZq	46.1 ± 0.5	208092
Total expected	255.3 ± 2.4	474128
Data	259	259

Table 5.3: Numbers of expected events in the SR-2j1b (Left) and SR-3j1b (Right) broken down by process. The uncertainty shown contains only the statistical component.

The predicted number of events to pass selection cuts based on MC simulations for tZq as well as all previously mentioned backgrounds are tabulated. The MC predictions for the backgrounds containing a non-prompt or fake leptons are given after the b-jet replacement method is performed as described in Chapter 6. The events in these regions are the primary regions of interest for the statistical analysis described in Chapter 9 after having been evaluated by the neural network described in Chapter 7.

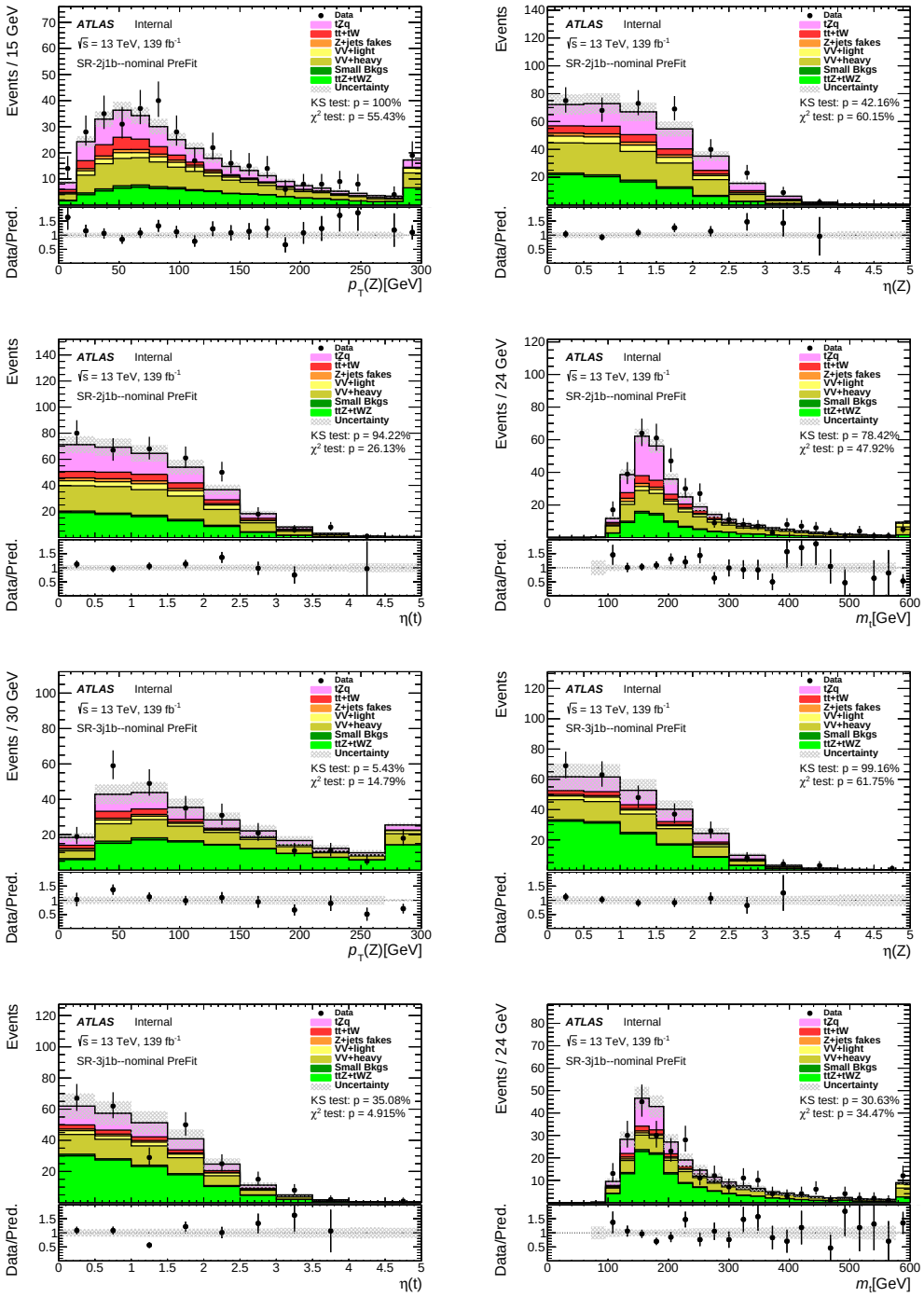


Figure 5.2: Comparison of data and MC predictions for reconstructed event-related quantities for events in the SR-2j1b and SR-3j1b. The uncertainty shown is the backgrounds' modeling uncertainty.

5.3 Control Regions

In order to insure proper modeling of each relevant background, a series of control regions that exhibit enhanced contribution from relevant backgrounds as close to the SRs as possible are also designed and their contents are also added to the statistical analysis (Chapter 9). There are two CRs for each background, one corresponding to each signal region.

To define regions of phase space enriched in diboson production, the presence of a b-jet is vetoed. This effectively removes events containing a top quark leaving events such as WZ to dominate. This region also has significant contamination from $\mathrm{Z}+\mathrm{jets}$ events that contain a fake lepton, a fact which is exploited in Chapter 9 to better model overall $\mathrm{Z}+\mathrm{jets}$ contribution. The $\mathrm{t\bar{t}Z}$ control regions require an additional b-jet to enhance events with a *second* top quark. Finally, the $\mathrm{t\bar{t}}$ contribution can be enhanced by requiring the OSSF lepton requirement be removed, effectively removing the requirement on the Z boson. This phase space is dominated by $\mathrm{t\bar{t}}$ events with a fake lepton and a b-jet that is mistagged.

Every region labeled as a CR is included in the statistical analysis to aide in estimating background yields as well as constrain the effects from systematic uncertainties (Chapter 9). The regions labeled VR are not included in the fit and are used to validate the post-fit modeling and background estimates by comparing the data-MC compatibility.

5.3.1 Diboson CRs Plots and Yields

The two diboson control regions as defined in Table 5.2, are included in the fit. The event yields in the diboson CRs after the full selection can be found in Table 5.4, and the reconstructed variables for the vector bosons are shown in Fig. 5.3. The large uncertainty band in Fig. 5.3 is primarily due to the generator modeling systematic described in Section 4.4.6 indicating a sizeable disagreement between PowhegBox and Sherpa at higher jet multiplicities [118].

Process	Number of events	Number of raw events
$t\bar{t}Z$	42.2 ± 1.2	31829
$t\bar{t}W$	1.8 ± 0.2	604
$t\bar{t}H$	1.1 ± 0.1	2086
tWZ	16.7 ± 1.0	2672
VV + HF	382.1 ± 1.8	146671
VV + LF	2039.7 ± 4.8	792748
Z + jets	63.5 ± 0.2	1065907
$t\bar{t}$	13.8 ± 0.0	234791
tW	0.5 ± 0.0	4561
tZq	55.4 ± 0.6	226420
Total expected	2616.8 ± 5.4	2508289
Data	2703	2703

Process	Number of events	Number of raw events
$t\bar{t}Z$	46.1 ± 1.3	38722
$t\bar{t}W$	0.7 ± 0.1	287
$t\bar{t}H$	1.0 ± 0.1	1766
tWZ	12.5 ± 0.9	2277
VV + HF	190.0 ± 1.1	80609
VV + LF	708.0 ± 2.2	310959
Z + jets	20.2 ± 0.1	388570
$t\bar{t}$	6.8 ± 0.0	91122
tW	0.3 ± 0.0	1345
tZq	22.3 ± 0.4	120942
Total expected	1008.0 ± 2.9	1036599
Data	949	949

Table 5.4: Numbers of expected events in the CR-2j0b (Left) and CR-3j0b (Right) broken down by process. The uncertainty shown contains only the statistical component.

The large number of observed events in this control region helps to provide a significant constraint on the overall rate of diboson events. Because this region is comprised of almost entirely two diboson backgrounds, if one increases, the other must decrease to maintain agreement with data, and the two are inversely correlated. This inverse correlation causes the rate of the two backgrounds to

be dependent on one another, and as a result, constraints on $VV + \text{LF}$ helps to constrain $VV + \text{HF}$ and vice versa. The $VV + \text{HF}$ background is also additionally controlled by the background-enriched regions of the signal regions shown in Section 9.3.

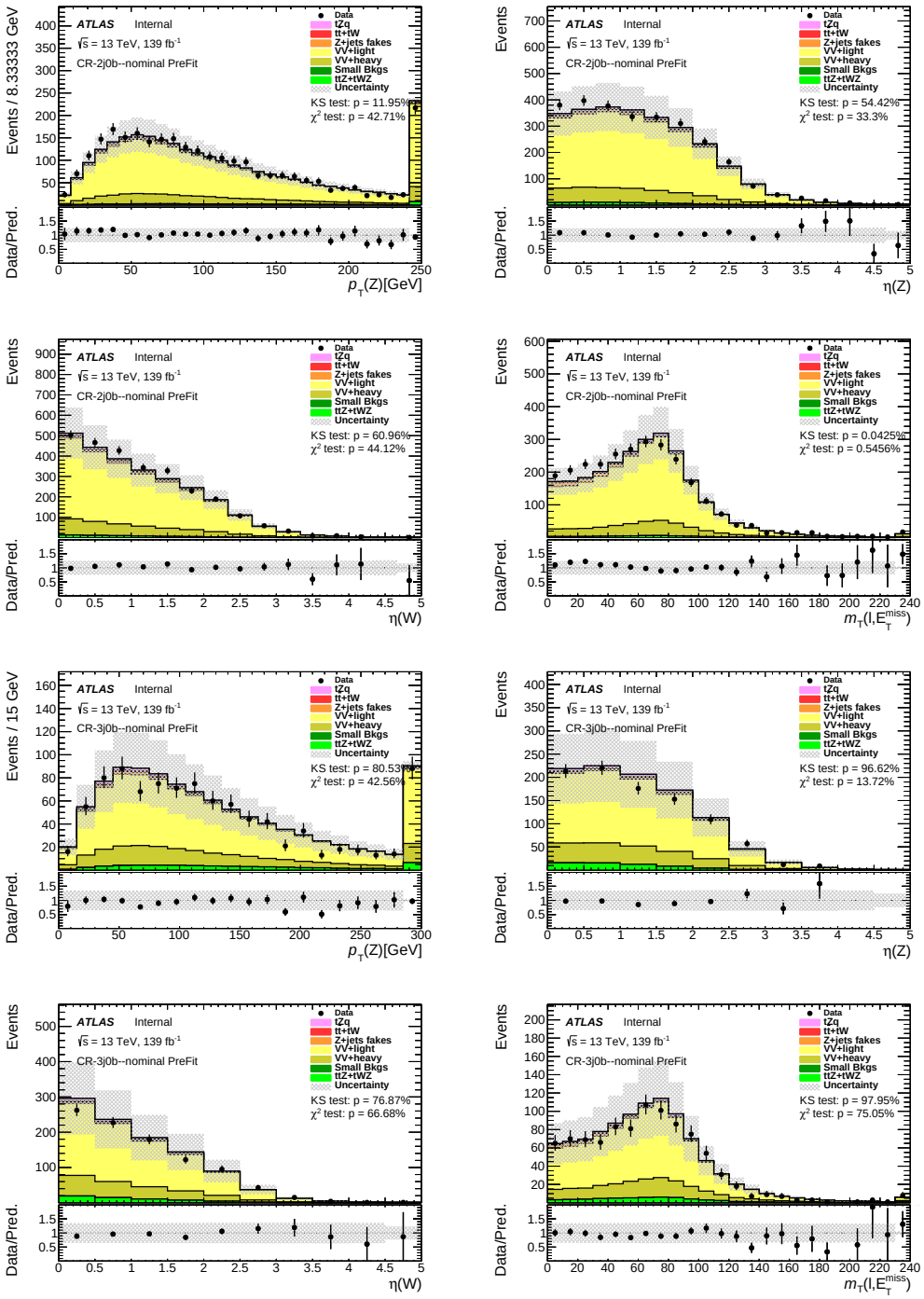


Figure 5.3: Comparison of data and MC predictions for reconstructed event-related quantities for events in the CR-2j0b and CR-3j0b. The uncertainty shown is the backgrounds' modeling uncertainty.

5.3.2 $t\bar{t}Z$ CRs Plots and Yields

The two $t\bar{t}Z$ control regions are also defined in Table 5.2. The event yields in the $t\bar{t}Z$ CRs after the full selection can be found in Table 5.5 and reconstructed variables from the top quark and Z boson are given in Fig. 5.4.

Process	Number of events	Number of raw events
$t\bar{t}Z$	45.1 ± 1.2	35187
$t\bar{t}W$	1.3 ± 0.2	552
$t\bar{t}H$	1.4 ± 0.1	2858
tWZ	4.4 ± 0.5	663
VV + HF	5.3 ± 0.2	2682
VV + LF	0.1 ± 0.0	9
Z + jets	0.5 ± 0.0	2972
$t\bar{t}$	1.6 ± 0.0	2944
tW	0.1 ± 0.0	28
tZq	13.2 ± 0.2	36019
Total expected	73.1 ± 1.4	83914
Data	92	92

Process	Number of events	Number of raw events
$t\bar{t}Z$	47.5 ± 1.3	42202
$t\bar{t}W$	0.6 ± 0.1	228
$t\bar{t}H$	1.3 ± 0.1	2099
tWZ	4.0 ± 0.5	762
VV + HF	3.3 ± 0.1	1630
VV + LF	0.1 ± 0.0	7
Z + jets	0.1 ± 0.0	2021
$t\bar{t}$	1.0 ± 0.0	1644
tW	0.0 ± 0.0	15
tZq	8.6 ± 0.2	27582
Total expected	66.6 ± 1.4	78190
Data	75	75

Table 5.5: Numbers of expected events in the CR-3j2b (Left) and CR-4j2b (Right) broken down by process. The uncertainty shown contains only the statistical component.

The $t\bar{t}Z$ CRs are unique in that they require an extra b-jet which introduces an ambiguity in the event selection and reconstruction criteria. To handle this, the b quark that reconstructs a top quark mass closest to 172.5 GeV is used. The forward jet is then selected as in Section 5.2.1. The $t\bar{t}Z$ CRs also have contamination from tZq signal events which can create a bias in the measurement. This is solved by fitting the neural-network output, O_{NN}, distribution (Chapter 9) which shows seperation between the tZq and $t\bar{t}Z$. This allows robust constraint of $t\bar{t}Z$ modeling and also a slight boost to the overall measurement's senstivity.

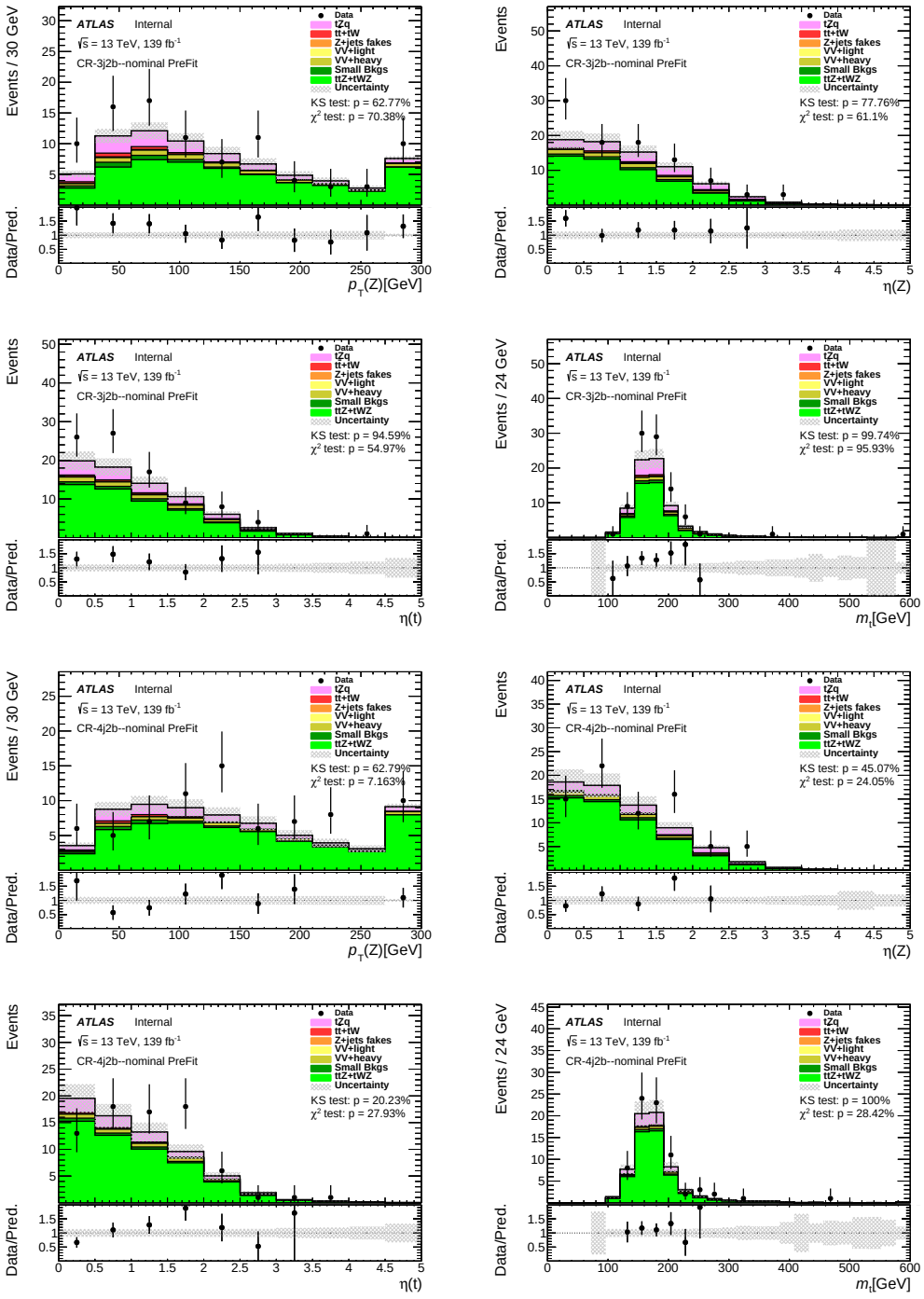


Figure 5.4: Comparison of data and MC predictions for reconstructed event-related quantities for events in the CR-3j2b and CR-4j2b. The uncertainty shown is the backgrounds' modeling uncertainty.

5.3.3 $t\bar{t}$ CRs Plots and Yields

The two $t\bar{t}$ CRs are also defined in Table 5.2. The event yields in the $t\bar{t}$ CRs after the full selection can be found in Table 5.6 and reconstructed variables from the top quark and Z boson are given in Fig. 5.5.

Process	Number of events	Number of raw events
$t\bar{t}Z$	3.5 ± 0.5	2533
$t\bar{t}W$	9.3 ± 0.5	2914
$t\bar{t}H$	2.8 ± 0.1	6782
tWZ	0.9 ± 0.2	143
VV + HF	0.4 ± 0.1	166
VV + LF	0.1 ± 0.0	19
Z + jets	0.0 ± 0.0	330
$t\bar{t}$	34.0 ± 0.1	327074
tW	0.8 ± 0.0	3935
tZq	0.2 ± 0.0	1101
Total expected	52.0 ± 0.7	344997
Data	49	49

Process	Number of events	Number of raw events
$t\bar{t}Z$	3.6 ± 0.5	2827
$t\bar{t}W$	4.7 ± 0.4	1756
$t\bar{t}H$	3.3 ± 0.1	6881
tWZ	0.2 ± 0.2	80
VV + HF	0.3 ± 0.0	101
VV + LF	0.0 ± 0.0	8
Z + jets	0.0 ± 0.0	194
$t\bar{t}$	15.3 ± 0.0	146886
tW	0.5 ± 0.0	1677
tZq	0.2 ± 0.0	794
Total expected	28.1 ± 0.6	161204
Data	31	31

Table 5.6: Numbers of expected events in the CR-ttbar-TTT-2j1b (Left) and CR-ttbar-TTT-3j1b (Right) broken down by process. The uncertainty shown contains only the statistical component.

The $t\bar{t}$ CRs suffer from the lowest statistics of all fitted regions. Because of this, only a single histogram bin per region is used in the statistical analysis.

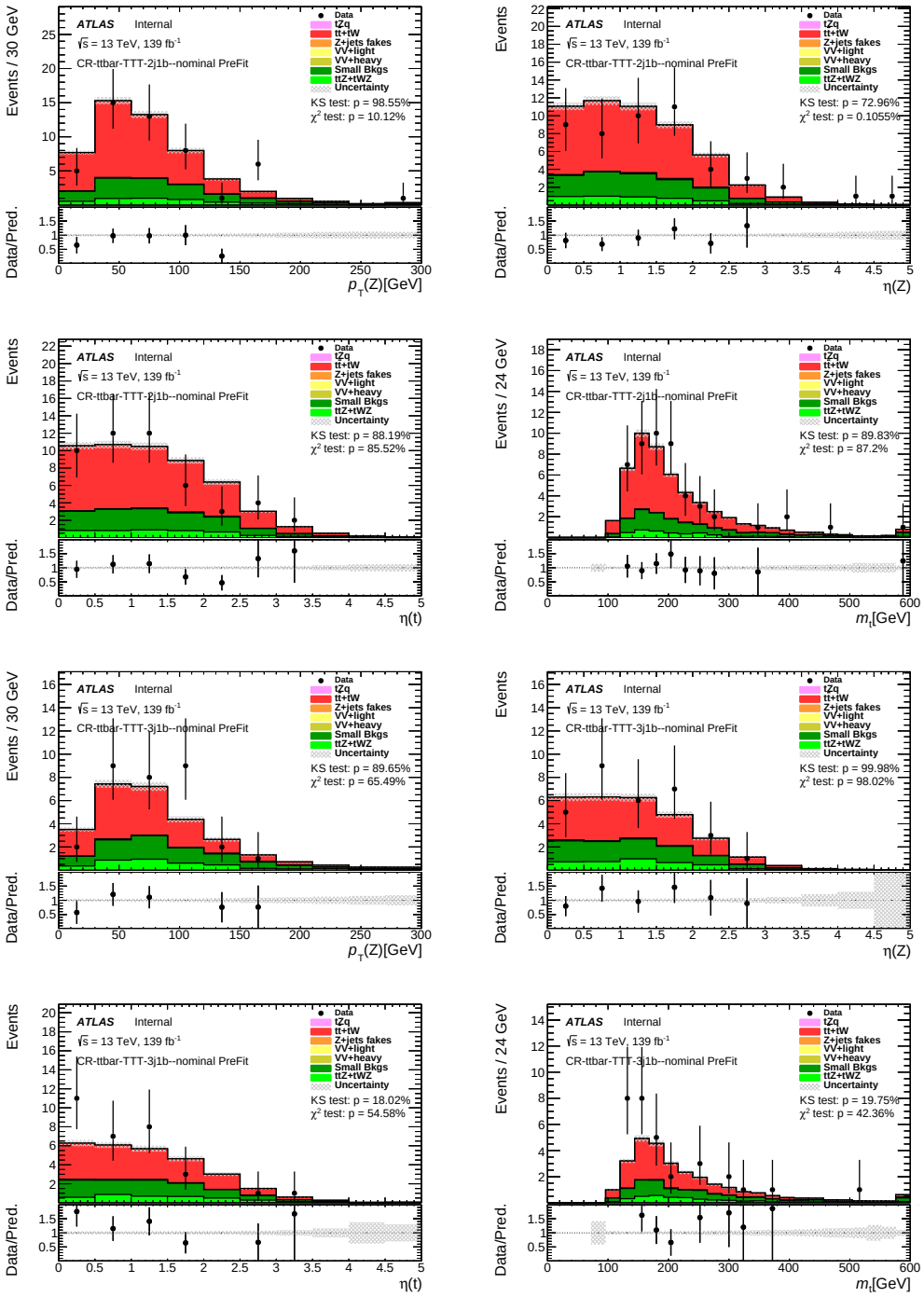


Figure 5.5: Comparison of data and MC predictions for reconstructed event-related quantities for events in the CR-ttbar-TTT-2j1b and CR-ttbar-TTT-3j1b. The uncertainty shown is the backgrounds' modeling uncertainty.

5.4 Validation Regions

In addition to the background control regions, a series of validation regions are also defined with the purpose of validating the post fit modeling after the fit in a region of phase space that does not influence the fit and is still near the signal regions.

5.4.1 $t\bar{t}$ VRs Prefit Yields

Two $t\bar{t}$ VRs are defined by inverting the invariant mass cut of the OSSF lepton pair, essentially veto-ing the presence of a Z boson as summarized in Table 5.2. The prefit event yields in the $t\bar{t}$ VRs after the full selection can be found in Table 5.7. The post-fit data-MC comparison is given in Section 9.4. Further pre-fit plots are provided in Appendix B.

Process	Number of events	Number of raw events
$t\bar{t}Z$	19.3 ± 1.0	14226
$t\bar{t}W$	22.6 ± 0.8	7509
$t\bar{t}H$	7.6 ± 0.2	17754
tWZ	3.5 ± 0.4	537
VV + HF	18.8 ± 0.4	9034
VV + LF	4.2 ± 0.2	1089
Z + jets	4.9 ± 0.1	20883
$t\bar{t}$	81.0 ± 0.1	808306
tW	3.4 ± 0.0	9864
tZq	10.4 ± 0.2	40982
Total expected	175.6 ± 1.4	930184
Data	196	196

Process	Number of events	Number of raw events
$t\bar{t}Z$	25.7 ± 1.2	20433
$t\bar{t}W$	11.4 ± 0.6	4240
$t\bar{t}H$	9.0 ± 0.2	18094
tWZ	3.0 ± 0.4	534
VV + HF	10.8 ± 0.3	5244
VV + LF	2.2 ± 0.1	594
Z + jets	1.8 ± 0.0	9749
$t\bar{t}$	36.0 ± 0.1	363899
tW	1.6 ± 0.0	4239
tZq	6.2 ± 0.2	27957
Total expected	107.7 ± 1.4	454983
Data	126	126

Table 5.7: Numbers of expected events in the VR-ttbar-2j1b (Left) and VR-ttbar-3j1b (Right) broken down by process. The uncertainty shown contains only the statistical component.

The $t\bar{t}$ VRs give confidence of the $t\bar{t}$ and $t\bar{t}Z$ modeling by comparing the data-MC distributions after the fit described in Chapter 9.

5.4.2 Diboson VRs Prefit Yields

Two diboson VRs are defined by exchanging the requirement of one b-tagged jet for one 'Loose' b-tagged jet as summarized in Table 5.2. A loose b-jet is defined by a jet that passses the 85% efficient working point of the MV2c10 algorithm as described in Section 3.3.1, but failing the 70% efficient nominal working point. The diboson VRs are unique in that they completely overlap with the diboson CRs, but they are enriched in VV + HF diboson events which are more relevant in the signal region. The prefit event yields in the diboson VRs after the full selection can be found in Table 5.8. The post-fit data-MC comparison is given in Section 9.4. Further pre-fit plots are provided in Appendix C.

Process	Number of events	Number of raw events
$t\bar{t}Z$	16.2 ± 0.7	11395
$t\bar{t}W$	1.2 ± 0.2	360
$t\bar{t}H$	0.5 ± 0.0	1068
tWZ	5.3 ± 0.5	741
VV + HF	87.0 ± 0.9	28586
VV + LF	172.7 ± 1.5	43227
Z + jets	7.5 ± 0.1	33306
$t\bar{t}$	2.8 ± 0.1	3648
tW	0.3 ± 0.0	58
tZq	13.5 ± 0.3	50224
Total expected	307.0 ± 2.0	172613
Data	275	275

Process	Number of events	Number of raw events
$t\bar{t}Z$	33.1 ± 1.1	25897
$t\bar{t}W$	0.7 ± 0.1	249
$t\bar{t}H$	0.8 ± 0.1	1513
tWZ	6.4 ± 0.6	1029
VV + HF	53.6 ± 0.6	18904
VV + LF	88.4 ± 0.9	25448
Z + jets	2.5 ± 0.0	25780
$t\bar{t}$	2.6 ± 0.1	2398
tW	0.2 ± 0.0	24
tZq	11.1 ± 0.3	46506
Total expected	199.3 ± 1.7	147748
Data	172	172

Table 5.8: Numbers of expected events in the VR-diboson-2j1Lb (Left) and VR-diboson-3j1Lb (Right) broken down by process. The uncertainty shown contains only the statistical component.

The diboson VRs give confidence of the diboson modeling by comparing the data-MC distributions after the fit described in Chapter 9.

Chapter 6

Modeling Fake Leptons

Events originating from $t\bar{t}$ and $Z+$jets are anticipated to have only two real leptons in the final state. In order for these backgrounds to pass selection requirements the reconstruction of a lepton not originating from the hard-scatter vertex ('non-prompt', or 'fake' lepton), is compulsory.

Fake leptons can originate from decays of bottom or charm hadrons, a jet that is misidentified as an electron, leptons from kaon or pion decays, or electrons coming from photon conversions. This is a rare occurrence and not a well modeled phenomenon by MC, mostly due to an insufficient number of MC simulated events. In order to better model backgrounds containing fake and non-prompt leptons, the origin of fakes is studied in detail and a technique known as the b-jet replacement method is used to adequately model the contribution.

6.1 Fake Lepton Origin Studies

In order to better understand the non-prompt lepton background composition, the origin of the non-prompt leptons in the trilepton final state is investigated. This is done using the MC detailed truth information and is checked for the SR-2j1b and SR-3j1b regions, as well as the relevant validation and control regions, keeping the event selection cuts described in Chapter 5.

For $t\bar{t}$ and $Z+$jets, the origins of the non-prompt or fake selected leptons can be seen in Fig. 6.1 & 6.2. The plots indicate that, in the case that the

fake lepton is a muon, the dominant source is heavy-hadron decays. In the case, instead, that the fake lepton is an electron, the dominant source are still heavy-hadron decays but with a non negligible fraction (ranging between 40 and 50 %) from photon conversions. "Not defined" leptons are leptons coming from shower-internal photon conversions that are not correctly classified by the truth-based classification algorithm (this is a feature seen in PYTHIA 8 samples). The fake background composition is similar between the different regions, with the exception of the diboson control regions that have fewer heavy-flavor jets, for each source ($Z+$jets and $t\bar{t}$) and for each lepton (electrons or muons) separately.

In Fig. 6.1 & 6.2, the fake lepton composition is also shown in the "LTT" (loose-tight-tight) regions. These regions have the same selection as the SRs, with the request that one of the leptons satisfies a loose (but not tight) selection. The loose selection requirements are reported in Table 6.1 and defined in Chapter 3. The LTT regions are dominated by fakes and are used to further validate the fake estimation described in the following.

	Loose		Tight	
	Definition	Isolation	Definition	Isolation
Electrons	MediumLH	None	TightLH	Gradient
Muons	Medium	None	Medium	Gradient

Table 6.1: Definition of electron and muon selection criteria for "loose" and "tight".

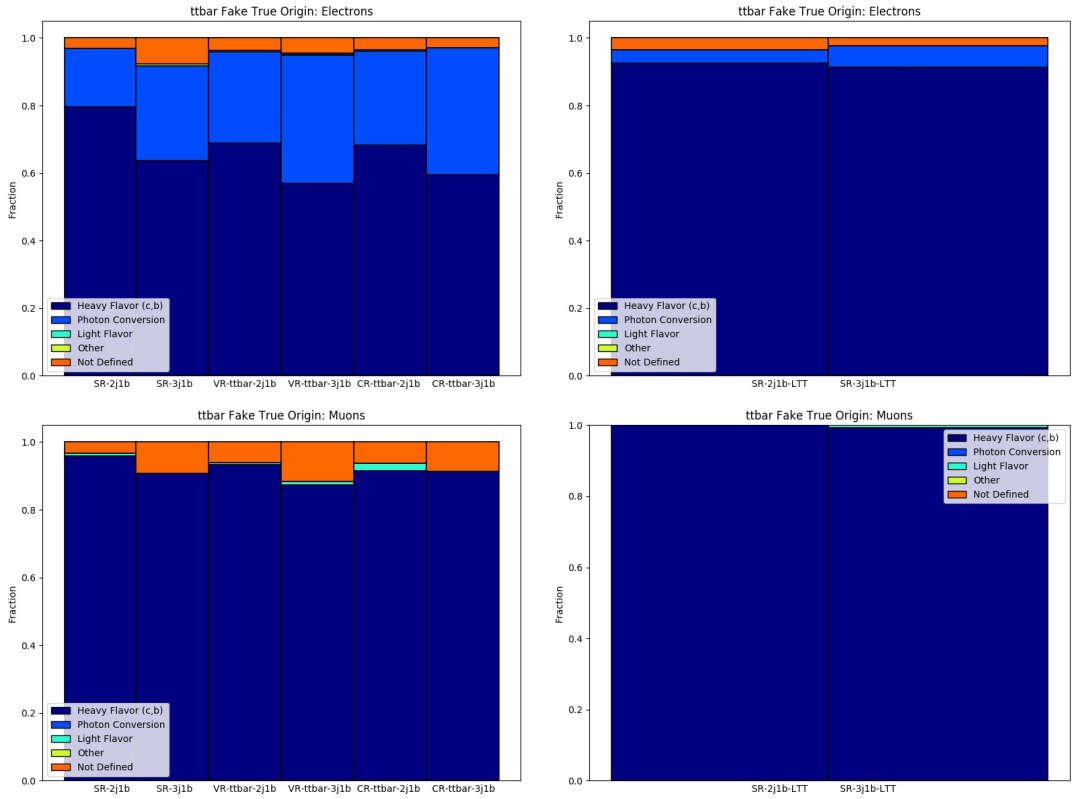


Figure 6.1: Origin of the fake electrons in the $t\bar{t}$ sample. The fraction of the different sources is shown on the y-axis. The different signal, validation and control regions are shown on the x-axis.

6.2 *b*-jet Replacement Method

The b-jet replacement method (BJR) exploits the previously justified assumption that a majority of fake leptons originate from heavy flavor (typically b-hadron) jets, and also that other sources of fakes can be modeled via perturbations of the distribution given from b-jet-originated fakes. In a nutshell, the method uses dilepton events with an extra reconstructed b-jet compared to the standard region selection and replaces one of the b-jets with an artificially generated non-prompt

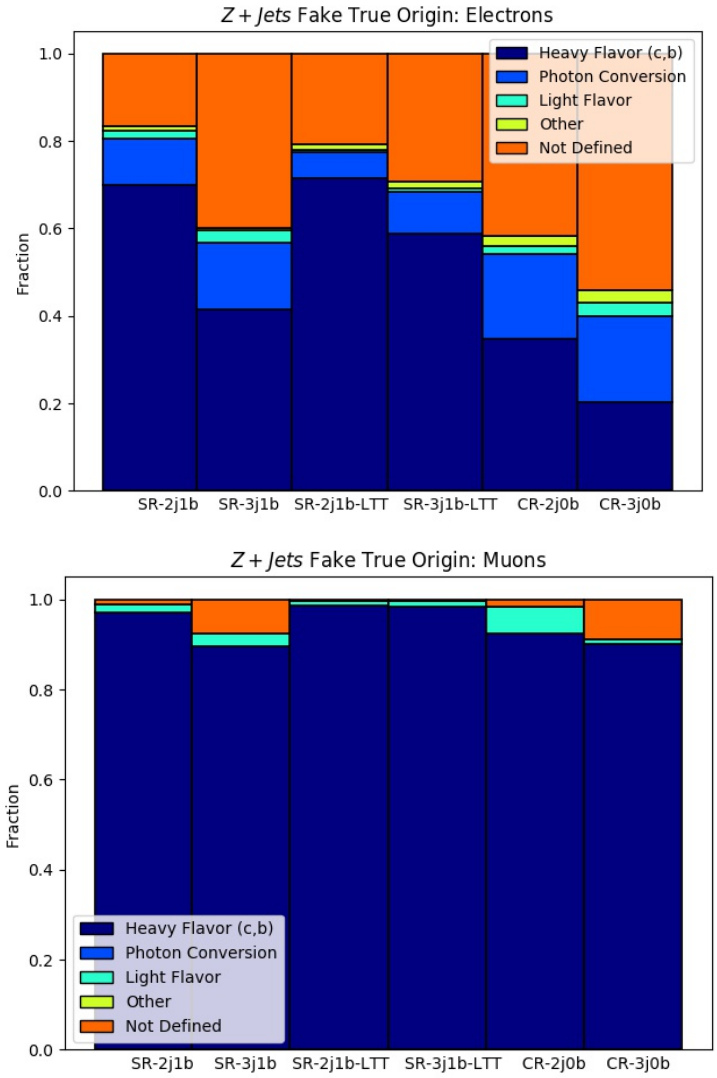


Figure 6.2: Origin of the fake electrons in the Z + jets sample. The fraction of the different sources is shown on the y-axis. The different signal, validation and control regions are shown on the x-axis. The SR-3j1b region suffers from extremely low statistics.

lepton, simulating the leptonic decay of the B hadron. The advantage of this method is that it greatly increases statistics in the non-prompt lepton samples, which in turn improves modeling and allows robust training of the neural-network in Chapter 7.

The properties of non-prompt leptons coming from b-hadron decays are studied in $t\bar{t}$ MC events in order to determine general kinematic distributions that can be sampled from in order to generate further non-prompt leptons from any b-jet. The construction of these distributions are as follows:

The momentum of a non-prompt lepton within an angular distance of $\Delta R < 0.3$ from a b-jet is boosted to the rest frame of the most energetic b quark[1] within the same jet. Improper lepton-b matching occurs a negligible fraction of the time. Using this transformed four-momentum, the energy of the lepton in the b rest-frame and its decay angle, α, are determined. The decay angle is defined as the angle between the lepton three-momentum in the b rest-frame and the b three-momentum in the laboratory frame. The distribution obtained is shown in Fig. 6.3.

This distribution is then used to create non-prompt leptons for both $Z + \text{jets}$ and the $t\bar{t}$ backgrounds. In order to estimate the fake-lepton containing backgrounds, a preselection step is applied requiring 1 more b-jet and 1 less lepton than standard event selection. Of the reconstructed b-jets in the event, one of them is selected randomly to use as a seed to generate a lepton via a sampling from the energy vs. α distribution in the b-hadron's rest frame shown in Fig. 6.3. Because

[1]The method assumes that the b-quark and the B meson have the same four-momentum.

the decay is isotropic in the b rest-frame, the azimuth about the b-jet axis of the lepton is generated randomly between 0 and 2π. Once the lepton is generated it is boosted to the lab frame using the b-jet four-momentum. Branching ratios are estimated empirically from data in the $t\bar{t}$ control regions and a value of 75 % is used for the selected b hadron decay to an electron and 25 % to a muon. Positively and negatively electrically charged electrons and muons are generated with equal probabilities.

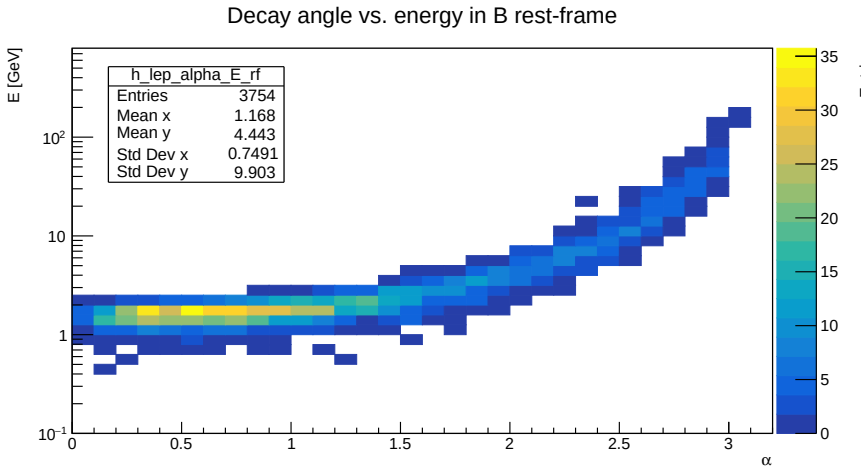


Figure 6.3: Distribution of the energy vs. the the decay angle of leptons coming from b-hadron decays, in the rest frame of the b-hadron.

This serves the purpose of increasing the statistics of the sample and does not affect the number of estimated non-prompt lepton decays since the normalization factor will be determined at a later stage by the fit. Once the lepton is generated, the b-jet is removed if it is within a angular distance of $\Delta R = 0.4$ from the lepton, similar to standard overlap removal. The results in removal of the b-jet and therefore passing of nominal event selection in greater than 95 % of events.

6.2.1 BJR normalization

The BJR method gives the shape of the fake lepton kinematics, but not its normalization. The initial yield for the BJR samples is renormalized to match the nominal MC trilepton prediction without the BJR applied. An uncertainty for each region decorrelated from one another is added to account for relative statistical fluctuations between regions of this initial estimate (Section 8.1.3). The final number of non-prompt lepton background events is determined by the fit described in Chapter 9.

6.2.2 BJR validation

In order to validate the modeling of the BJR method a comparison to data is made in the LTT regions which have a higher number of events with a fake lepton present. The most critical variables to model are the ones most significant to the neural network (Chapter 7), and the ones associated to the synthetic lepton. These variables are shown completely in Appendix D. The most difficult variable to model because of its combination of both momentum and direction of the newly created lepton, $m_{\mathrm{T}}(\mathrm{W})$, is shown in Fig. 6.4.

6.2.3 Shape comparison between various fake sources

In the following, plots comparing the shapes of different fake sources for $\mathrm{t\bar{t}}$ and $\mathrm{Z}+\mathrm{jets}$ events in 2jXb and 3jXb regions, where X stands for "any", are shown. All events in "2j" signal and control regions, are used in the same plot, and the same is done for 3j regions.

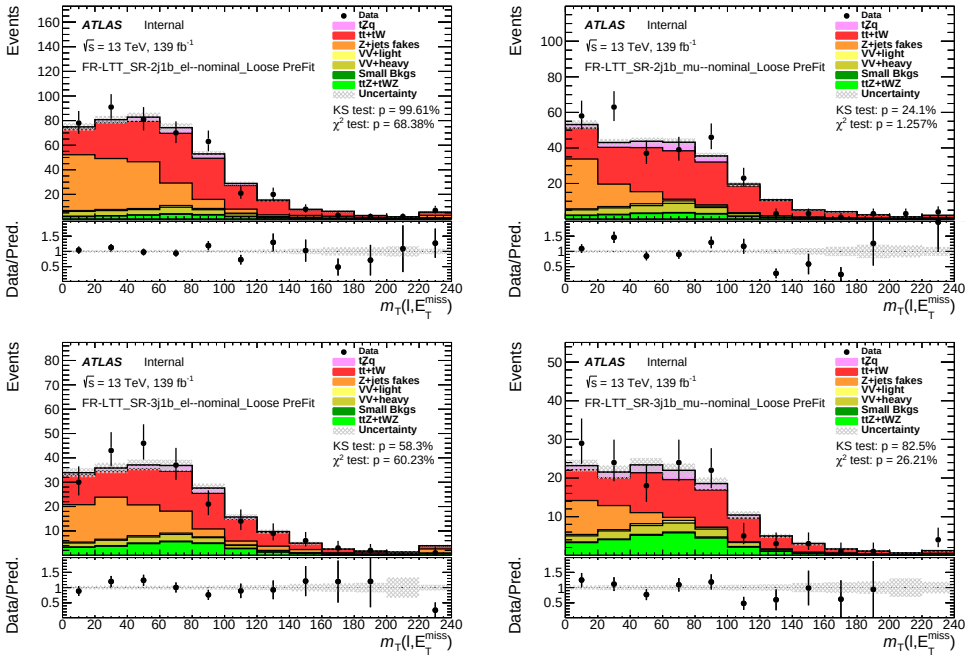


Figure 6.4: Comparison of data and MC predictions for reconstructed electron events in the SR-2(3)j1b-LTT. For further plots see Appendix D.

As shown in Fig. 6.5, different fake sources from $t\bar{t}$ have comparable shapes, while differences are visible for $Z+$jets. For this reason for $Z+$jets an additional uncertainty is added to cover the differences, but not $t\bar{t}$. This is described in Section 8. The compatibility of the post-BJR $t\bar{t}$ with data in the $t\bar{t}$ CRs and VRs also supports the exclusion of any additional systematic uncertainties on $t\bar{t}$.

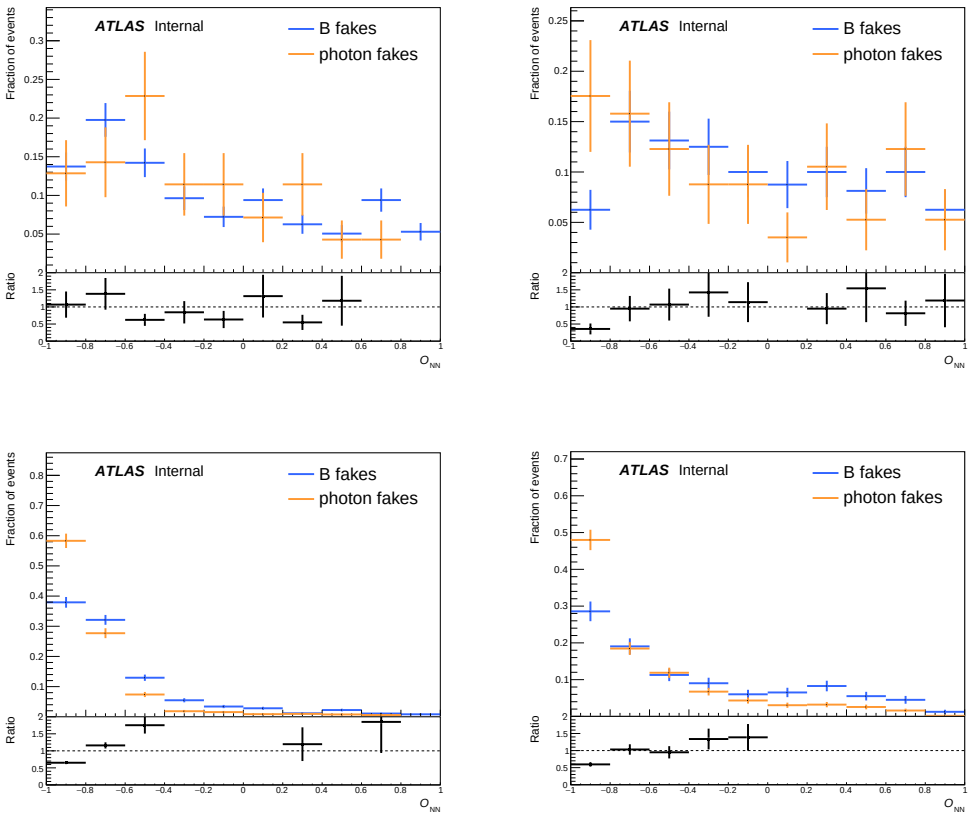


Figure 6.5: Comparison of shapes of different fake sources for $t\bar{t}$ (top) and $Z + jets$ (bottom) events in 2jXb (left) and 3jXb (right) regions with three tight leptons.

Chapter 7

Multivariate Analysis

In an effort to maximize the separation of signal and background a variable is constructed using a multivariate technique, namely a Bayesian artificial neural-network (NN). A NN provides a method of non-linear regression of multiple input variables to a variable number of outputs. A Bayesian NN implements Bayesian statistical treatment of the internal parameters' regularization. When properly marginalized the output of a Bayesian neural-network can be interpreted as a posterior probability distribution [119].

The NN used in this analysis uses the NeuroBayes framework, which combines a three-layer feed-forward neural-network with a complex robust preprocessing [120, 121]. The network architecture used consists of one input node for each input variable used (15) plus one bias node, eighteen nodes in a single hidden layer, followed by one output node which gives a continuous output in the interval $[-1, 1]$. All nodes use a sigmoid activation function, and a simple χ^2 loss function is used for optimization. Each event is weighted to represent each processes expected yield, and a global reweighting is done to balance the to expected signal to background events evenly.

A distinct training optimization campaign is done for the SR-2j1b and SR-3j1b separately resulting in two neural-networks, one specialized for the two-jet final state and one for the three-jet. In order to chose input variables all possible reconstructed variables are used in an initial NN training. A correlation matrix

of all variables is calculated and the least correlated variable with the output of the loss function is dropped from the training. This process is done iteratively until fifteen variables are kept. There is very small gain in performance to be had by keeping more than fifteen variables. These variables are different for the two main signal regions and are given in Tables 7.1 and 7.2. Their modeling shows reasonable agreement with data, as well as distinguishability of tZq in Section 7.1.

Variable	Corr. loss [%]	Definition
$m_{\mathrm{bj_f}}$	43.3	Invariant mass of the b-jet and the forward jet
m_t	34.7	Reconstructed top-quark mass
$\lvert\eta_{j_f}\rvert$	18.6	Absolute value of the forward jet η
$m_{\mathrm{T}}(l, E_{\mathrm{T}}^{\mathrm{miss}})$	12.7	Transverse mass of the W boson
b-tagging score	9.5	b-tagging score of the b-jet
H_{T}	6.0	Scalar sum of the p_{T} of the selected particles in the event
$q(\ell^{\mathrm{W}})$	6.0	Electric charge of the lepton from the W-boson decay
$\lvert\eta(\ell^{\mathrm{W}})\rvert$	4.9	Absolute value of the η of the lepton from the W-boson decay
$p_{\mathrm{T}}(\mathrm{W})$	3.5	p_{T} of the reconstructed W boson
$p_{\mathrm{T}}(\ell^{\mathrm{W}})$	4.5	p_{T} of the lepton coming from the W-boson decay
$m(\ell\ell)$	4.5	Mass of the reconstructed Z boson
$\lvert\eta(\mathrm{Z})\rvert$	4.4	Absolute value of the η of the reconstructed Z boson
$\Delta R(j_f, \mathrm{Z})$	4.1	ΔR between the forward jet and the reconstructed Z boson
$E_{\mathrm{T}}^{\mathrm{miss}}$	3.8	Missing transverse momentum
$p_{\mathrm{T}}(j_f)$	3.3	Forward jet p_{T}

Table 7.1: Variables used as input to the neural-network of the 2j1b SR ordered by their importance. The 2nd column gives the correlation the loss function.*More detailed definitions of some variables in App. E.*

To maximize the training statistics a technique of five-folded template assembly

Variable	Corr. loss [%]	Definition
$m_{\mathrm{bj_f}}$	43.0	Invariant mass of the b-jet and the forward jet
m_t	31.8	Reconstructed top-quark mass
$\lvert\eta_{j_f}\rvert$	17.4	Absolute value of the forward jet η
$m_{\mathrm{T}}(l, E_{\mathrm{T}}^{\mathrm{miss}})$	12.3	Transverse mass of W-boson
$\lvert\eta(j_r)\rvert$	12.0	Absolute value of the radiation jet η
$p_{\mathrm{T}}(\mathrm{Z})$	10.2	p_{T} of the reconstructed Z boson
$\Delta R(j_f, \mathrm{Z})$	8.1	ΔR between the forward jet and the reconstructed Z boson
$q(\ell^{\mathrm{W}})$	7.8	Electric charge of the lepton from the W boson decay
$p_{\mathrm{T}}(\mathrm{j_r})$	6.7	p_{T} of the radiation jet
$p_{\mathrm{T}}(\mathrm{j_f})$	5.6	p_{T} of the forward jet
b-tagging score	5.2	b-tagging score of the b-jet
$\lvert\eta(\ell^{\mathrm{W}})\rvert$	4.2	Absolute value of the η of the lepton coming from the W-boson decay
$\lvert\eta(\mathrm{Z})\rvert$	3.9	Absolute value of the η of the reconstructed Z boson
$p_{\mathrm{T}}(\ell^{\mathrm{W}})$	2.5	p_{T} of the lepton coming from the W boson decay
$p_{\mathrm{T}}(\mathrm{W})$	3.5	p_{T} of the reconstructed W boson

Table 7.2: Variables used as input to the neural-network of the 3j1b SR ordered by their importance. The 2nd column gives the correlation with the loss function. *More detailed definitions of some variables in App. E.*

is used. In this method, five NNs are trained per signal region on 80 % of the available MC events and a histogram template is created by evaluating the NN on the remaining test set of 20 %. The five templates are then summed to create the final template used for statistical comparison in Chapter 9. The construction of the template from events not present in the training nearly eliminates the possibility for bias in the templates. Each of the five NNs use orthogonal events for the 20 % test set to further eliminate possible over-fitting. After all training is complete and data is to be evaluated by the NNs, each data event is scored by one of the five NNs at random. When evaluating the NN classifier on an event containing a variable outside of the bounds of the SRs, a value of -999 is used as an input for said variable thus preventing bias.

To demonstrate the lack of over-training and to show the performance of the NN, the receiver operating characteristic (ROC) for all training folds and the final test template for each signal region is shown in Fig. 7.1. A diagonal line with a slope of 1 would represent an even 50:50 mix of signal and background events for all O_{NN} values and no separation power between the two. The tendency for the curve to reach up and to the left displays the signal and background grow at different rates, and the separation can be quantitatively inferred by the following: for any point on the curve a value of O_{NN} exists such that the signal and background events are present at or below said value at efficiencies given by the ROC curve. The coincidence of all 5 training fold and the single test fold ROC curves demand that all training and test events perform equally, concluding the lack of over-training.

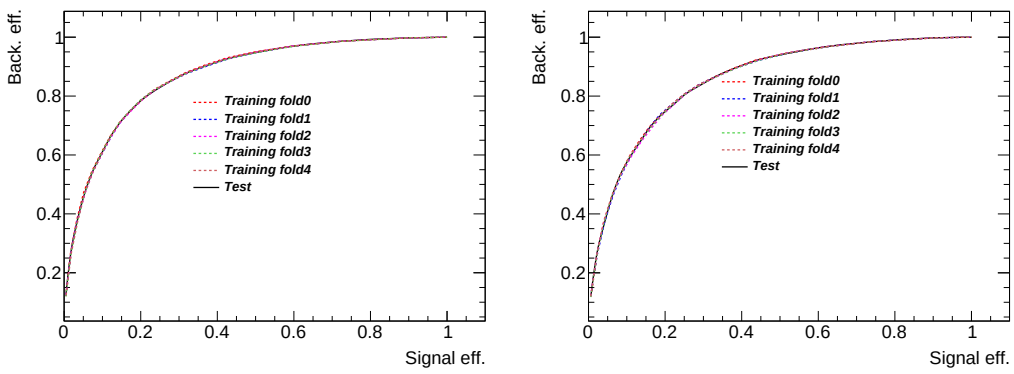


Figure 7.1: Neural-network ROC curve of the training and test samples of the 2 jet SR (left) and of the 3 jet SR (right). The hashed curves are created from the training samples of each fold and the solid curves are created from the test samples.

7.1 Input variable distributions

The modeling of the input variables must be well described by MC in order to validate the assumption that the training of the NN on MC events be also applicable to data. There should also be distinguishability of tZq from background events present in the input variable distributions. All input variables used in the multivariate analysis are shown in the following figures that compare simulated to LHC data in order to illustrate that they adequately modeled. Overlain distributions normalized to unity in order to compare input shapes are given in Fig. 7.2-7.5, and stacked histograms showing the data-MC comparison are given in Fig. 7.6-7.9.

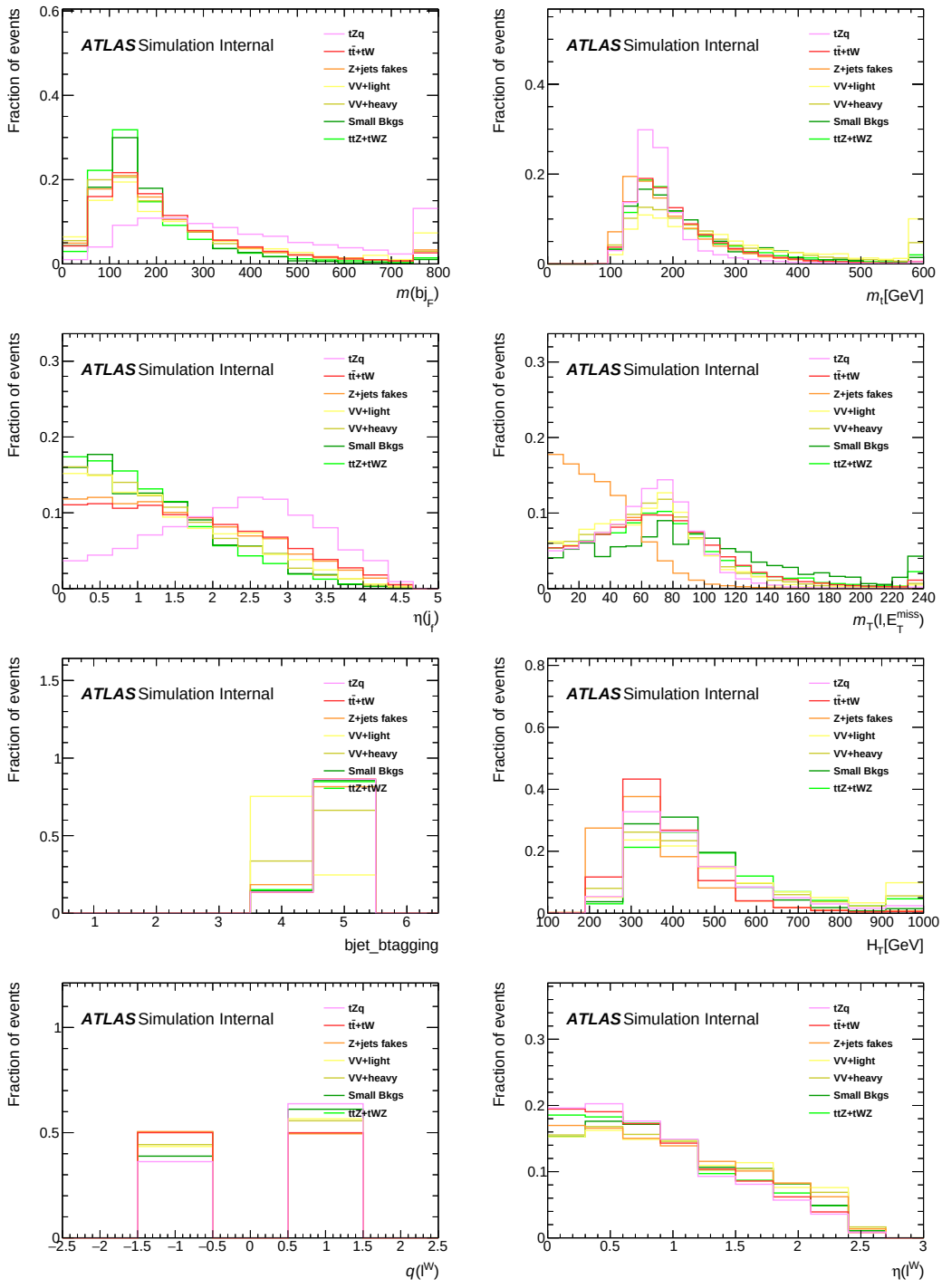


Figure 7.2: Normalised kinematic plots of neural-network training variables of the 2j1b SR, in order of significance. "bjet_btagging" refers to the pseudo-continuous b-tagging score.

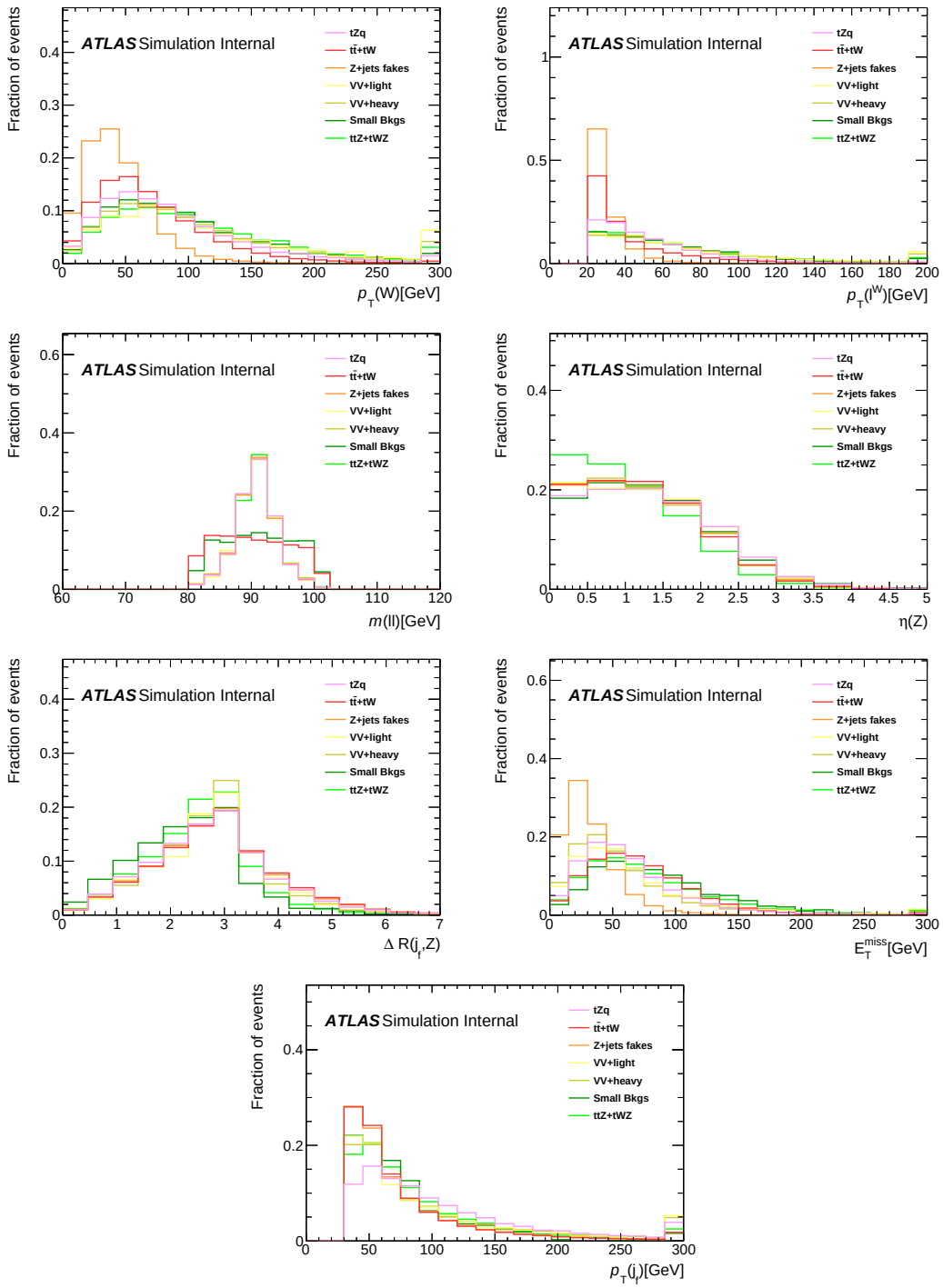


Figure 7.3: Normalised kinematic plots of neural-network training variables of the 2j1b SR, in order of significance.

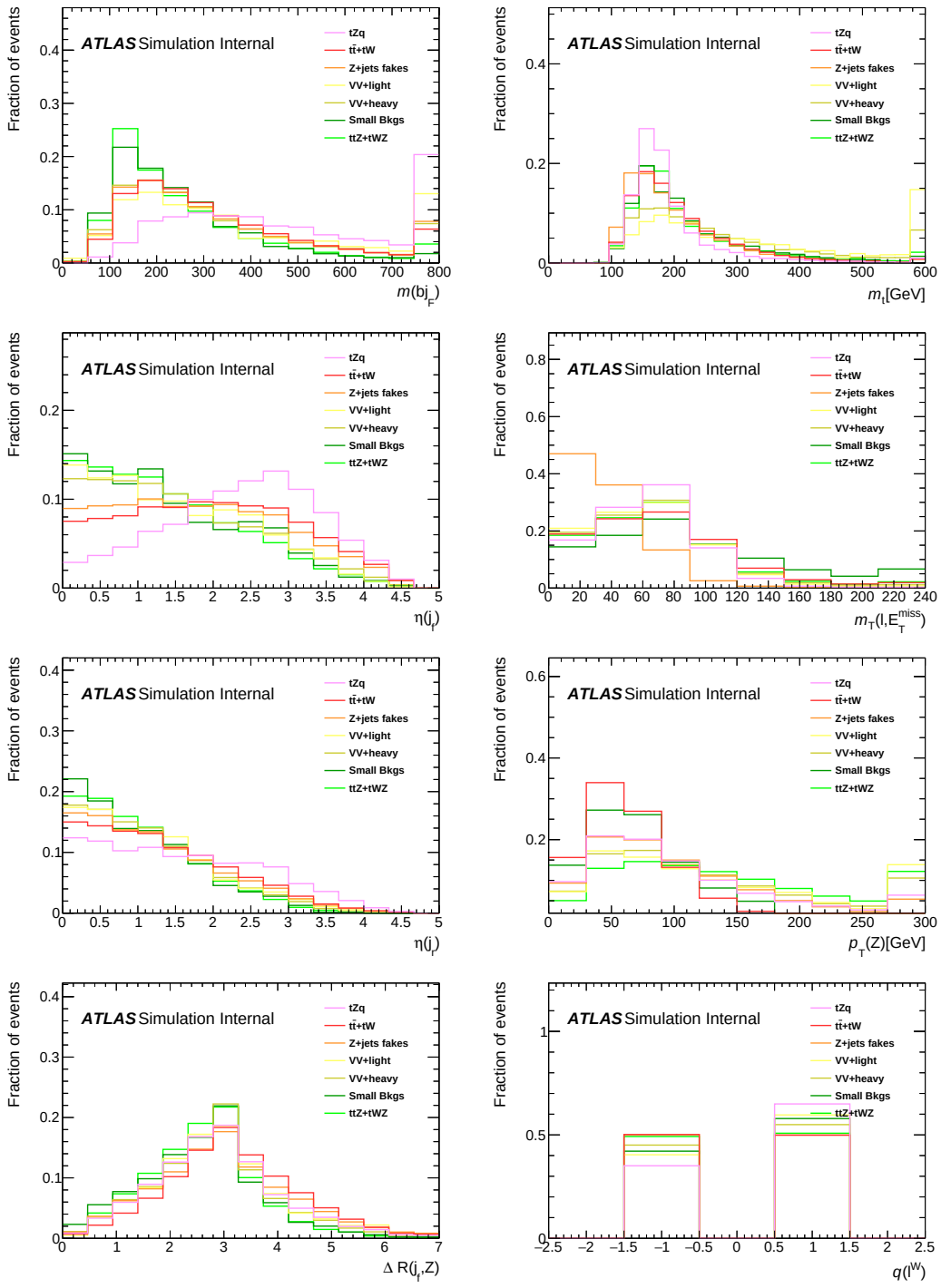


Figure 7.4: Normalised kinematic plots of neural-network training variables of the 3j1b SR, in order of significance.

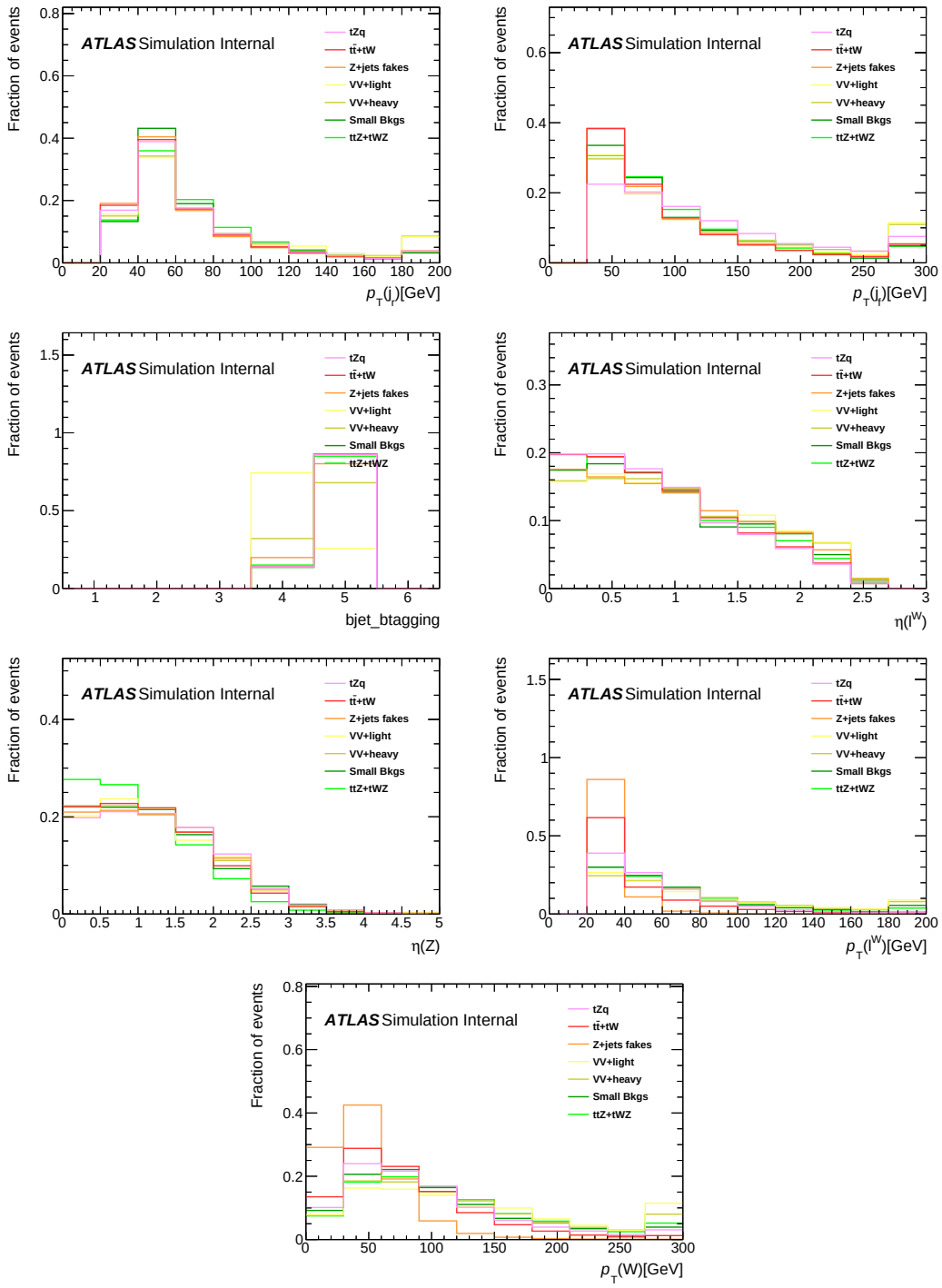


Figure 7.5: Normalised kinematic plots of neural-network training variables of the 3j1b SR, in order of significance. "bjet_btagging" refers to the pseudo-continuous b-tagging score.

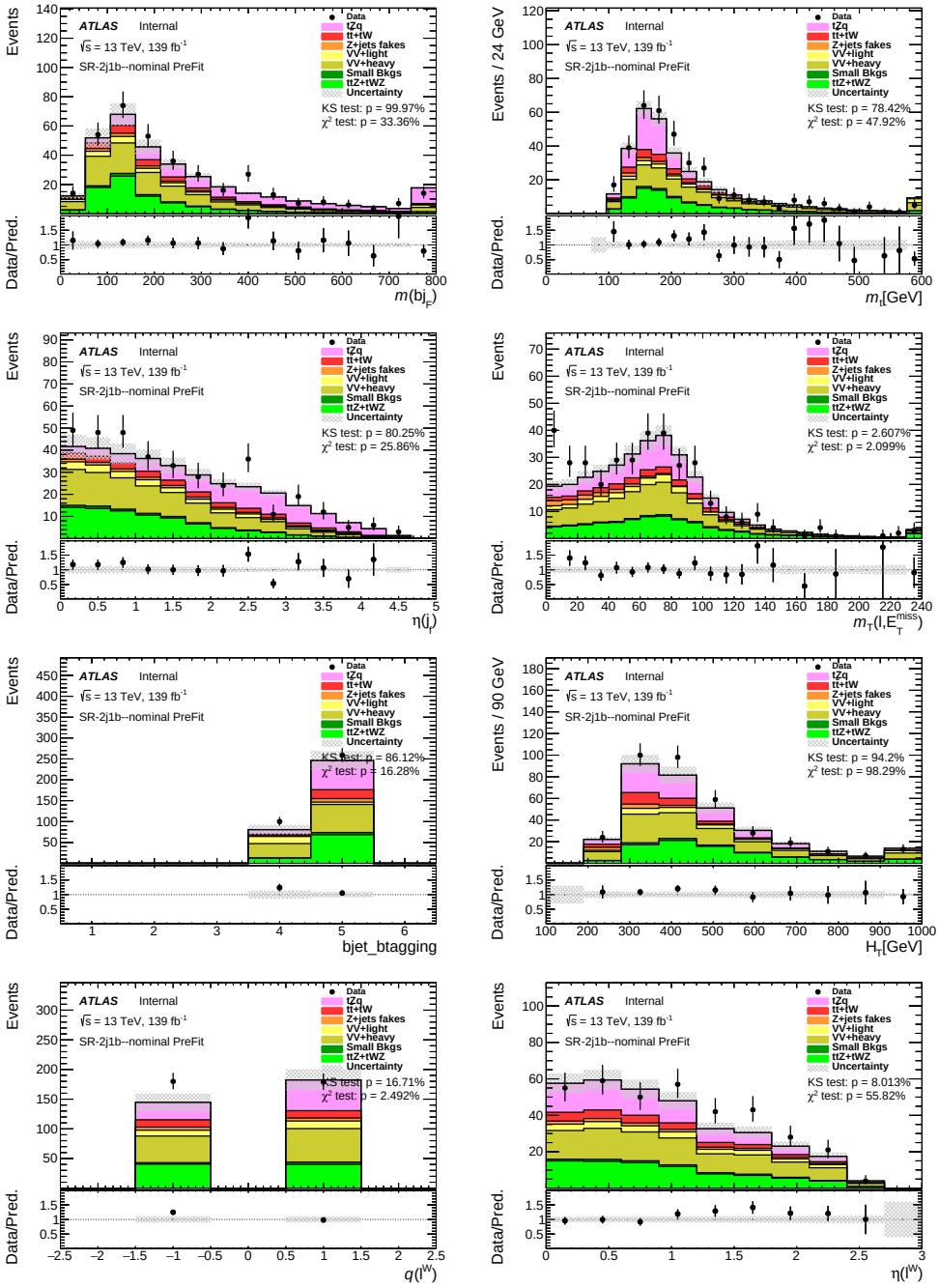


Figure 7.6: Stacked kinematic plots of neural-network training variables of the 2j1b SR, in order of significance. "bjet_btagging" refers to the pseudo-continuous b-tagging score.

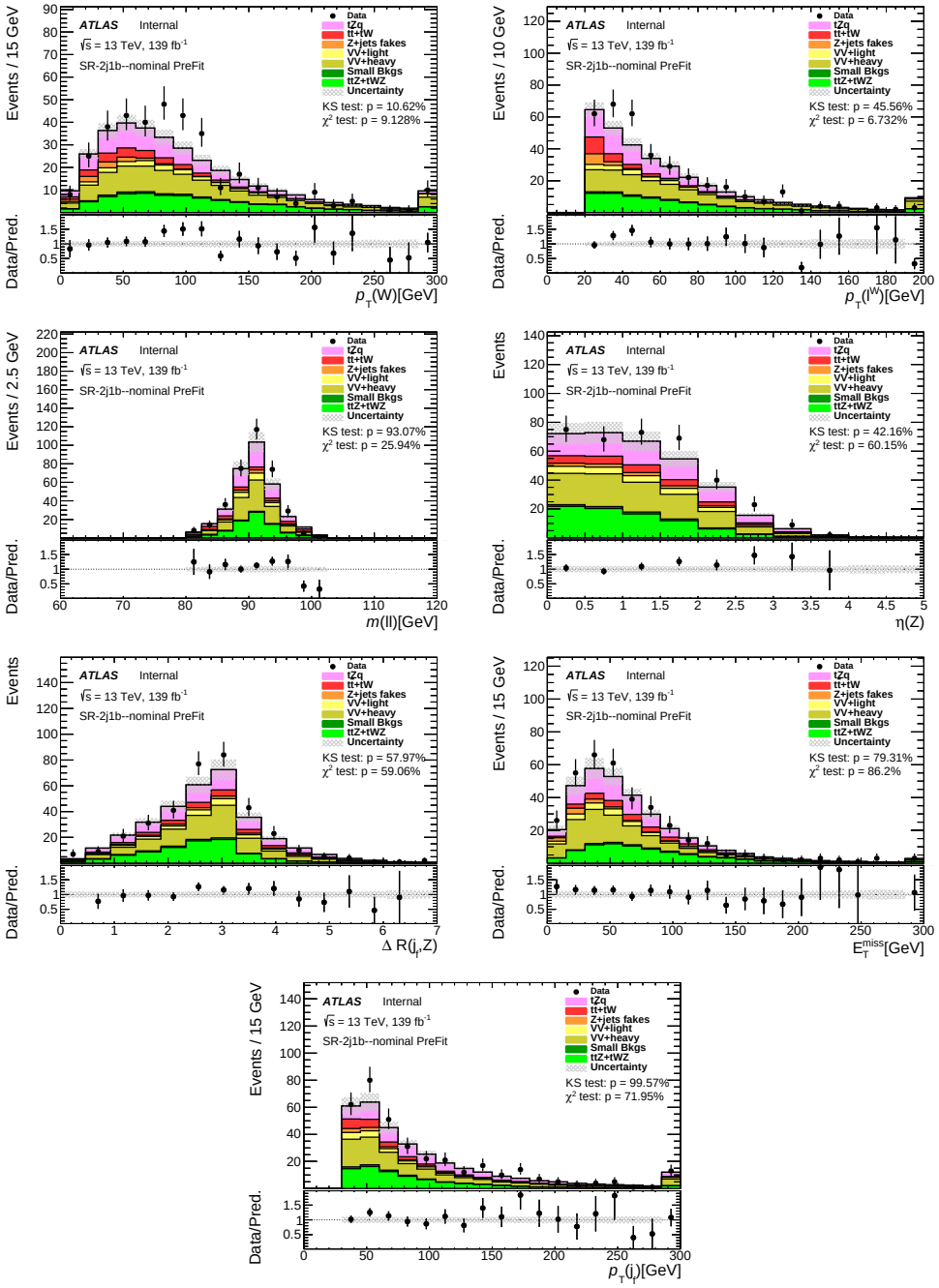


Figure 7.7: Stacked kinematic plots of neural-network training variables of the 2j1b SR, in order of significance.

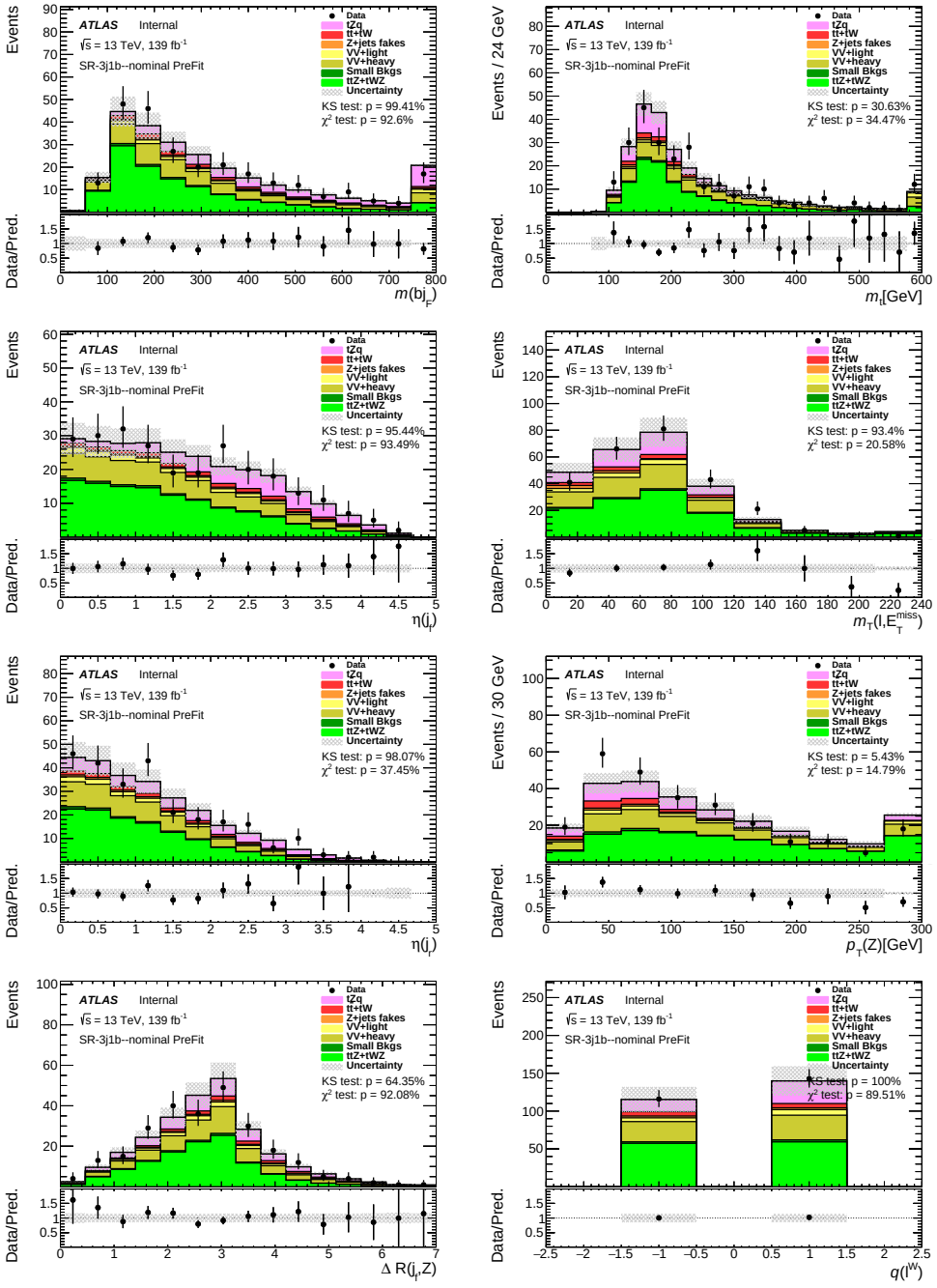


Figure 7.8: Stacked kinematic plots of neural-network training variables of the 3j1b SR, in order of significance.

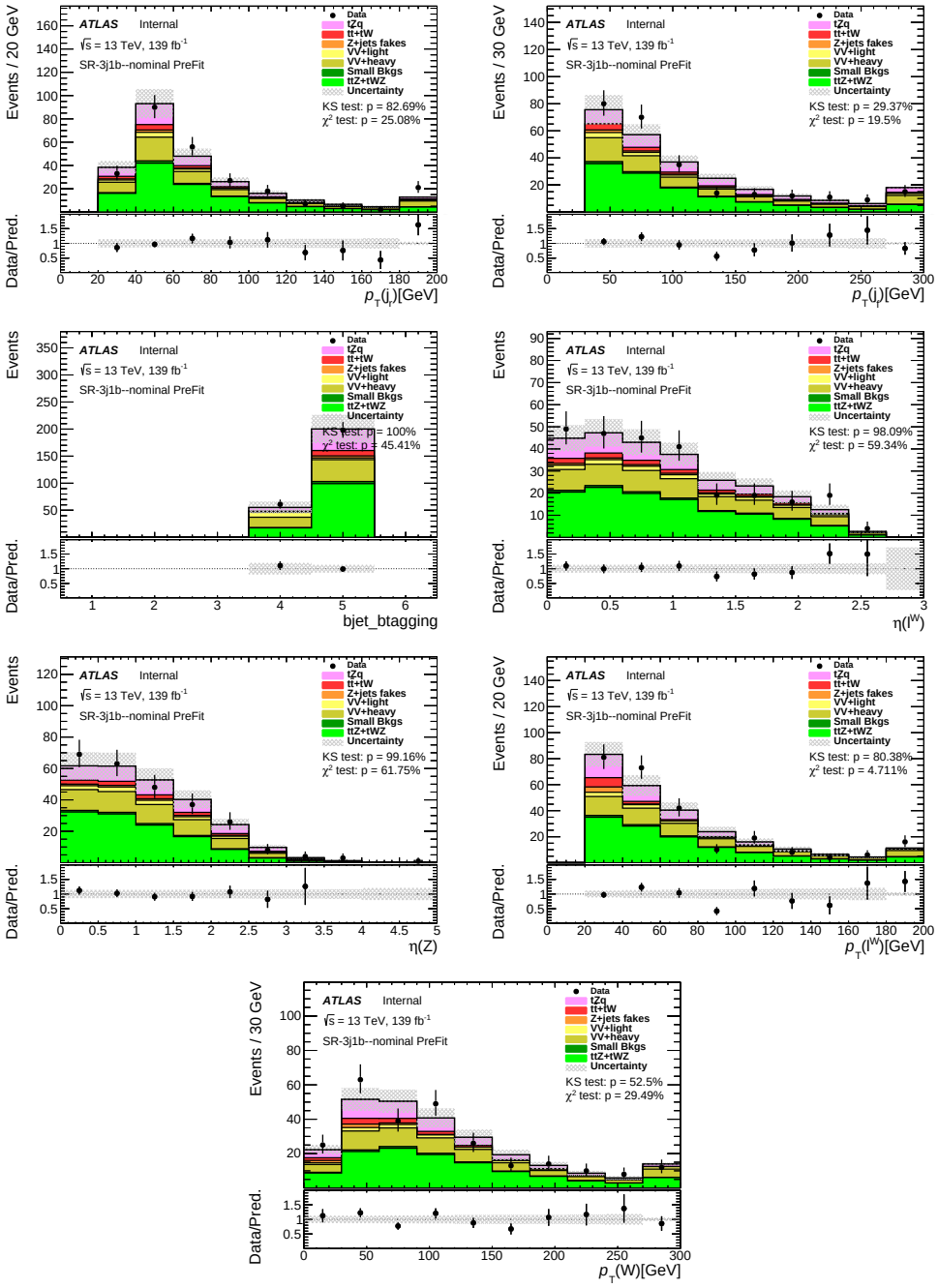


Figure 7.9: Stacked kinematic plots of neural-network training variables of the 3j1b SR, in order of significance. "bjet_btagging" refers to the pseudo-continuous b-tagging score.

7.2 Neural-network output distributions in the SRs

The normalized template distributions of the neural-network output of the 2j1b and 3j1b SRs for signal and backgrounds are shown in Fig. 7.10. The final O_{NN} distribution for both signal regions is shown in Fig. 7.11.

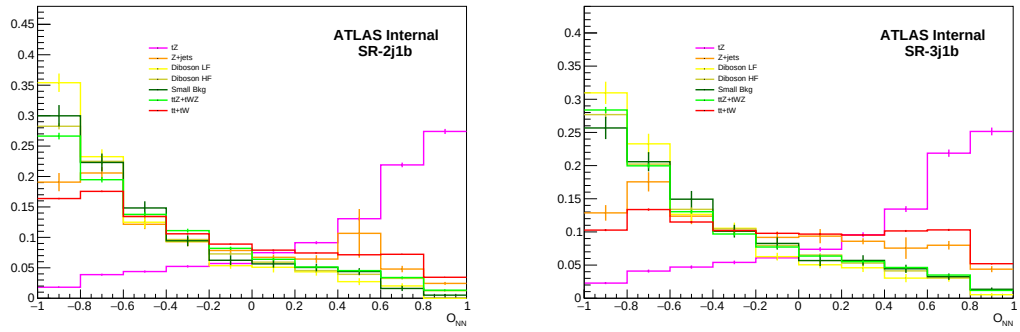


Figure 7.10: Shapes of the NN output in the SRs, in the 2j1b SR (left) and in the 3j1b SR (right).

A good separation between the signal and backgrounds is seen, demonstrating that using the neural network should lead to an improved cross-section measurement.

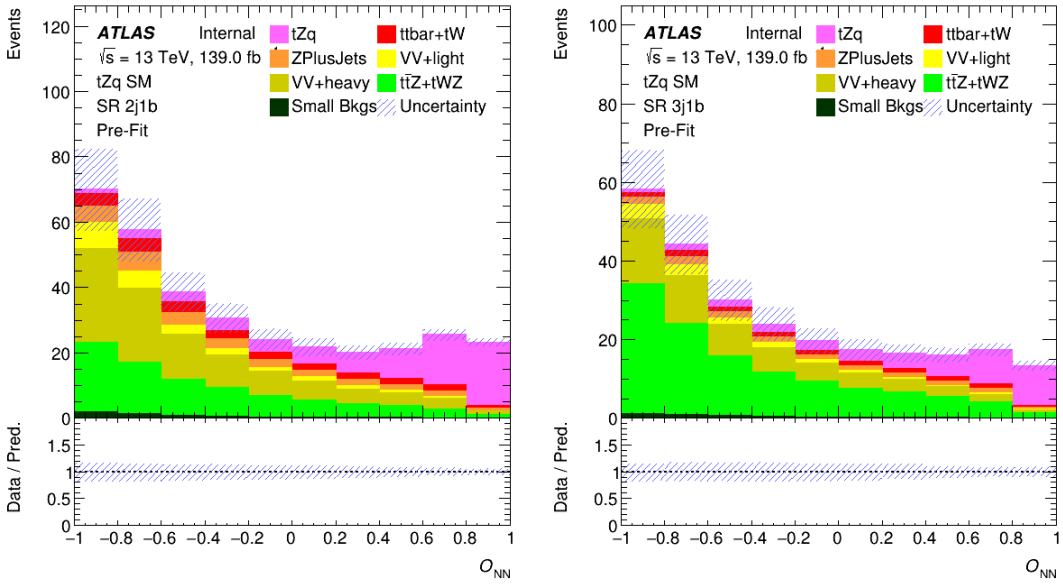


Figure 7.11: Output of the NN in the SRs, in the 2j1b SR (top) and in the 3j1b SR (bottom). The uncertainty shown contains all sources of statistical and systematic error.

Chapter 8

Systematic Uncertainties

Many sources of systematic uncertainties are considered in the extraction of the tZq cross section. Each source of systematic uncertainty effects the predicted signal and background modeling. This can effect the overall yield, or can impact object reconstruction to augment the predicted templates' shape. The impact of each uncertainty is propagated to each histogram bin's yield and is constrained by individual Gaussian nuisance parameters (NP) in the maximum likelihood fit. More on the statistical implementation of systematic uncertainties is provided in Chapter 9.

The evaluation of systematic uncertainties is performed using the common top group prescription and standard ATLAS procedures, with additional analysis or method specific systematics. A breakdown of each systematic type and their method of evaluation is given in the following.

8.1 Sources of Systematic Uncertainty

8.1.1 Object energy scale/resolution

Systematic uncertainties due to residual differences between data and Monte Carlo simulations, for jets, electron and muon reconstruction after calibration, as well as uncertainties on the calibration scale factors are propagated to the event yields and observables:

- **Lepton reconstruction:**

  The mis-modeling of muon (electron) trigger, reconstruction and selection efficiencies in simulation is corrected by introducing scale factors derived from measured efficiencies in data. $Z \to \mu^+\mu^-$ ($Z \to e^+e^-$) decays are used to obtain scale factors as functions of the lepton kinematics. The uncertainties are evaluated by varying the lepton and signal selection and from the uncertainties in the background evaluations [67, 122].

- **Lepton momentum scale and resolution:**

  The $Z \to \ell\ell$ processes are again used to measure the lepton momentum scale and resolution. Calibration factors and associated uncertainties are derived to match the simulation to observed distributions in collision data. The effect of momentum scale uncertainties is evaluated by repeating the event selection after varying the lepton momentum up by 1σ and down by 1σ. For the momentum resolution uncertainties the event selection is repeated by smearing the lepton momentum [123].

- **Jet energy scale (JES):**

  The JES was derived using information from test-beam data, LHC collision data and simulation. The JES calibration consists of several steps that account for detector non-uniformity, jet reconstruction algorithms, jet fragmentation models, dense data-taking environment from high pile-up conditions and response difference between data and MC simulation. There are a total of 33 separate components used in this thesis to handle each

individual source of uncertainty on the JES. The general trend of all components' fractional uncertainty is an inverse relationship with the p_{T} of the reconstructed jet and is rather stable in η [124]. The jet calibration procedure is described in more detail in Ref. [125].

To take into account the fact that the major backgrounds have different fraction of jets originating from quarks and gluons, the JES component associated with jet flavor composition is decorrelated into four NPs: VV+LF, VV + HF, $\mathrm{t\bar{t}Z}$ and a fourth which is correlated among all other samples.

- **Jet energy resolution:**

  The impact of the uncertainty on the jet energy resolution is evaluated by smearing the jet energy in the MC samples by the known detector resolution (Section 3.3). The jet energy resolution is measured using in-situ techniques, and the uncertainty on the resolution is applied in the analysis by varying the smearing-distribution by the measured uncertainty on the resolution [126].

- **Jet vertex tagger:**

  The uncertainty for the JVT requirement is also applied varying the tracking a vertexing parameters by their detector resolutions (Section 3.3).

- **Missing transverse momentum:**

  Uncertainties of the soft-track component are derived from the level of agreement between data and MC simulation of the p_{T} balance between the hard and soft $E_{\mathrm{T}}^{\mathrm{miss}}$ components. Three different uncertainties are considered: an offset along the p_{T} (hard) axis, as well as the smearing resolution along

and perpendicular to the p_{T} (hard) axis (Section 3.4).

- **b-tagging efficiency:**

  The b-tagging efficiencies and mis-tag rate for the taggers have been measured in data using the same methods as described in [127, 128]. The impact on the tZq cross-section measurement due to the uncertainties of the b-tagging data/MC scale factors is evaluated separately for b, c and light-flavor quark jets in the MC samples. The flavor tagging algorithms cover a large dimensional phase space of correlated independent variables. In an effort to reduce file size and increase computational speed, a principal component analysis is done to map the relevant sources of uncertainty onto a basis of 85 separate vectors. This includes orthogonal components that codify the migration from different working points.

8.1.2 Monte Carlo and PDF modeling:

Systematic effects from MC modeling are estimated by comparing different MC generators and varying parameters for the event generation. These are previously detailed in Section 4.2. The uncertainty due to finite MC statistics is taken into account when constructing the likelihood function in Section 9.1.

PDF uncertainty:

The systematic uncertainties related to the parton distribution functions are taken into account for the signal only. The events are reweighted according to each of the PDF uncertainty eigenvectors. The uncertainties are calculated using the formula given in Equation 43 of Ref. [129]. The uncertainty is calculated, following

the new PDF4LHC recommendation [130], of the estimated uncertainties for the PDF4LHC15 PDF set. This ultimately leads to the root-mean-squared of each eigenvector's impact being used to create a single systematic uncertainty NP.

8.1.3 Background rate uncertainty:

Each background process has an uncertainty on the expected overall rate.

The $t\bar{t}Z$ background normalization is constrained by an uncertainty of 12 % on the cross section, which is taken from [131]. For the diboson background, the normalization uncertainty is taken to be compatible with ATLAS results [132, 133] to be 30 %. For $t\bar{t}W$ and $t\bar{t}H$ (combined) a 15 % systematic uncertainty on the normalization is used.

For the backgrounds that utilize the b-jet replacement method the normalization of the background templates are a free unconstrained parameter in the fit. There is however, a normalization uncertainty of 15 % for Z + jets and 7 % for $t\bar{t}$ independently for each relevant region to allow freedom for the relative yields between different regions to adjust to the fit. These values correspond to the characteristic Monte Carlo statistical uncertainty of the Z + jets and $t\bar{t}$ samples in SRs and the relevant CRs.

8.1.4 BJR shape uncertainty:

To account for the possible slight differences in shape of Z + jets events originating from sources other than semi-leptonic B-hadron decays, a systematic uncertainty on the shape of the Z + jets distribution is applied. The systematic uncertainty

is constructed by comparing the shapes of Monte Carlo events from different sources separated by their origin of the fake lepton in the event (e.g.: heavy flavor decay, photon conversion, etc.). The magnitude of the difference in the shape,(i.e. bin-by-bin scale factors), is scaled by the relative contribution of the non-semi-leptonic contribution of total Z + jets events, which is taken to be approximately 25 % for SR-Xj1b and 50 % for CR-Xj0b. These weighted scale factors are then applied to the nominal BJR Z + jets templates to create a 2 point systematic in the control and signal regions. These uncertainties are shown in Fig. 8.1.

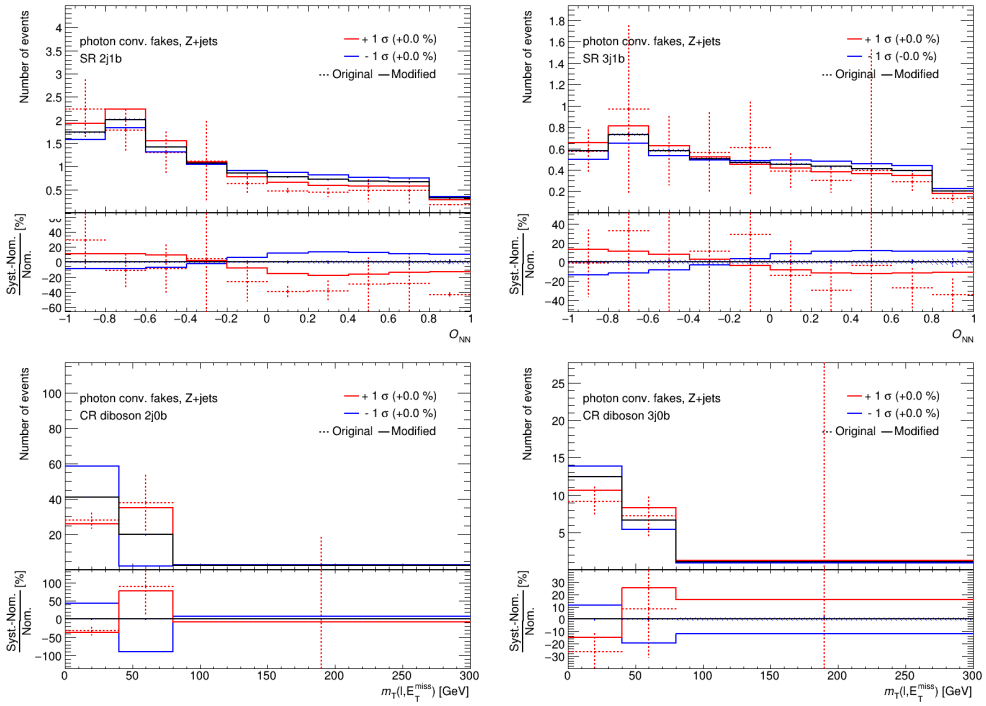


Figure 8.1: Z + jets BJR shape uncertainty.

8.1.5 Luminosity

The uncertainty in the combined 2015–2018 integrated luminosity is 1.7 %. It is derived following a methodology similar to that detailed in Ref. [134] from the calibration of the luminosity scale using x–y beam-separation scans, as well as measurements by the LUCID-2 sub-detector [45, 46].

8.1.6 Uncertainty on pile-up reweighting

The impact of pileup on the analysis is modeled by simulating zero-bias proton-proton collision events that are used to define reweighting factors that account for effects due to pileup for all simulated events in the analysis. Uncertainties on these scale factors from multiple sources described in Ref. [89] are included as a systematic uncertainty.

8.2 Symmetrizing, Smoothing, and Pruning

The systematic uncertainties discussed above cause variations on the signal acceptance, the background rates, and the shape of the distributions that are used in the fit. The effect of each systematic uncertainty, j, has the yield and acceptance of each bin present in the fit calculated and fully correlated into a single nuisance parameter α_j. To codify the degree of impact α_j has on each bin, the analysis is re-calculated varying each systematic uncertainty independently up and/or down by an estimated 1σ variation. The variation from nominal for each bin, i, and systematic, j: σ_{ij+} and σ_{ij-}, are used to create a coefficient of α_j as shown in

Eq. 9.2 for each bin and systematic. In calculating this coefficient, all systematic uncertainties containing both up and down systematic variations are symmetrized via $(\sigma_{ij+} + \sigma_{ij-})/2 = \sigma_{ij}$. For some systematics only a single up or down variation is estimated. In these cases σ_{ij} is then defined as: $\sigma_{ij-} = \sigma_{ij+} = \sigma_{ij}$. An exception is the MC statistic uncertainties which use a separate NP for each histogram bin in the fit (Eq. 9.1).

Due to low statistics systematic uncertainties can suffer from fluctuations in individual bins causing unrealistic shape deformations. A smoothing of systematic shape uncertainties is performed to average adjacent bins' systematics's magnitude to remove statistical fluctuations. To simplify the fit and reduce computational time, NPs that inflict a less than 0.5% impact on the tZq normalization are pruned from the fit (Chap. 9).

Chapter 9

Statistical Analysis

In order to extract the tZq cross-section, a binned maximum-likelihood fit is performed using the MC templates for both signal and background predictions with an unconstrained parameter of interest: the normalization of the signal template [135]. To evaluate the statistical significance as well as evaluate postfit uncertainties of model parameters, a profiled likelihood approach is used. The software framework used for performing the fit is `TRExFitter` [136]. This combines the functionalities of `RooFit` [137] and `RooStats` [138] and is designed to construct the likelihood function from all histogram bins from both the signal and control regions.

9.1 Likelihood Function and Fitted Parameters

The likelihood function used is constructed as the product of independent Poisson distributions, one for each histogram bin, multiplied by a product of nuisance-parameter Gaussian constraint terms for each of the systematic uncertainties discussed in section 8, and also a Poisson distribution for each bin to include the impact of the uncertainty on the background prediction due to MC statistical uncertainty:

$$\mathcal{L}(\vec{\mu},\vec{\theta}) = \prod_i \frac{\gamma_i \nu_i^{n_i} \mathrm{e}^{-\gamma_i \nu_i}}{n_i!} \times \prod_j \mathrm{e}^{-\alpha_j^2} \times \prod_i \mathrm{P}_i(\gamma_i) \tag{9.1}$$

The number of data events observed per bin is listed as n_i, the nuisance parameters incorporating MC uncertainties as γ_i, and each bin's prediction ν_i has the form:

$$\nu_i = \vec{\mu} \cdot \vec{P}_i + \sum_j \alpha_j \sigma_{ij}. \tag{9.2}$$

The matrix $\vec{P}_i$ is the predicted number of events of each physics process for bin i, and the vector $\vec{\mu}$ is either a completely unconstrained normalization coefficient in the case of $\mathrm{tZ}q$ and backgrounds estimated using the b-jet-replacement-method or a constant value of 1 for non-floating background predictions. The effect of all systematic uncertainties are included in the predicted number of events via the second term in Eq. 9.2 with the variable definitions detailed in Section 8.2.

This negative log-likelihood is numerically minimized in the parameter-space of 3 unconstrained 'μ' ($\mathrm{tZ}q$, $\mathrm{Z}+\mathrm{jets}$, and $\mathrm{t\bar{t}}$), 34 'γ', and $\sim$200 'α' parameters after pruning. The fitted value of the normalization of $\mathrm{tZ}q$ (μ_0) times the calculated cross section is then interpreted as the inclusive cross section measurement. In order to calculate the statistical significance of observed $\mathrm{tZ}q$ events the asymptotic approximation [139] of the likelihood is used with the CL_s method to define the test statistic [140].

9.2 Fitted Regions

The SRs included in the fit are designed to maximize sensitivity to the parameter of interest (POI), and the CRs are carefully designed to maximally constrain all other parameters in the fit so as to have maximum information extraction of the POI. The regions and distributions that are fit are summarized in Table 9.1. The

definitions of the various regions are shown in Table. 5.2. For the SRs and $t\bar{t}Z$ CRs the O_{NN} distribution is used in the fit. For the diboson CRs the $m_{\mathrm{T}}(\mathrm{W})$ distribution is used to separate and therefore constrain the $\mathrm{Z}+\mathrm{jets}$ prediction. For the $t\bar{t}$ CRs a single bin is fit due to relatively low statistics so the variable is irrelevant.

Region	Distribution	Additional info
SR-2j1b	O_{NN}	–
SR-3j1b	O_{NN}	–
CR-2j0b	$m_{\mathrm{T}}(\ell, E_{\mathrm{T}}^{\mathrm{miss}})$	–
CR-3j0b	$m_{\mathrm{T}}(\ell, E_{\mathrm{T}}^{\mathrm{miss}})$	–
CR-ttbar-2j1b	–	single bin
CR-ttbar-3j1b	–	single bin
CR-3j2b	O_{NN}	–
CR-4j2b	O_{NN}	–

Table 9.1: Overview of the regions included in the fit.

9.3 Fit Results

The results of the maximum-likelihood estimator fit to data in the SRs is shown in Fig. 9.1 and the CRs in Fig. 9.2. The numerical post-fit yields are compiled in Table 9.2. These show a reasonable agreement with the SM prediction.

The post-fit correlation matrix in Fig. 9.3 shows the most correlated parameters

	SR 2j1b	CR diboson 2j0b	CR $t\bar{t}$ 2j1b	CR $t\bar{t}Z$ 3j2b
tZq	79 ± 11	53.1 ± 7.5	0.2 ± 0.1	12.9 ± 2.0
$t\bar{t}$ + tW	23.8 ± 4.8	13.7 ± 2.7	33.3 ± 6.3	1.7 ± 0.3
Z + jets	28 ± 13	179 ± 81	< 0.1	1.4 ± 0.6
VV + LF	19.7 ± 7.9	2000 ± 100	< 0.1	0.1 ± 0.1
VV + HF	101 ± 22	383 ± 78	0.4 ± 0.1	5.2 ± 1.7
$t\bar{t}Z$ + tWZ	95 ± 11	62.8 ± 6.9	4.7 ± 0.5	59.3 ± 7.1
$t\bar{t}H$ + $t\bar{t}W$	6.5 ± 1.0	3.0 ± 0.5	12.4 ± 1.9	2.8 ± 0.5
Total	354 ± 16	2697 ± 56	51.1 ± 6.1	83.5 ± 6.4
Data	359	2703	49	92

	SR 3j1b	CR diboson 3j0b	CR $t\bar{t}$ 3j1b	CR $t\bar{t}Z$ 4j2b
tZq	43.4 ± 6.2	21.2 ± 3.3	0.2 ± 0.1	8.0 ± 1.3
$t\bar{t}$ + tW	11.0 ± 2.2	6.9 ± 1.3	15.4 ± 3.1	1.0 ± 0.2
Z + jets	12.8 ± 6.0	53 ± 23	< 0.1	0.4 ± 0.2
VV + LF	10.1 ± 4.2	624 ± 53	< 0.1	0.1 ± 0.1
VV + HF	59 ± 17	187 ± 50	0.3 ± 0.1	3.3 ± 1.0
$t\bar{t}Z$ + tWZ	132 ± 12	61.9 ± 6.2	3.9 ± 0.5	58.1 ± 5.3
$t\bar{t}H$ + $t\bar{t}W$	4.7 ± 0.7	1.7 ± 0.3	8.2 ± 1.3	2.0 ± 0.3
Total	272 ± 12	955 ± 29	28.0 ± 3.0	72.8 ± 5.0
Data	259	949	31	75

Table 9.2: Post-fit SR and CR yields.

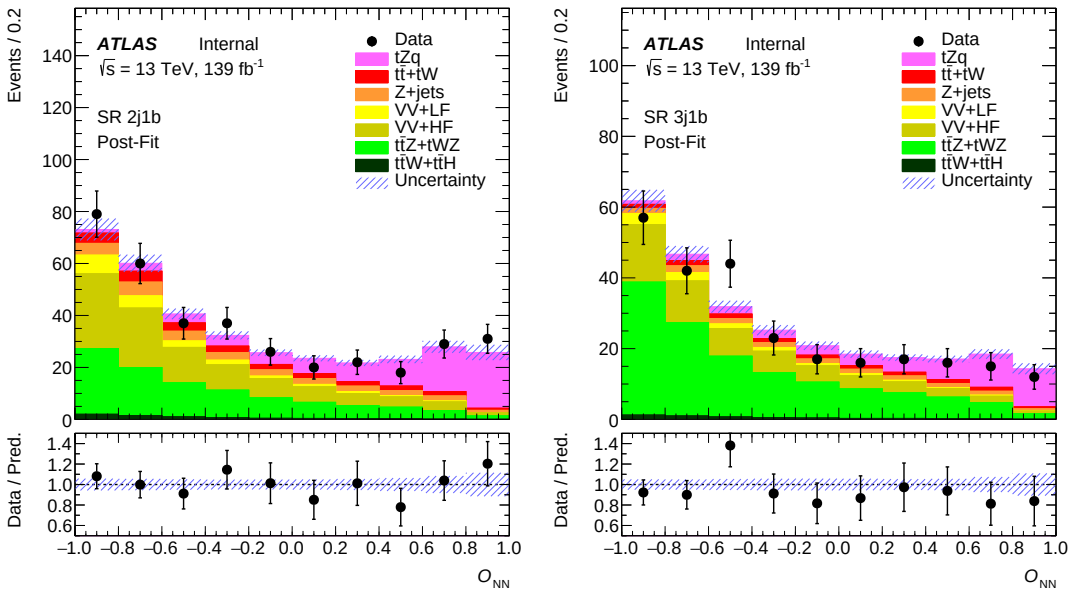


Figure 9.1: Analysis post-fit results of SR regions.

in the fit. The low correlation between the POI and other variables demonstrates the well designed fit configuration to minimize effects of background modeling uncertainties. One can also see the inter-dependence of the different diboson flavors with one another, as well as the expected influence of different shape uncertainties of Z + jets and $t\bar{t}Z$ on their respective normalizations.

The post-fit values of the unconstrained $\vec{\mu}$ parameters, including the POI, are given in Fig. 9.4. The Z + jets normalization is pulled up slightly to accommodate the data, mostly driven by the the CR-Xj0b regions, but is still within a reasonable 1.5 σ from the prediction. This large fluctuation of the free floating background normalization is not unexpected due to the Z + jets background's relatively small contribution to the fit as well as the b-jet-replacement's rough estimate of the prefit normalization. The POI also shows good agreement with the SM within about a 14% uncertainty. The post fit values of the γ parameters associated to

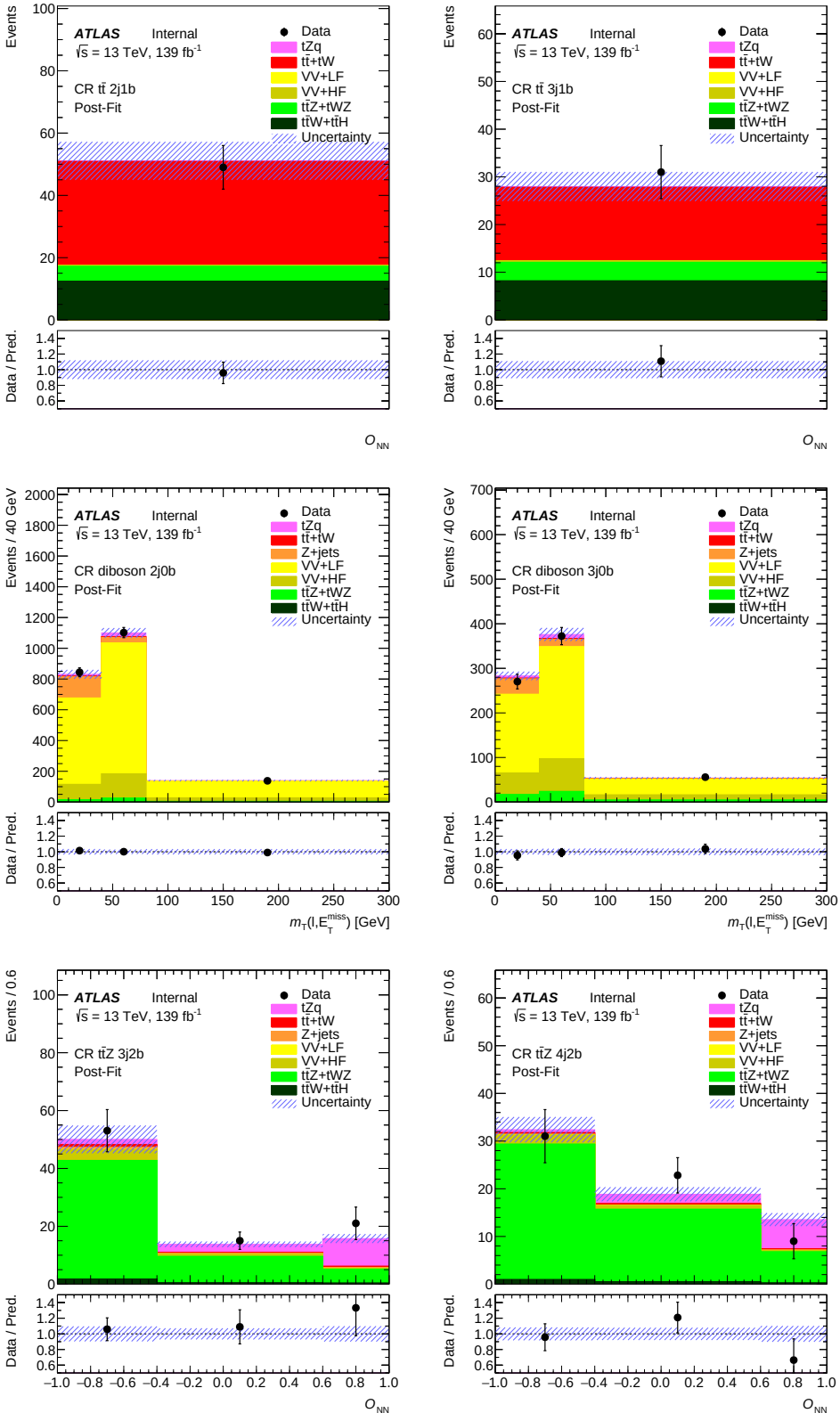


Figure 9.2: Analysis post-fit results of CR regions.

MC statistics is shown in Fig. 9.5. The post-fit uncertainty of these parameters is on the order of 1-2%. The post fit 1 σ value for all parameters are calculated by scanning each parameter value while keeping all others constant (profiled) until the value of the likelihood function doubles. To speed up this calculation, a quadratic approximation of the likelihood function is used to obtain the 1 σ values of systematic uncertainties analytically [141].

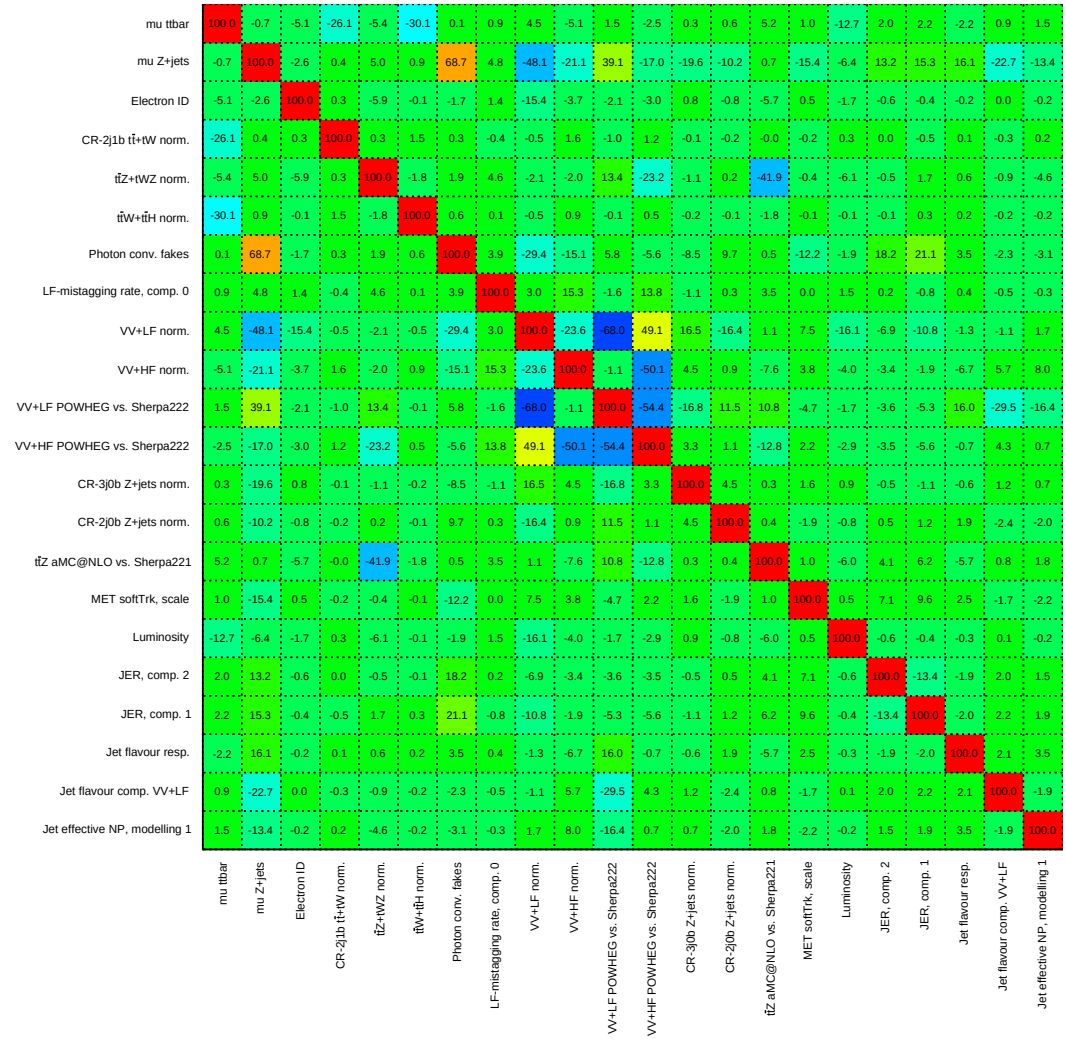


Figure 9.3: Estimate of the correlation matrix of all parameters in the fit that show a single correlation greater than 10%.

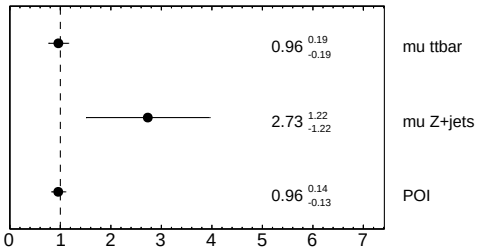


Figure 9.4: Analysis post-fit values of unconstrained normalization parameters.

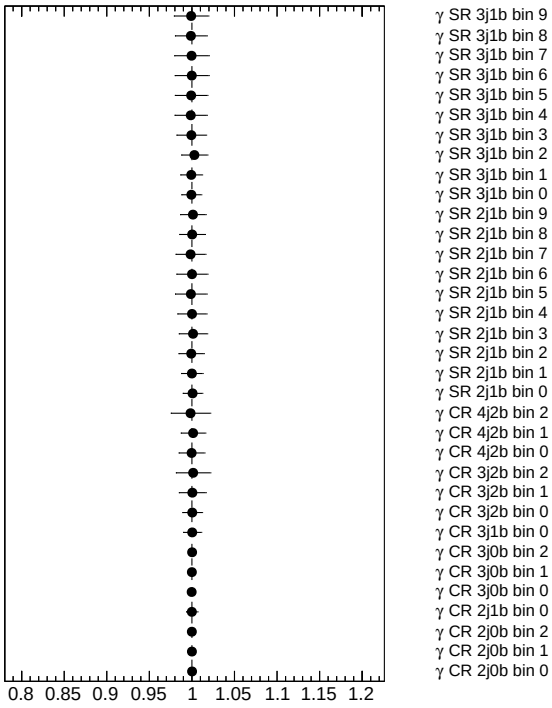


Figure 9.5: Analysis post-fit 'γ' parameters associated with MC statistics.

An important thing to consider is how each parameter in the fit impacts the POI. In order to do this the fit is performed whilst constraining each parameter by its ± 1 σ condition one at a time, then calculating the difference that occurs in the POI. From this one can deduce which systematics have the highest impact on the measurement. The most important systematics are ranked in Fig. 9.6 with

their impact quantified by the blue bands lain underneath their pull distributions.

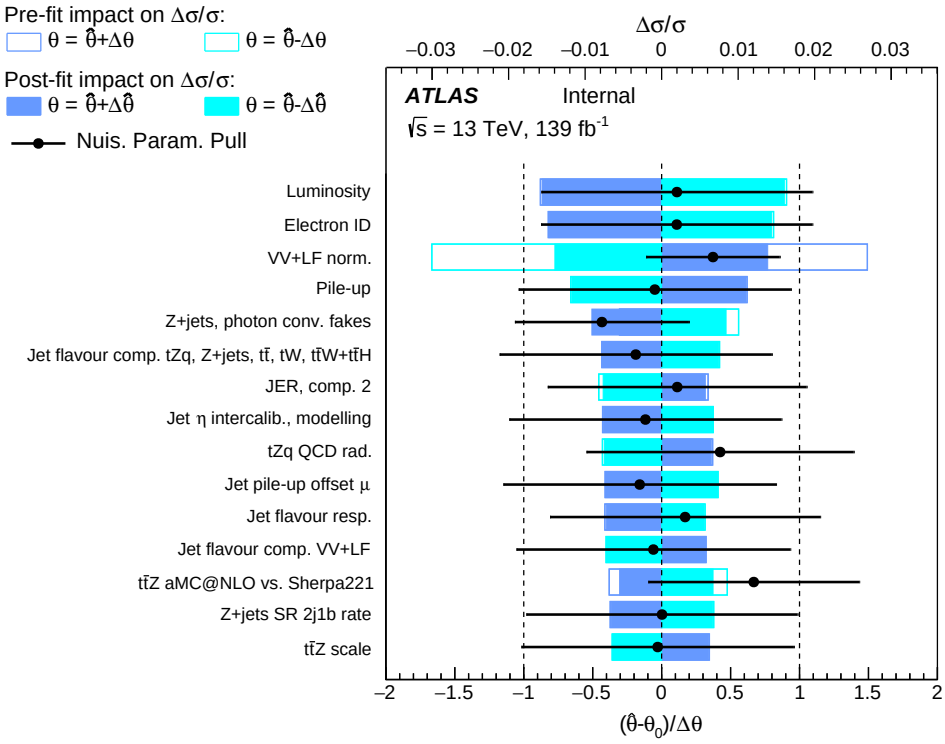


Figure 9.6: Ranking of each parameters impact on the POI. The pre- and post-fit impact of the parameter is shown via the blue bands, underneath its pull distribution.

The total impact of all uncertainties is evaluated for each category and compiled in Table 9.3. The systematic uncertainties are calculated the same as Fig. 9.6 but for all systematics in each category simultaneously. The total statistical uncertainty is calculated by subtracting in quadrature the systematic uncertainty from the total uncertainty.

After the fit has been calculated and the values of the fitted parameters are extracted, histograms of the most significant variables to the neural network are plotted to further survey the compatibility of model to data. These are shown in

Fig. 9.7 & 9.8. The most discrepant histogram bin is found in the m_t distribution of the SR-3j1b, but given the total number of histogram bins examined it is not statistically unlikely to find such an outlier. The satisfactory modeling of these critical variables builds confidence to interpretations of the results of the fit as real physical quantities.

Uncertainty source	$\Delta\sigma/\sigma$ [%]
Prompt lepton background modeling and normalization	3.3
Jets+$E_{\mathrm{T}}^{\mathrm{miss}}$	2.0
Lepton reconstruction and calibration	2.0
Luminosity	1.7
Non-prompt lepton background modeling	1.6
Pileup	1.2
MC statistics	1.0
tZq QCD radiation	0.8
tZq PDF	0.7
b-tagging	0.4
Total systematic uncertainty	7.0
Data statistical	12.6
Floating normalizations	2.1
Total statistical uncertainty	12.9

Table 9.3: Table of systematics' impact on the POI uncertainty grouped together based on origin.

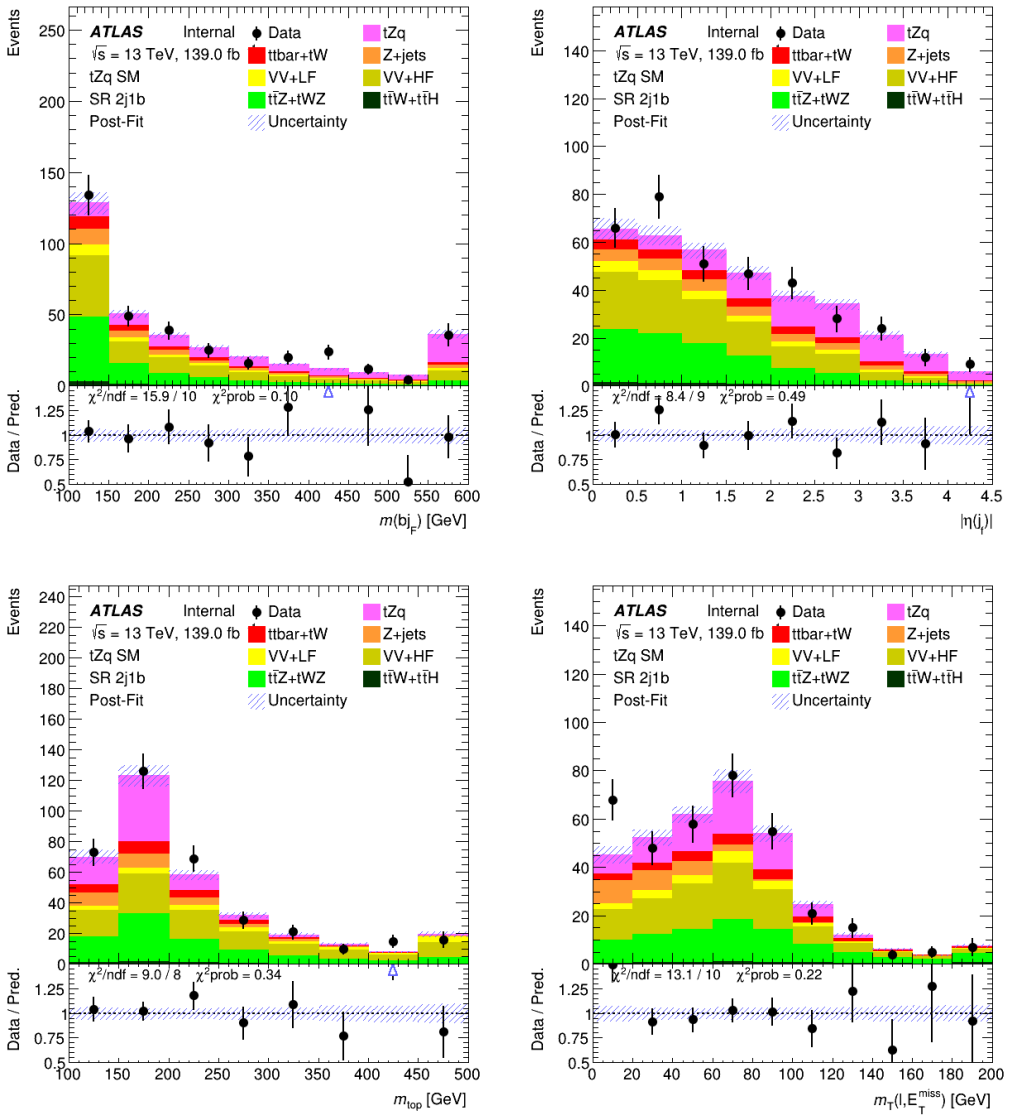


Figure 9.7: Comparison of data and MC predictions for the most significant variables to the neural network in the SR-2j1b region using postfit values of fitted parameters.

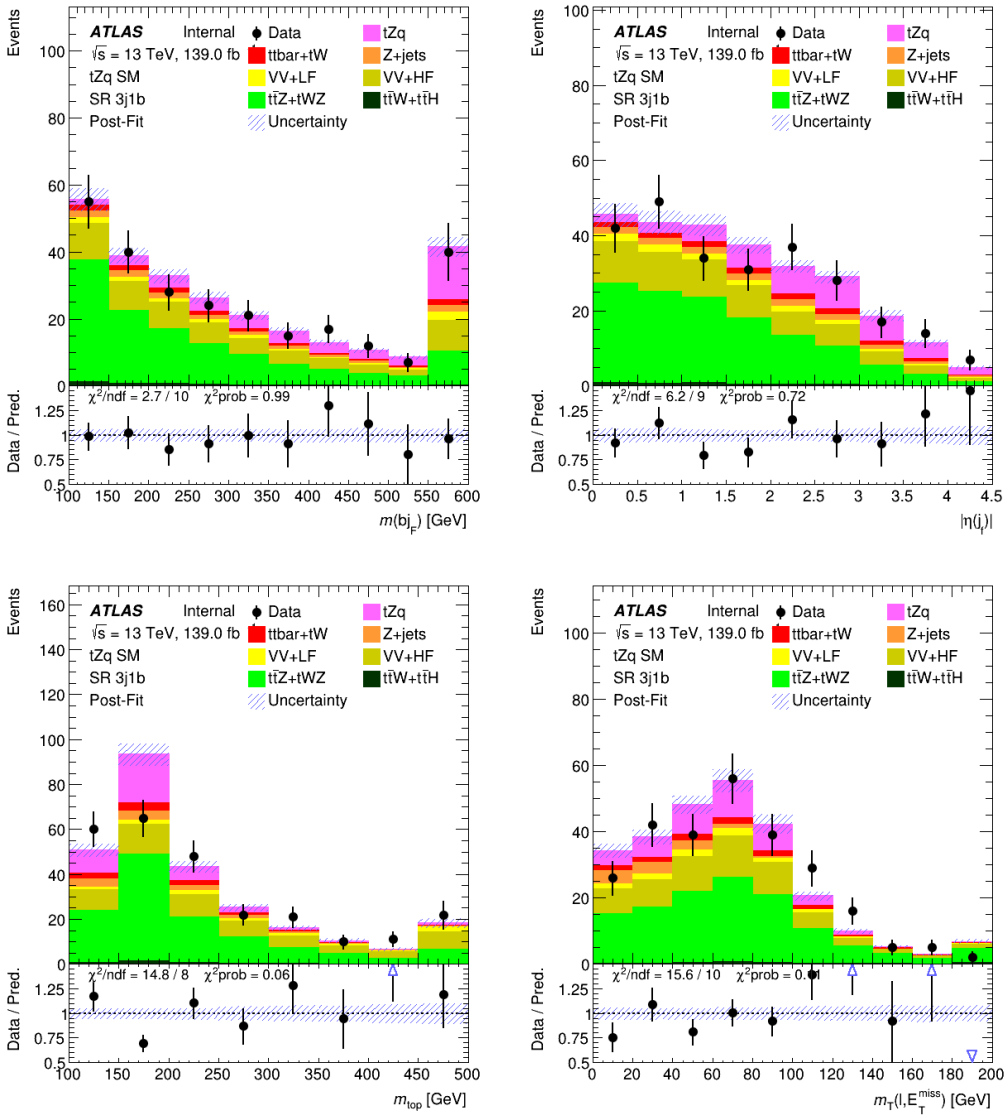


Figure 9.8: Comparison of data and MC predictions for the most significant variables to the neural network in the SR-3j1b region using postfit values of fitted parameters.

9.4 Post-fit modeling in VRs

In order to build further confidence in the modeling, the post-fit modeling in the validation regions' O_{NN} distribution described in Section 5.4 is compared to data in Fig. 9.9. The post-fit yields are given in Table 9.4. These regions are not included in the fit, so their adequate modeling post-fit suggests the statistical procedure is indeed attempting to describe the physical phenomenon taking place.

	VR 2j1Lb	VR 2jLb	VR $t\bar{t}$ 2j1b	VR $t\bar{t}$ 3j1b
tZq	13 ± 2	11 ± 1.7	10 ± 1.5	5.9 ± 0.9
$t\bar{t}$ + tW	2.7 ± 0.5	2.5 ± 0.5	81 ± 16	36 ± 7
Z + jets	20.2 ± 9	6.6 ± 3	13 ± 6	5 ± 2
VV + LF	155.7 ± 27.0	73 ± 15	4 ± 2	2 ± 1
VV + HF	88 ± 18	53 ± 16	19 ± 4	11 ± 3
$t\bar{t}Z$ + tWZ	23 ± 2.6	42 ± 4	24 ± 3	30 ± 3
$t\bar{t}H$ + $t\bar{t}W$	1.7 ± 0.3	1.5 ± 0.3	31 ± 5	21 ± 3
Total	304 ± 25	190 ± 14	182 ± 16	111 ± 7
Data	275	172	169	126

Table 9.4: Post-fit VR yields.

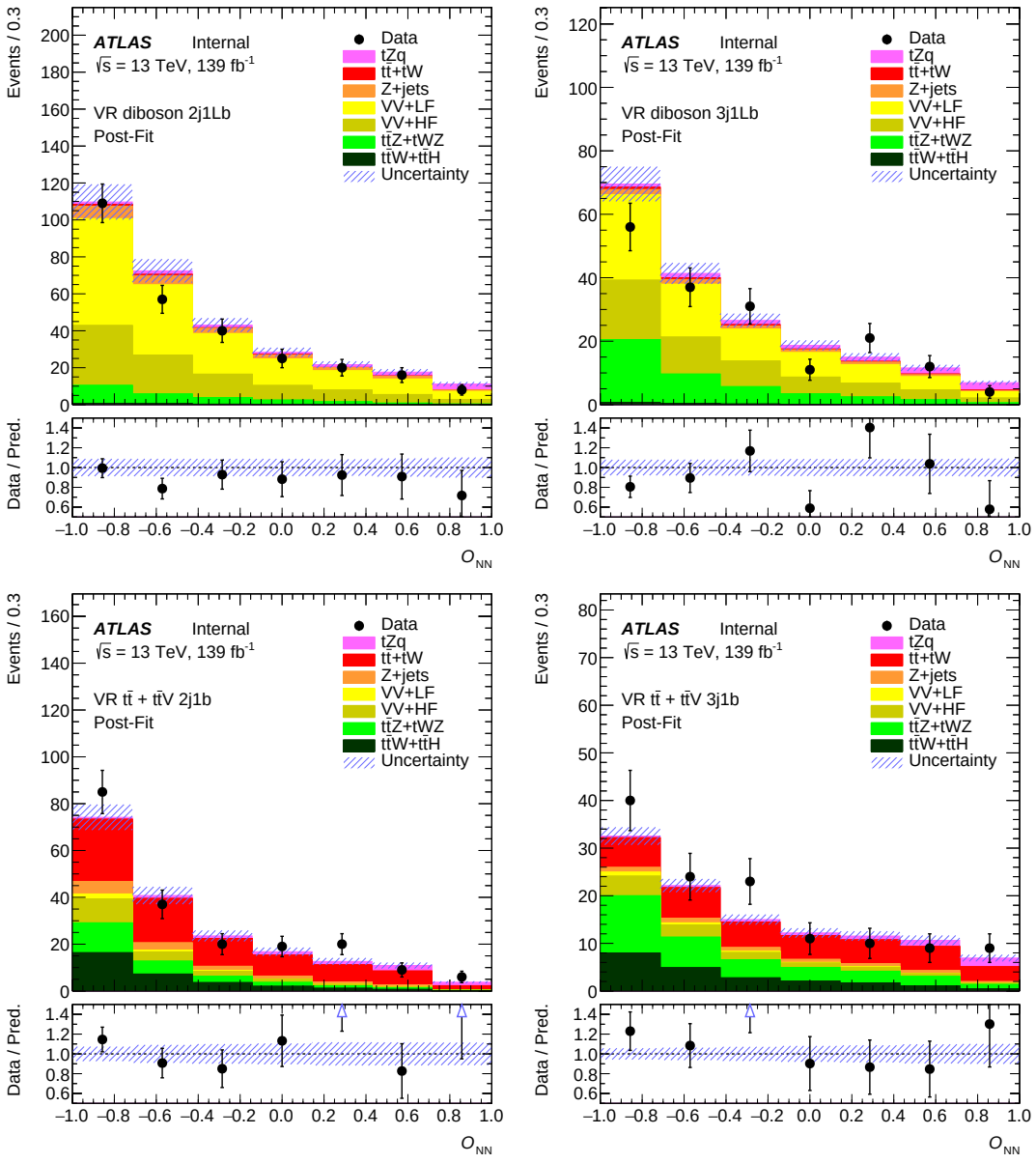


Figure 9.9: Analysis post-fit results of VR regions.

9.5 Interpretation of Results

Taking the fitted value of the tZq normalization scaled to the theoretical 5FS cross section prediction described in Section 4.3.1, the measured cross section using 139 fb^{-1} of pp collision data collected using the ATLAS detector is

$$\sigma(tl^+l^-q) \;=\; 97 \pm 13\ (\text{stat.}) \pm 7\ (\text{syst.})\,\text{fb}, \tag{9.3}$$

where the measured cross section includes contributions from non-resonant dilepton pairs with $m_{\ell\ell} > 30\,\text{GeV}$. This is in agreement with the SM prediction of 101.7 fb. The statistical significance of the measurement is estimated to be 9.1 σ, directly matching expectation.

Chapter 10

Conclusion

This thesis has presented the observation and measurement of the cross section of the $\mathrm{tZ}q$ process using data collected by the ATLAS detector in the years 2015 to 2018 using proton-proton collisions provided by the LHC. Only the trilepton decay channel is considered, and events containing three identified charged leptons (electrons and muons) two or three jets, one of which is identified as originating from a b-quark are selected. A series of Bayesian neural networks are used to improve the background rejection before extracting and measuring the signal using a binned maximum-likelihood estimator. The measured cross-section for $\mathrm{t}\ell^+\ell^- q$ production including non-resonant dilepton pairs with $m_{\ell\ell} > 30\,\mathrm{GeV}$ is $97 \pm 13\,(\mathrm{stat.}) \pm 7\,(\mathrm{syst.})\,\mathrm{fb}$. This is compatible with the standard model prediction of $101.7\,\mathrm{fb}\ ^{+5.2}_{-1.3}\%\,(\mathrm{scale})\ \pm 1.0\%\,(\mathrm{PDF})$. The statistical significance in favor of this processes' existence is estimated to be 9.1 σ. This directly matches the expected sensitivity of the analysis and surpasses the common benchmark 5 σ level of significance typically used to claim direct observation. The first public release of this result can be found in Ref. [142]. This is the most precise $\mathrm{tZ}q$ cross section measurement ever performed, and the second observation of such a process worldwide.

Perhaps most importantly, this signifies the observation of the $\mathrm{tZ}q$ process as a repeatable scientific endeavor, as it has been observed and measured by not only the ATLAS collaboration, but also by CMS [143]. In absence of the upending of

the last 25 to 50 years of particle physics, this unarguably verifies the existence of the $\mathrm{tZ}q$ interaction. The compatibility of this experimental observation with the prediction of the SM increases its reputation just a bit further as one of the most well tested theories in modern physics.

References

[1] Planck Collaboration, P. A. R. Ade et al., Astron. Astrophys. **571** (2014) A16, arXiv:1303.5076 [astro-ph.CO].

[2] G. Bertone, D. Hooper, and J. Silk, Phys. Rept. **405** (2005) 279–390, arXiv:hep-ph/0404175 [hep-ph].

[3] L. Canetti, M. Drewes, and M. Shaposhnikov, New J. Phys. **14** (2012) 095012, arXiv:1204.4186 [hep-ph].

[4] Muon g-2 Collaboration Collaboration, G. W. Bennett et al., Phys. Rev. D **73** (2006) 072003, https://link.aps.org/doi/10.1103/PhysRevD.73.072003.

[5] K. Hagiwara, R. Liao, A. D. Martin, D. Nomura, and T. Teubner, J. Phys. **G38** (2011) 085003, arXiv:1105.3149 [hep-ph].

[6] Particle Data Group Collaboration,, Phys. Rev. D **98** (2018) 030001, https://link.aps.org/doi/10.1103/PhysRevD.98.030001.

[7] S. L. Glashow, Nucl. Phys. **22** (1961) 579–588.

[8] S. Weinberg, Phys. Rev. Lett. **19** (1967) 1264–1266, https://link.aps.org/doi/10.1103/PhysRevLett.19.1264.

[9] A. Salam, Conf. Proc. **C680519** (1968) 367–377.

[10] M. Y. Han and Y. Nambu, Phys. Rev. **139** (1965) B1006–B1010, https://link.aps.org/doi/10.1103/PhysRev.139.B1006.

[11] P. W. Higgs, Phys. Lett. **12** (1964) 132–133.

[12] F. Englert and R. Brout, Phys. Rev. Lett. **13** (1964) 321–323, https://link.aps.org/doi/10.1103/PhysRevLett.13.321.

[13] ATLAS Collaboration, G. Aad et al., Phys. Lett. **B716** (2012) 1–29, arXiv:1207.7214 [hep-ex].

[14] CMS Collaboration, S. Chatrchyan et al., Phys. Lett. **B716** (2012) 30–61, arXiv:1207.7235 [hep-ex].

[15] V. D. Barger and R. J. N. Phillips, *Collider physics: 1993*, pp. , 0064–168. 1993. arXiv:hep-ph/9309250 [hep-ph].

[16] ATLAS Collaboration, Phys. Lett. B **716** (2012) 1, arXiv:1207.7214 [hep-ex].

[17] CMS Collaboration, Phys. Lett. B **716** (2012) 30, arXiv:1207.7235 [hep-ex].

[18] Y. Nambu, Phys. Rev. **117** (1960) 648–663, https://link.aps.org/doi/10.1103/PhysRev.117.648.

[19] J. Goldstone, A. Salam, and S. Weinberg, Phys. Rev. **127** (1962) 965–970, https://link.aps.org/doi/10.1103/PhysRev.127.965.

[20] N. Cabibbo, Phys. Rev. Lett. **10** (1963) 531–533, https://link.aps.org/doi/10.1103/PhysRevLett.10.531.

[21] M. Kobayashi and T. Maskawa, Progress of Theoretical Physics **49** (1973) 652–657, http://oup.prod.sis.lan/ptp/article-pdf/49/2/652/5257692/49-2-652.pdf, https://doi.org/10.1143/PTP.49.652.

[22] M. Gell-Mann, *The Eightfold Way: A Theory of strong interaction symmetry*, tech. rep., 1961.

[23] H. D. Politzer, Phys. Rev. Lett. **30** (1973) 1346–1349, https://link.aps.org/doi/10.1103/PhysRevLett.30.1346.

[24] D. J. Gross and F. Wilczek, Phys. Rev. Lett. **30** (1973) 1343–1346, https://link.aps.org/doi/10.1103/PhysRevLett.30.1343.

[25] R. Brandelik et al., Physics Letters B **86** (1979) 243–249, http://www.sciencedirect.com/science/article/pii/037026937990830X.

[26] The NNPDF collaboration, R. D. Ball, V. Bertone, S. Carrazza, C. S. Deans, L. Del Debbio, S. Forte, A. Guffanti, N. P. Hartland, J. I. Latorre, J. Rojo, and M. Ubiali, Journal of High Energy Physics **2015** (2015) 40, https://doi.org/10.1007/JHEP04(2015)040.

[27] G. Altarelli, Scholarpedia **4** (2009) 7124, revision #91681.

[28] K. Jakobs, https://cds.cern.ch/record/1459024, Comments: 53 pages, 42 figures, to be published in the proceedings of ESHEP 2011.

[29] M. E. Peskin and D. V. Schroeder, *An Introduction to quantum field theory*. Addison-Wesley, Reading, USA, 1995. http://www.slac.stanford.edu/~mpeskin/QFT.html.

[30] N. Kidonakis, Physical Review D **97** (2017) .

[31] R. H. Parker, C. Yu, W. Zhong, B. Estey, and H. Müller, Science **360** (2018) 191–195, https://science.sciencemag.org/content/360/6385/191.full.pdf, https://science.sciencemag.org/content/360/6385/191.

[32] The D0 Collaboration Collaboration,, Phys. Rev. Lett. **120** (2018) 241802, https://link.aps.org/doi/10.1103/PhysRevLett.120.241802.

[33] CDF, D0 Collaboration, T. A. Aaltonen et al., Phys. Rev. **D97** (2018) 112007, arXiv:1801.06283 [hep-ex].

[34] Particle Data Group Collaboration, K. A. Olive et al., Chin. Phys. **C38** (2014) 090001.

[35] J. Campbell, R. K. Ellis, and R. Röntsch, Phys. Rev. D **87** (2013) 114006, https://link.aps.org/doi/10.1103/PhysRevD.87.114006.

[36] ATLAS Collaboration Collaboration, O. Bessidskaia Bylund, *Measurement of ttZ and ttW production at ATLAS in 13 TeV data, using trilepton and same charge dimuon final states*, Tech. Rep. ATL-PHYS-PROC-2016-117, CERN, Geneva, Aug, 2016. https://cds.cern.ch/record/2211022.

[37] ATLAS Collaboration, M. Cristinziani, PoS **ICHEP2012** (2013) 217, arXiv:1302.3698 [hep-ex].

[38] C. Degrande, F. Maltoni, K. Mimasu, E. Vryonidou, and C. Zhang, Journal of High Energy Physics **2018** (2018) 5, https://doi.org/10.1007/JHEP10(2018)005.

[39] O. S. Brüning, P. Collier, P. Lebrun, S. Myers, R. Ostojic, J. Poole, and P. Proudlock, *LHC Design Report*. CERN Yellow Reports: Monographs. CERN, Geneva, 2004. https://cds.cern.ch/record/782076.

[40] ATLAS Collaboration, G. Aad et al., JINST **3** (2008) S08003.

[41] CMS Collaboration, L. Borrello, EPJ Web Conf. **164** (2017) 07023.

[42] LHCb Collaboration, A. A. Alves, Jr. et al., JINST **3** (2008) S08005.

[43] J. Schukraft, *The ALICE detector at the CERN LHC*, pp. , 398–415. 1996.

[44] A. Ster, *Linac 2 Performance optimization*, Tech. Rep. CERN-PS-97-005-HP, CERN, Geneva, Jan, 1997. https://cds.cern.ch/record/322715.

[45] S. van der Meer, *Calibration of the effective beam height in the ISR*, Tech. Rep. CERN-ISR-PO-68-31. ISR-PO-68-31, CERN, Geneva, 1968. https://cds.cern.ch/record/296752.

[46] G. Avoni, M. Bruschi, G. Cabras, D. Caforio, N. Dehghanian, A. Floderus, B. Giacobbe, F. Giannuzzi, F. Giorgi, P. Grafström, V. Hedberg, F. L. Manghi, S. Meneghini, J. Pinfold, E. Richards, C. Sbarra, N. S. Cesari, A. Sbrizzi, R. Soluk, G. Ucchielli, S. Valentinetti, O. Viazlo, M. Villa, C. Vittori, R. Vuillermet, and A. Zoccoli, Journal of Instrumentation **13** (2018) P07017–P07017, https://doi.org/10.1088%2F1748-0221%2F13%2F07%2Fp07017.

[47] ATLAS Collaboration Collaboration,, *Luminosity determination in pp collisions at $\sqrt{s} = 13$ TeV using the ATLAS detector at the LHC*, Tech. Rep. ATLAS-CONF-2019-021, CERN, Geneva, Jun, 2019. http://cds.cern.ch/record/2677054.

[48] ATLAS Collaboration, JINST **3** (2008) S08003.

[49] ATLAS Collaboration, G. Aad et al., Eur. Phys. J. **C70** (2010) 787–821, arXiv:1004.5293 [physics.ins-det].

[50] A. Collaboration, *Technical Design Report for the ATLAS Inner Tracker Strip Detector*, Tech. Rep. CERN-LHCC-2017-005. ATLAS-TDR-025, CERN, Geneva, Apr, 2017. https://cds.cern.ch/record/2257755.

[51] ATLAS Collaboration, Atlas-tdr-19, 2010, https://cds.cern.ch/record/1291633.

[52] B. Abbott et al., JINST **13** (2018) T05008, arXiv:1803.00844 [physics.ins-det].

[53] J. Metcalfe, *Development of Planar and 3D Silicon Sensor Technologies for the ATLAS Experiment Upgrades and Measurements of Heavy Quark Production Fractions with Fully Reconstructed D-star Mesons with ATLAS*, Dec, 2011. https://cds.cern.ch/record/1447153. Presented 09 Dec 2011.

[54] Journal of Instrumentation **3** (2008) S08003–S08003, https://doi.org/10.1088%2F1748-0221%2F3%2F08%2Fs08003.

[55] ATLAS Collaboration, JINST **12** (2017) P05002, arXiv:1702.06473 [hep-ex].

[56] Journal of Instrumentation **12** (2017) P05002–P05002, https://doi.org/10.1088%2F1748-0221%2F12%2F05%2Fp05002.

[57] A. Vogel, *ATLAS Transition Radiation Tracker (TRT): Straw Tube Gaseous Detectors at High Rates*, Tech. Rep. ATL-INDET-PROC-2013-005, CERN, Geneva, Apr, 2013. https://cds.cern.ch/record/1537991.

[58] ATLAS Collaboration, ATL-PHYS-PUB-2016-015, 2016, https://cds.cern.ch/record/2203514.

[59] A. Collaboration, *Technical Design Report for the Phase-II Upgrade of the ATLAS LAr Calorimeter*, Tech. Rep. CERN-LHCC-2017-018. ATLAS-TDR-027, CERN, Geneva, Sep, 2017. https://cds.cern.ch/record/2285582.

[60] ATLAS Collaboration, N. Nikiforou, *Performance of the ATLAS Liquid Argon Calorimeter after three years of LHC operation and plans for a future upgrade*, in *Proceedings, 3rd International Conference on Advancements in Nuclear Instrumentation Measurement Methods and their Applications (ANIMMA 2013): Marseille, France, June 23-27, 2013*. 2013. arXiv:1306.6756 [physics.ins-det].

[61] ATLAS Collaboration, P. Bartos, PoS **LHCP2016** (2016) 204.

[62] ATLAS Collaboration Collaboration,, *ATLAS tile calorimeter: Technical Design Report*. Technical Design Report ATLAS. CERN, Geneva, 1996. https://cds.cern.ch/record/331062.

[63] S. Psoroulas, *Measurement of the jet energy resolution in ATLAS*, 2011. http://cdsweb.cern.ch/record/1389896/files/ATL-PHYS-PROC-2011-156.pdf.

[64] ATLAS Collaboration Collaboration,, *ATLAS magnet system: Technical Design Report, 1*. Technical Design Report ATLAS. CERN, Geneva, 1997. https://cds.cern.ch/record/338080.

[65] ATLAS Collaboration, K. Ishii, PoS **HEP2001** (2001) 253.

[66] ATLAS Collaboration Collaboration,, *ATLAS muon spectrometer: Technical Design Report*. Technical Design Report ATLAS. CERN, Geneva, 1997. https://cds.cern.ch/record/331068.

[67] Salvucci, Antonio, EPJ Web of Conferences **28** (2012) 12039, https://doi.org/10.1051/epjconf/20122812039.

[68] G. Artoni, Nuclear and Particle Physics Proceedings **273-275** (2016) 2542 – 2544, http://www.sciencedirect.com/science/article/pii/S2405601415009426, 37th International Conference on High Energy Physics (ICHEP).

[69] ATLAS Collaboration, Eur. Phys. J. C **77** (2017) 317, arXiv:1611.09661 [hep-ex].

[70] *TopCommonObjects13TeV*, https://twiki.cern.ch/twiki/bin/view/AtlasProtected/TopCommonObjects13TeV.

[71] *AnalysisTop*, https://twiki.cern.ch/twiki/bin/viewauth/AtlasProtected/AnalysisTop.

[72] ATLAS Collaboration, ATL-PHYS-PUB-2015-041, 2015, https://cds.cern.ch/record/2048202.

[73] ATLAS Collaboration, ATLAS-CONF-2016-024, 2016, https://cds.cern.ch/record/2157687.

[74] ATLAS Collaboration, ATL-PHYS-PUB-2015-037, 2015, https://cds.cern.ch/record/2047831.

[75] W. Lampl et al., ATL-LARG-PUB-2008-002, 2008, https://cds.cern.ch/record/1099735.

[76] ATLAS Collaboration, Eur. Phys. J. C **77** (2017) 580, arXiv:1705.02211 [hep-ex].

[77] ATLAS Collaboration, T. A. collaboration.

[78] *D0 Collaboration*, http://www-d0.fnal.gov/Run2Physics/top/singletop_observation/singletop_observation_updated.html.

[79] ATLAS Collaboration, ATL-PHYS-PUB-2016-012, 2016, https://cds.cern.ch/record/2160731.

[80] ATLAS Collaboration, ATLAS-CONF-2011-102, 2011, https://cds.cern.ch/record/1369219.

[81] J. Ferrando, J. Geisen, C. S. Pollard, M. Saimpert, and J. C. Schmoeckel, *Measurement of the b-jet identification efficiency with $t\bar{t}$ events using an improved likelihood method: Calibration INT note of ANA-FTAG-2018-01*, Tech. Rep. ATL-COM-PHYS-2018-1072, CERN, Geneva, 06, 2018. https://cds.cern.ch/record/2631547.

[82] ATLAS Collaboration, Eur. Phys. J. C **72** (2012) 1844, arXiv:1108.5602 [hep-ex].

[83] ATLAS Collaboration, arXiv:1609.09324 [hep-ex].

[84] ATLAS Collaboration, ATL-PHYS-PUB-2015-027, 2015, https://cds.cern.ch/record/2037904.

[85] ATLAS Collaboration, ATL-DAQ-PUB-2016-001, 2016, https://cds.cern.ch/record/2136007/.

[86] ATLAS Collaboration, ATL-DAQ-PUB-2017-001, 2017, https://cds.cern.ch/record/2242069.

[87] S. Alioli et al., arXiv:1902.01674 [hep-ph].

[88] GEANT4 Collaboration, S. Agostinelli et al., Nucl. Instrum. Meth. A **506** (2003) 250–303.

[89] ATLAS Collaboration, Z. Marshall, J. Phys. Conf. Ser. **513** (2014) 022024.

[90] J. Alwall, R. Frederix, S. Frixione, V. Hirschi, F. Maltoni, O. Mattelaer, H. S. Shao, T. Stelzer, P. Torrielli, and M. Zaro, JHEP **07** (2014) 079, arXiv:1405.0301 [hep-ph].

[91] NNPDF Collaboration, NNPDF Collaboration, R.D. Ball et al., JHEP **04** (2015) 040, arXiv:1410.8849 [hep-ph].

[92] T. Sjöstrand, S. Ask, J. R. Christiansen, R. Corke, N. Desai, P. Ilten, S. Mrenna, S. Prestel, C. O. Rasmussen, and P. Z. Skands, Comput. Phys. Commun. **191** (2015) 159–177, arXiv:1410.3012 [hep-ph].

[93] ATLAS Collaboration, Atl-phys-pub-2014-021, https://cds.cern.ch/record/1966419.

[94] S. Frixione, E. Laenen, P. Motylinski, and B. R. Webber, JHEP **0704** (2007) 081, arXiv:hep-ph/0702198.

[95] P. Artoisenet, R. Frederix, O. Mattelaer, and R. Rietkerk, JHEP **1303** (2013) 015, arXiv:1212.3460 [hep-ph].

[96] R. Frederix, E. Re, and P. Torrielli, JHEP **09** (2012) 130, arXiv:1207.5391 [hep-ph].

[97] D. J. Lange, Nucl. Instrum. Meth. A **462** (2001) 152.

[98] https://indico.cern.ch/event/708573/contributions/2995420/attachments/1649998/2638496/VryonidoutZjsm.pdf.

[99] S. Frixione et al., JHEP **09** (2007) 126, arXiv:0707.3088 [hep-ph].

[100] P. Nason, JHEP **0411** (2004) 040, arXiv:hep-ph/0409146.

[101] S. Frixione, P. Nason, and C. Oleari, JHEP **11** (2007) 070, arXiv:0709.2092 [hep-ph].

[102] S. Alioli, P. Nason, C. Oleari, and E. Re, JHEP **06** (2010) 043, arXiv:1002.2581 [hep-ph].

[103] ATLAS Collaboration, ATL-PHYS-PUB-2016-020, 2016, https://cds.cern.ch/record/2216168.

[104] ATLAS Collaboration, ATL-PHYS-PUB-2017-007, 2017, https://cds.cern.ch/record/2261938.

[105] M. Bahr et al., Eur. Phys. J. C **58** (2008) 639–707, arXiv:0803.0883 [hep-ph].

[106] J. Bellm et al., Eur. Phys. J. C **76** (2016) 196, arXiv:1512.01178 [hep-ph].

[107] L. Harland-Lang, A. Martin, P. Motylinski, and R. Thorne, Eur. Phys. J. C **75** (2015) 204, arXiv:1412.3989 [hep-ph].

[108] S. Frixione, E. Laenen, P. Motylinski, B. R. Webber, and C. D. White, JHEP **0807** (2008) 029, arXiv:0805.3067 [hep-ph].

[109] T. Gleisberg et al., JHEP **02** (2009) 007, arXiv:0811.4622 [hep-ph].

[110] T. Gleisberg and S. Höche, JHEP **12** (2008) 039, arXiv:0808.3674 [hep-ph].

[111] S. Schumann and F. Krauss, JHEP **03** (2008) 038, arXiv:0709.1027 [hep-ph].

[112] S. Höche, F. Krauss, M. Schonherr, and F. Siegert, JHEP **09** (2012) 049, arXiv:1111.1220 [hep-ph].

[113] S. Höche, F. Krauss, M. Schönherr, and F. Siegert, JHEP **04** (2013) 027, arXiv:1207.5030 [hep-ph].

[114] S. Catani, F. Krauss, R. Kuhn, and B. R. Webber, JHEP **11** (2001) 063, arXiv:hep-ph/0109231.

[115] S. Höche, F. Krauss, S. Schumann, and F. Siegert, JHEP **05** (2009) 053, arXiv:0903.1219 [hep-ph].

[116] F. Cascioli, P. Maierhofer, and S. Pozzorini, Phys. Rev. Lett. **108** (2012) 111601, arXiv:1111.5206 [hep-ph].

[117] A. Denner, S. Dittmaier, and L. Hofer, Comput. Phys. Commun. **212** (2017) 220–238, arXiv:1604.06792 [hep-ph].

[118] M. e. a. Aaboud, The European Physical Journal C **79** (2019) 535, https://doi.org/10.1140/epjc/s10052-019-7027-6.

[119] G. E. Hinton and R. M. Neal, *Bayesian learning for neural networks*, 1995.

[120] M. Feindt, 2004, arXiv:0402093v1.

[121] M. Feindt and U. Kerzel, Nucl. Instrum. Meth. **A559** (2006) 190–194.

[122] M. e. a. Aaboud, The European Physical Journal C **77** (2017) 195, https://doi.org/10.1140/epjc/s10052-017-4756-2.

[123] ATLAS Collaboration, Eur. Phys. J. C **74** (2014) 3071, arXiv:1407.5063 [hep-ex].

[124] *JetPubPlots*, https://atlas.web.cern.ch/Atlas/GROUPS/PHYSICS/PLOTS/JETM-2018-006.

[125] ATLAS Collaboration, arXiv:1703.09665 [hep-ex].

[126] The ATLAS Collaboration, The European Physical Journal C **73** (2013) 2306, https://doi.org/10.1140/epjc/s10052-013-2306-0.

[127] ATLAS Collaboration, ATLAS-CONF-2014-046, 2014, https://cds.cern.ch/record/1741020.

[128] ATLAS Collaboration, ATLAS-CONF-2014-004, 2014, https://cds.cern.ch/record/1664335.

[129] J. M. Campbell, J. Huston, and W. Stirling, Rept. Prog. Phys. **70** (2007) 89, arXiv:hep-ph/0611148.

[130] J. Butterworth et al., J. Phys. G **43** (2016) 023001, arXiv:1510.03865 [hep-ph].

[131] D. de Florian et al., arXiv:1610.07922 [hep-ph].

[132] ATLAS Collaboration, arXiv:1902.05759 [hep-ex].

[133] ATLAS Collaboration, JHEP **12** (2017) 024, arXiv:1708.03299 [hep-ex].

[134] ATLAS Collaboration, arXiv:1608.03953 [hep-ex].

[135] John Wiley and Sons, Ltd, 2013. https://onlinelibrary.wiley.com/doi/abs/10.1002/9783527653416.fmatter.

[136] *TRExFitter*, https://twiki.cern.ch/twiki/bin/viewauth/AtlasProtected/TtHFitter.

[137] W. Verkerke and D. P. Kirkby, eConf **C0303241** (2003) MOLT007, arXiv:physics/0306116 [physics], [,186(2003)].

[138] L. Moneta, K. Belasco, K. S. Cranmer, S. Kreiss, A. Lazzaro, D. Piparo, G. Schott, W. Verkerke, and M. Wolf, PoS **ACAT2010** (2010) 057, arXiv:1009.1003 [physics.data-an].

[139] G. Cowan, K. Cranmer, E. Gross, and O. Vitells, Eur. Phys. J. **C71** (2011) 1554, arXiv:1007.1727 [physics.data-an], [Erratum: Eur. Phys. J.C73,2501(2013)].

[140] K. Cranmer, G. Lewis, L. Moneta, A. Shibata, and W. Verkerke, Cern-open-2012-016, http://cds.cern.ch/record/1456844.

[141] L. Lista, CERN Yellow Reports: School Proceedings **5** (2017) 213, https://e-publishing.cern.ch/index.php/CYRSP/article/view/354.

[142] ATLAS Collaboration Collaboration,, *Observation of the associated production of a top quark and a Z boson in pp collisions at* $\sqrt{s} = 13$ *TeV with the ATLAS detector*, Tech. Rep. ATLAS-CONF-2019-043, CERN, Geneva, Sep, 2019. https://cds.cern.ch/record/2690716.

[143] CMS Collaboration Collaboration, e. a. Sirunyan, A. M., Phys. Rev. Lett. **122** (2019) 132003, https://link.aps.org/doi/10.1103/PhysRevLett.122.132003.

Appendix A

Signal Region Plots

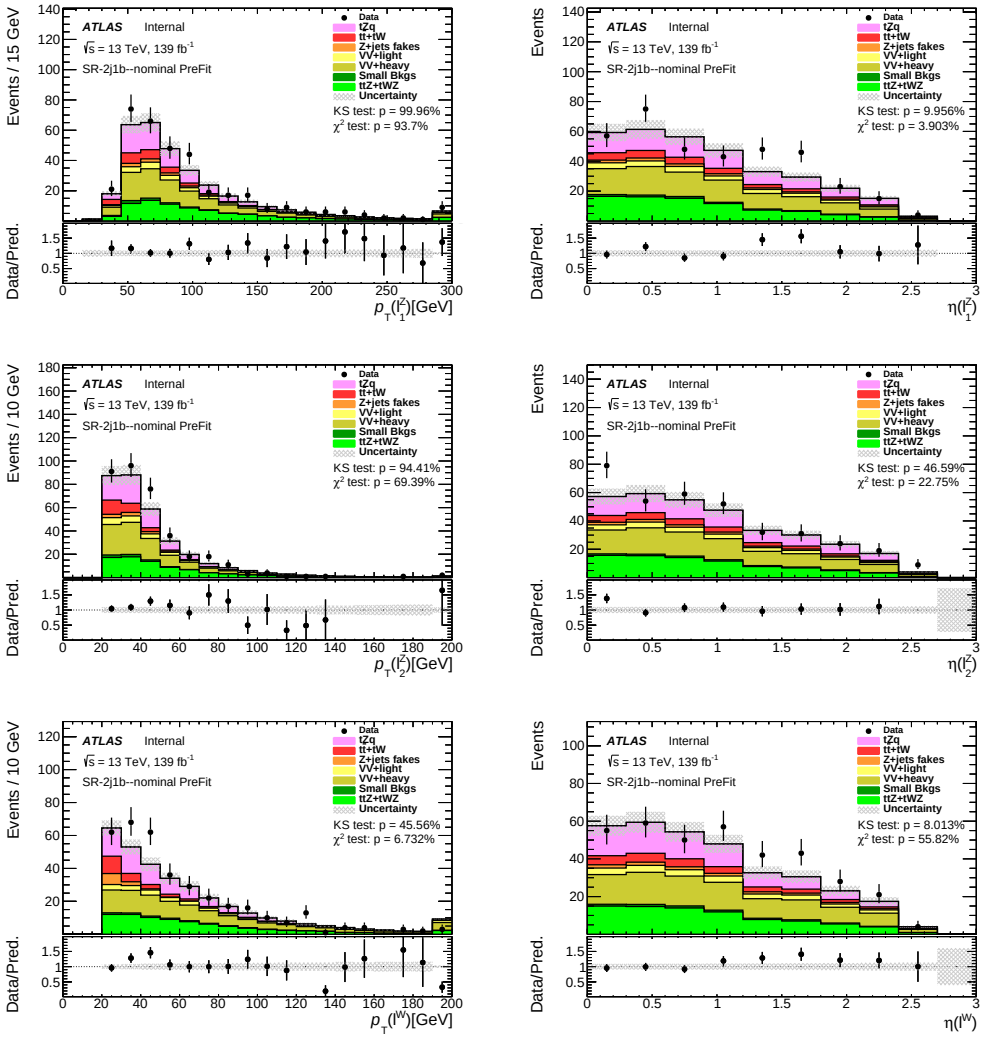


Figure A.1: Comparison of data and predictions for reconstructed lepton-related quantities for events in the 2j1b SR. The uncertainty shown is the backgrounds' modeling uncertainty.

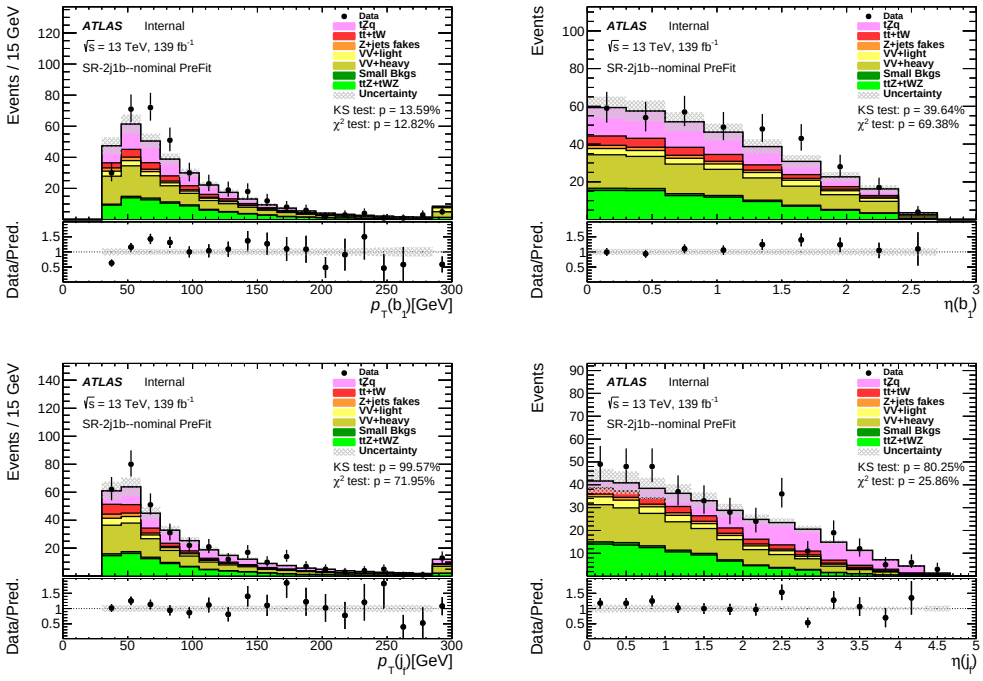


Figure A.2: Comparison of data and predictions for reconstructed jet-related quantities for events in the 2j1b SR.The uncertainty shown is the backgrounds' modeling uncertainty.

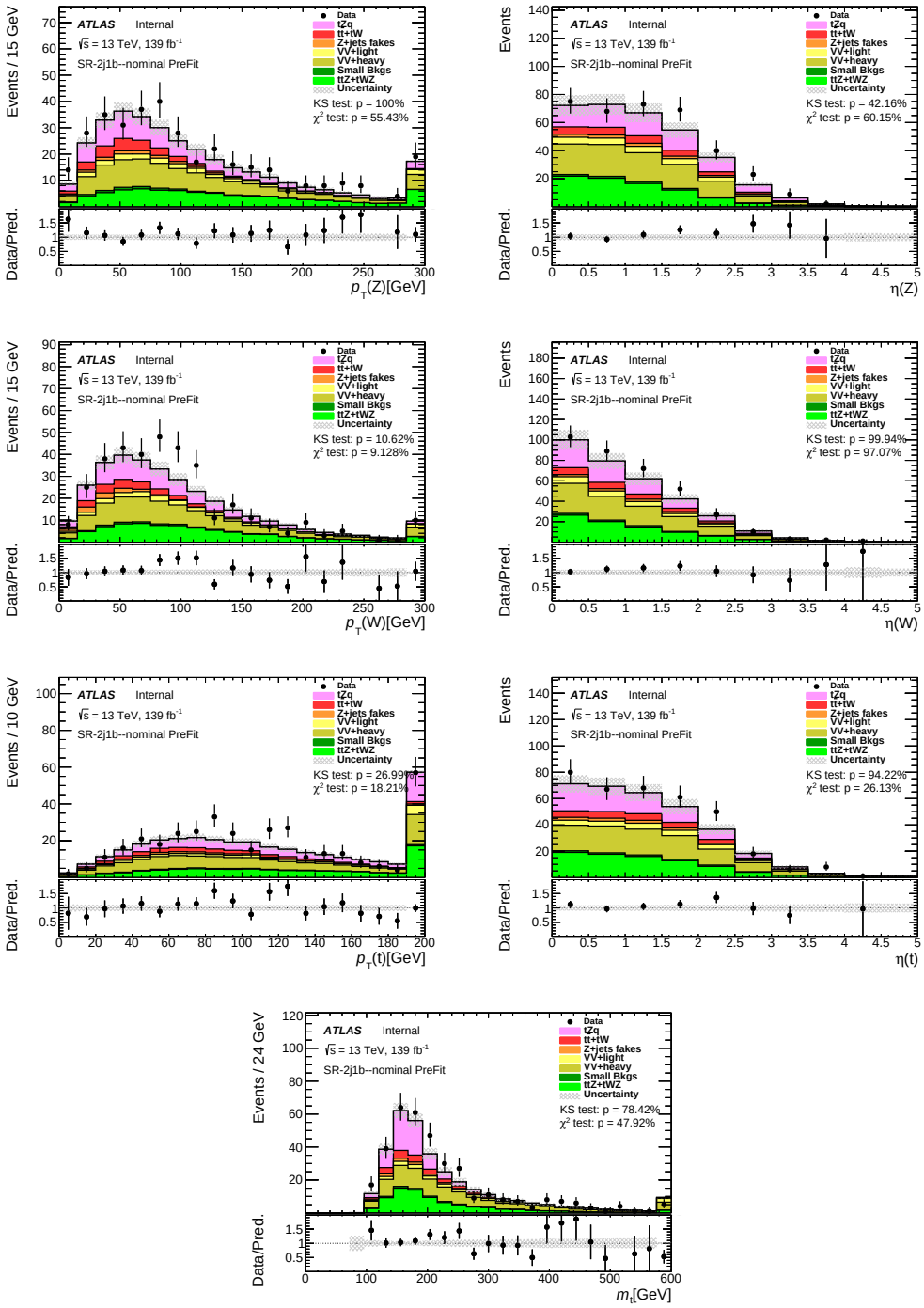


Figure A.3: Comparison of data and predictions for reconstructed event-related quantities for events in the 2j1b SR. The uncertainty shown is the backgrounds' modeling uncertainty.

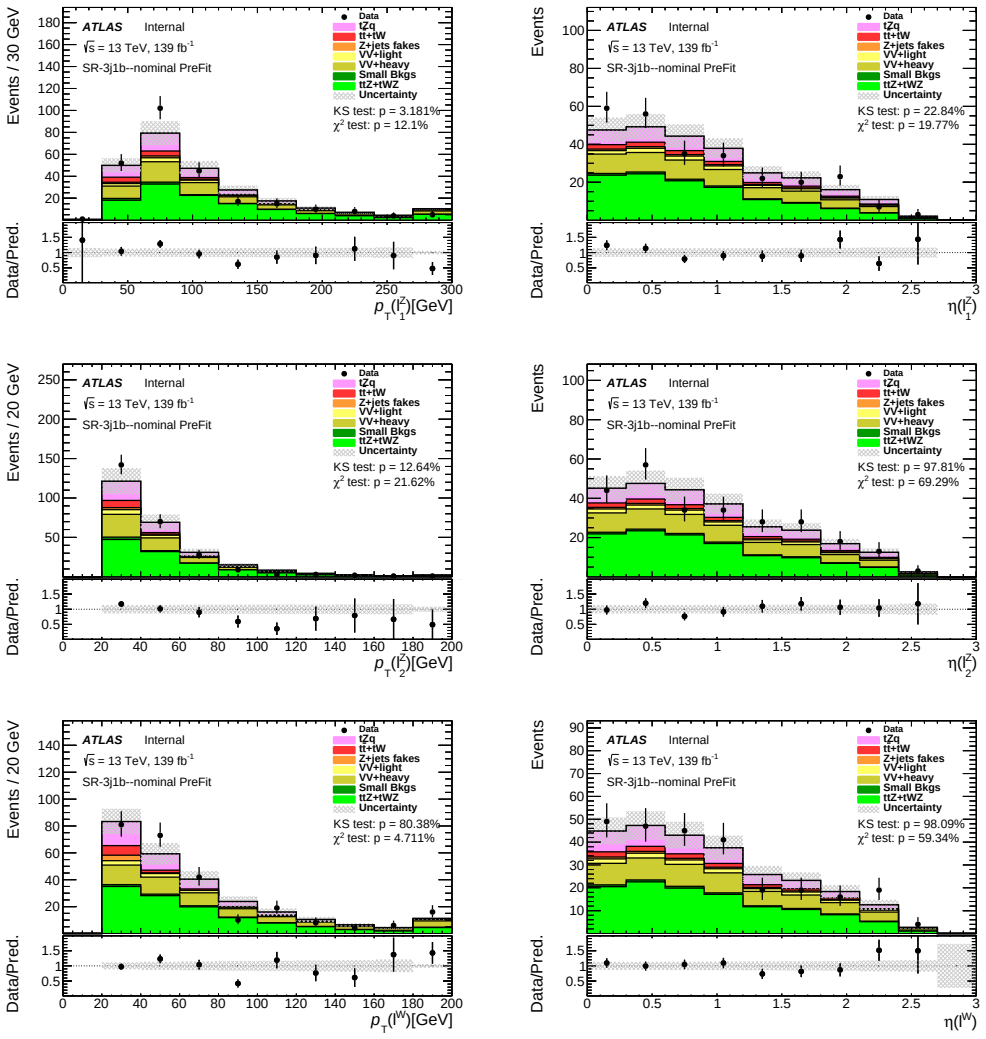


Figure A.4: Comparison of data and predictions for reconstructed lepton-related quantities for events in the 3j1b SR. The uncertainty shown is the backgrounds' modeling uncertainty.

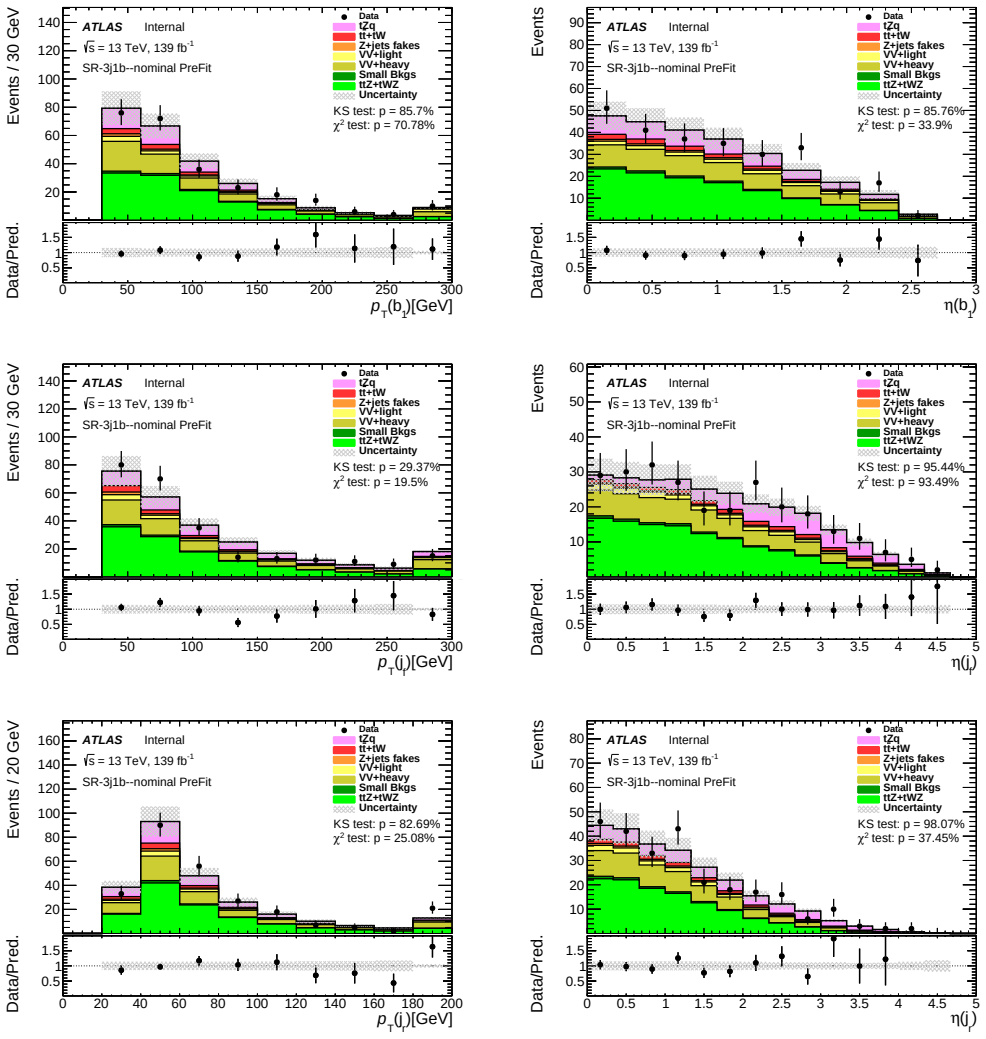


Figure A.5: Comparison of data and predictions for reconstructed jet-related quantities for events in the 3j1b SR. The uncertainty shown is the backgrounds' modeling uncertainty.

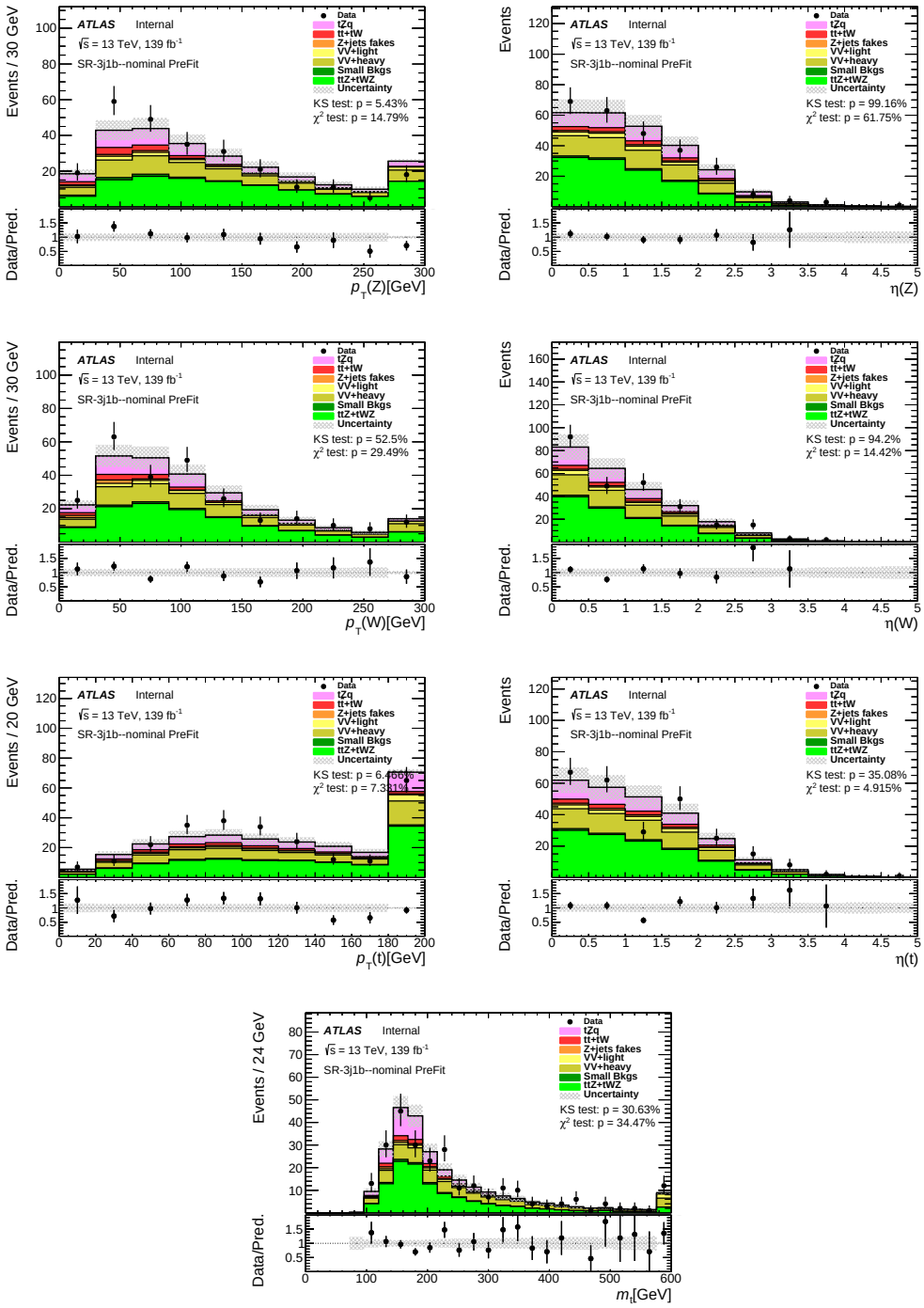


Figure A.6: Comparison of data and predictions for reconstructed event-related quantities for events in the 3j1b SR. The uncertainty shown is the backgrounds' modeling uncertainty.

Appendix B

$t\bar{t}$ Validation Regions Plots

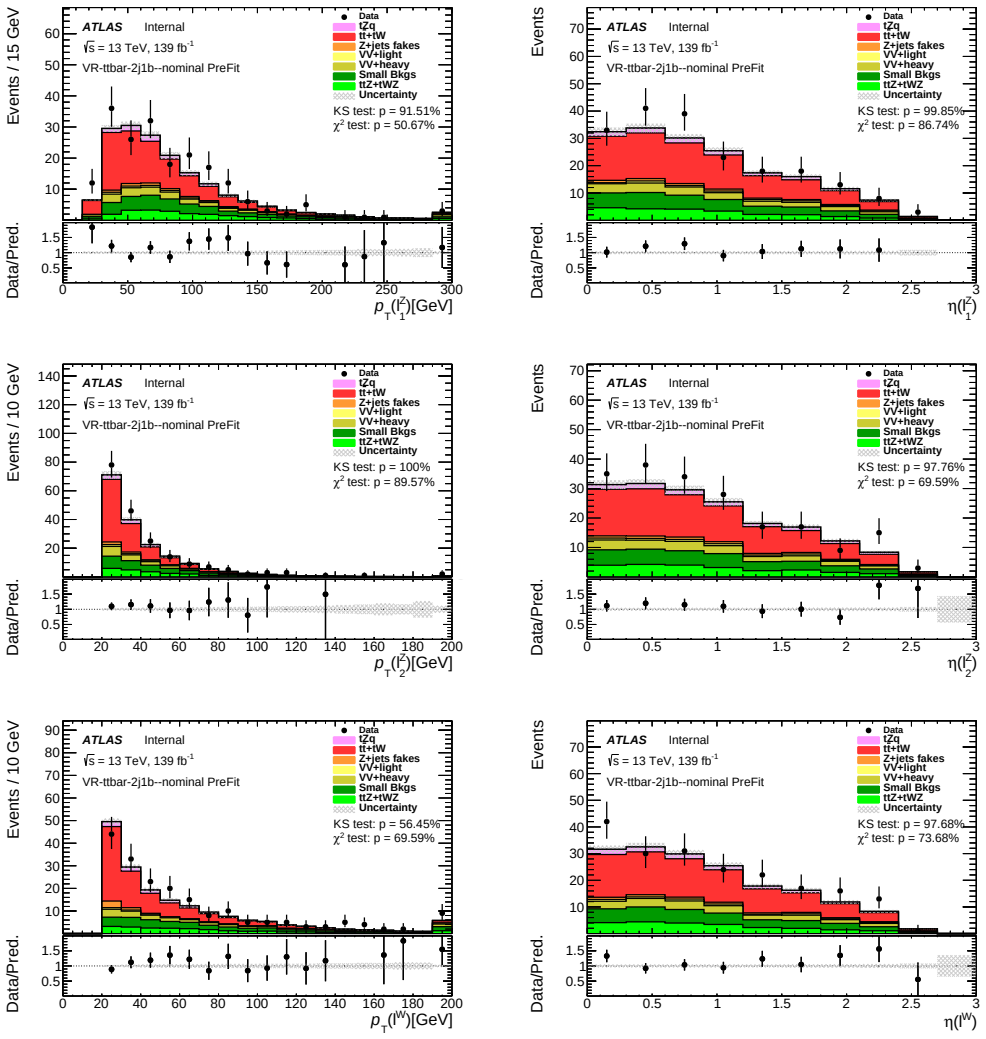


Figure B.1: Comparison of data and predictions for reconstructed lepton-related quantities for events in the 2j1b VR-ttbar. The uncertainty shown is the backgrounds' modeling uncertainty.

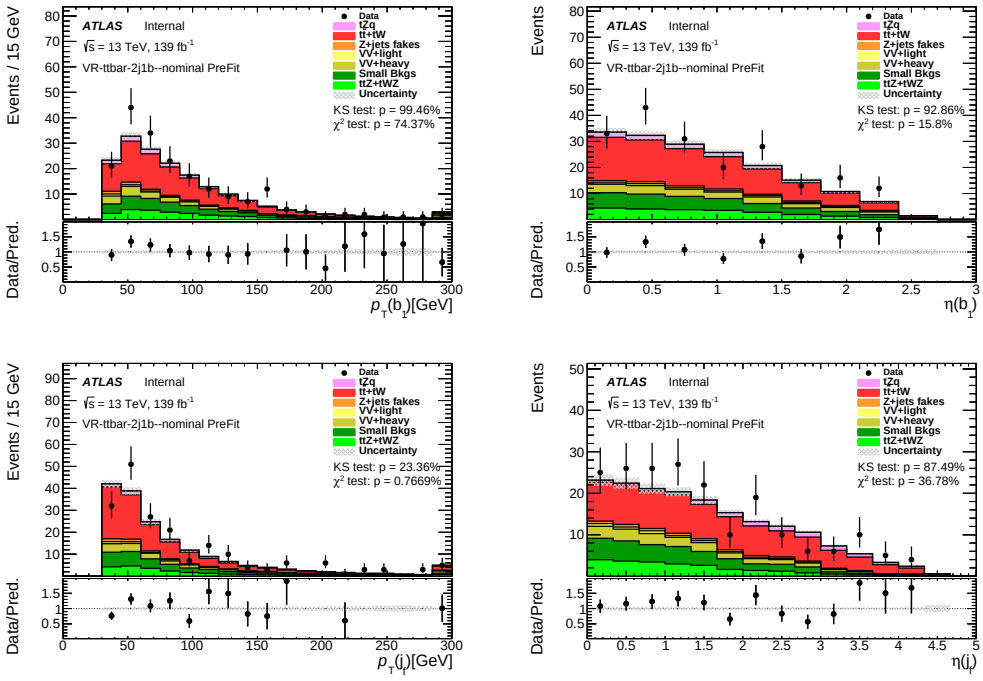


Figure B.2: Comparison of data and predictions for reconstructed jet-related quantities for events in the 2j1b VR-ttbar.The uncertainty shown is the backgrounds' modeling uncertainty.

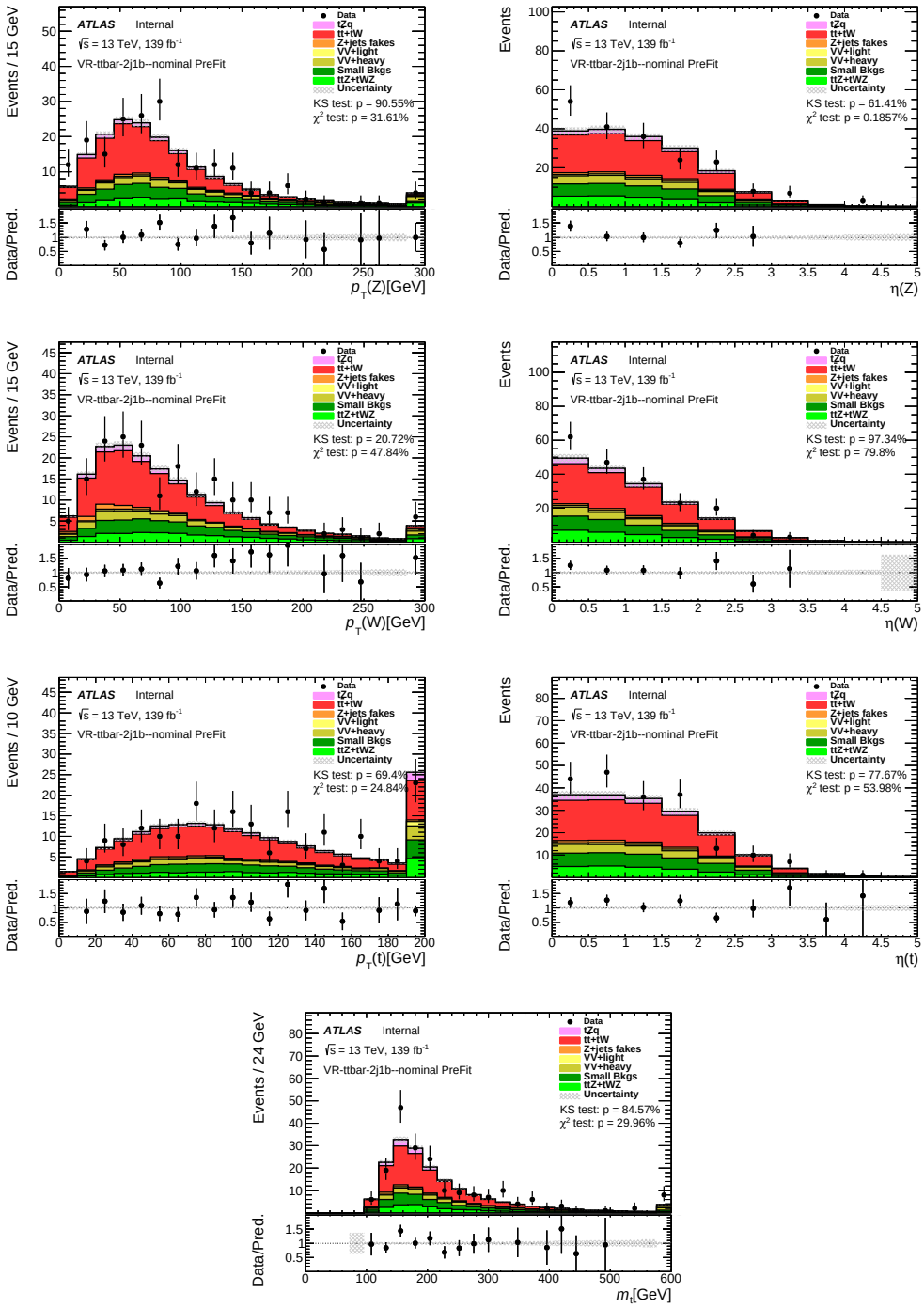


Figure B.3: Comparison of data and predictions for reconstructed event-related quantities for events in the 2j1b VR-ttbar. The uncertainty shown is the backgrounds' modeling uncertainty.

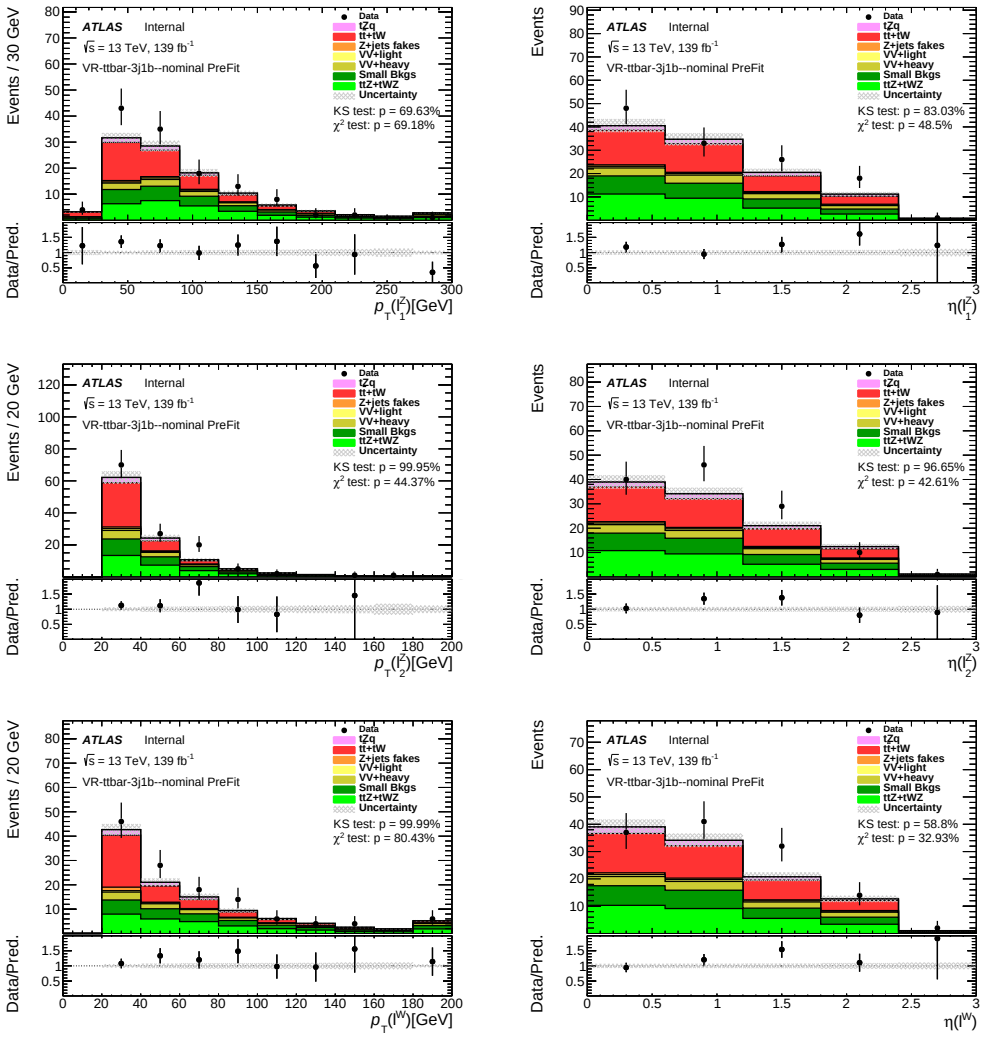


Figure B.4: Comparison of data and predictions for reconstructed lepton-related quantities for events in the 3j1b VR-ttbar. The uncertainty shown is the backgrounds' modeling uncertainty.

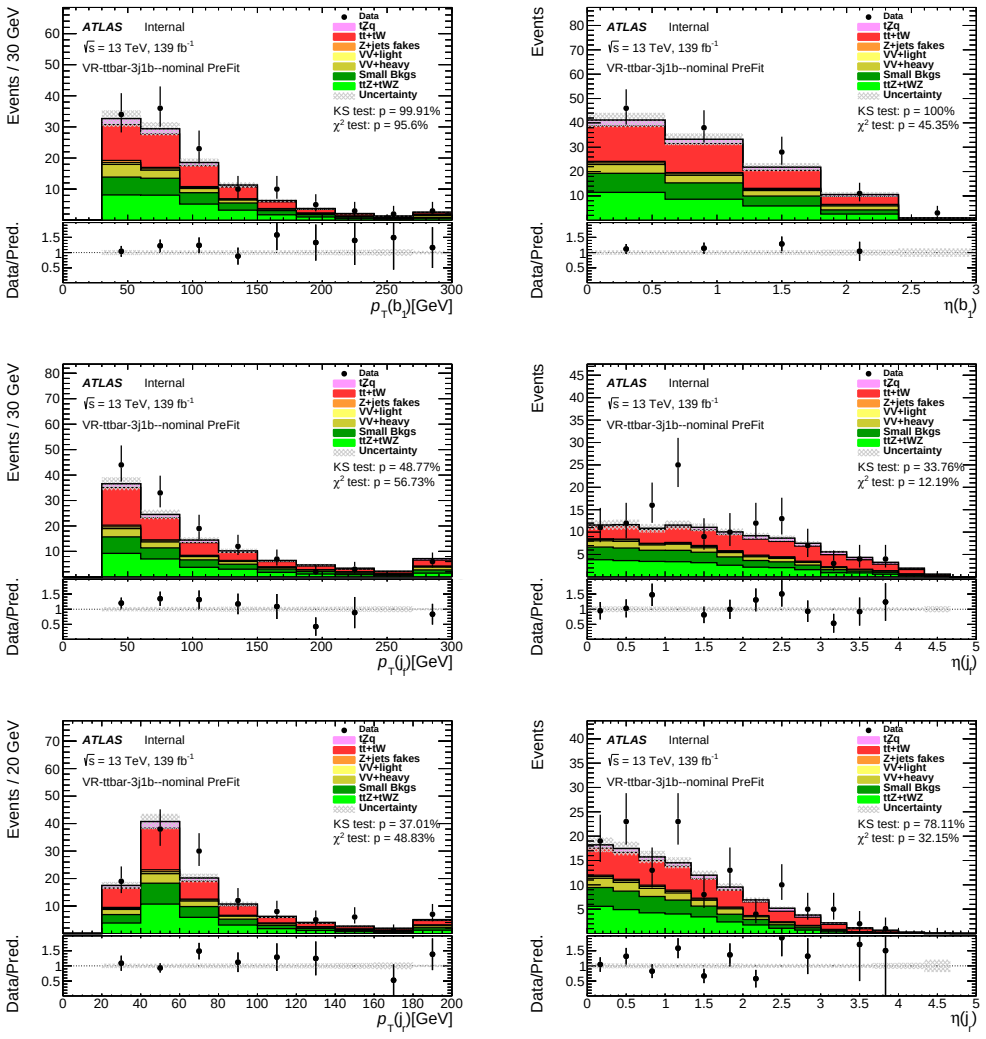


Figure B.5: Comparison of data and predictions for reconstructed jet-related quantities for events in the 3j1b VR-ttbar. The uncertainty shown is the backgrounds' modeling uncertainty.

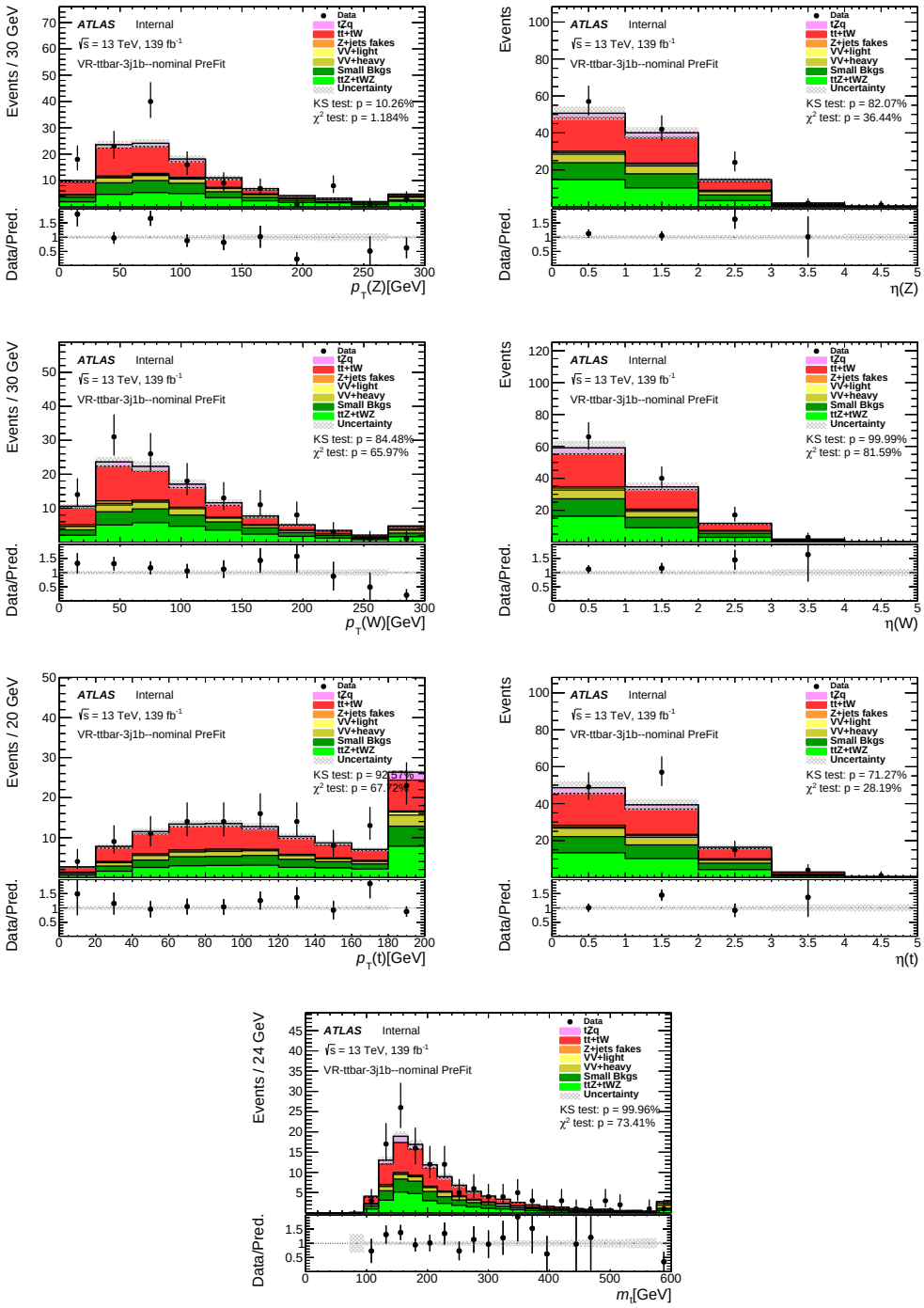


Figure B.6: Comparison of data and predictions for reconstructed event-related quantities for events in the 3j1b VR-ttbar. The uncertainty shown is the backgrounds' modeling uncertainty.

Appendix C

Diboson Validation Regions Plots

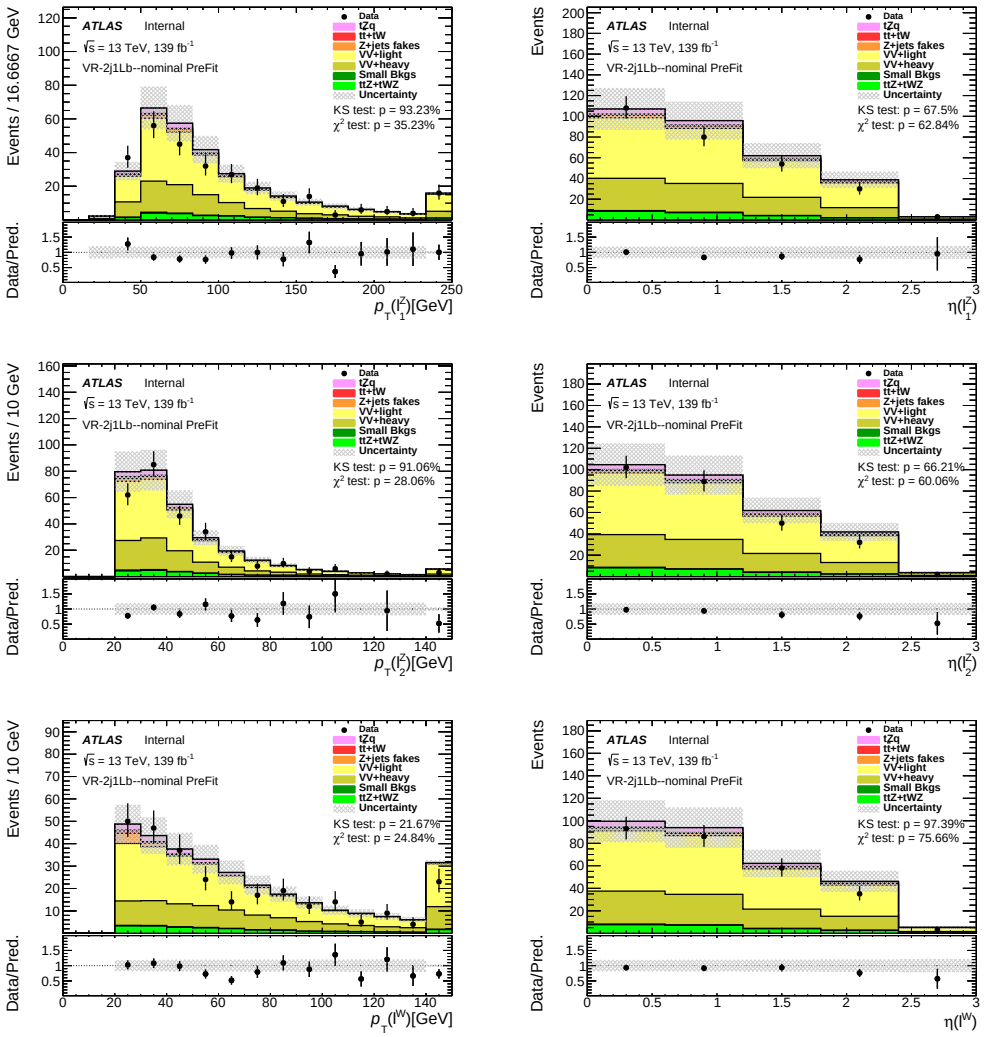


Figure C.1: Comparison of data and predictions for reconstructed lepton-related quantities for events in the 2j1Lb VR. The uncertainty shown is the backgrounds' modeling uncertainty.

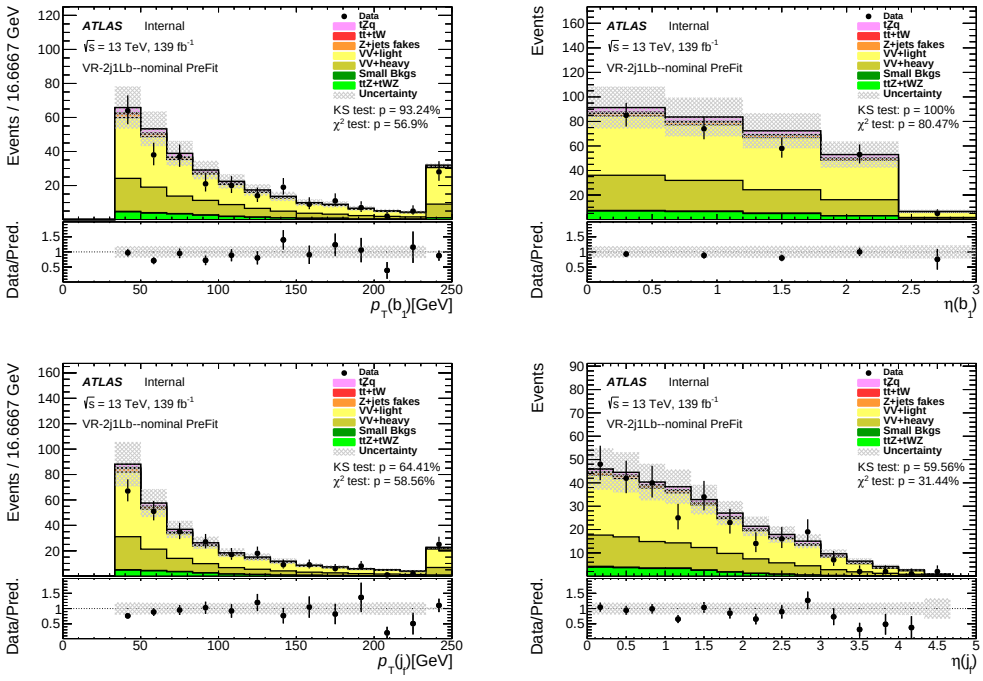


Figure C.2: Comparison of data and predictions for reconstructed jet-related quantities for events in the 2j1Lb VR.The uncertainty shown is the backgrounds' modeling uncertainty.

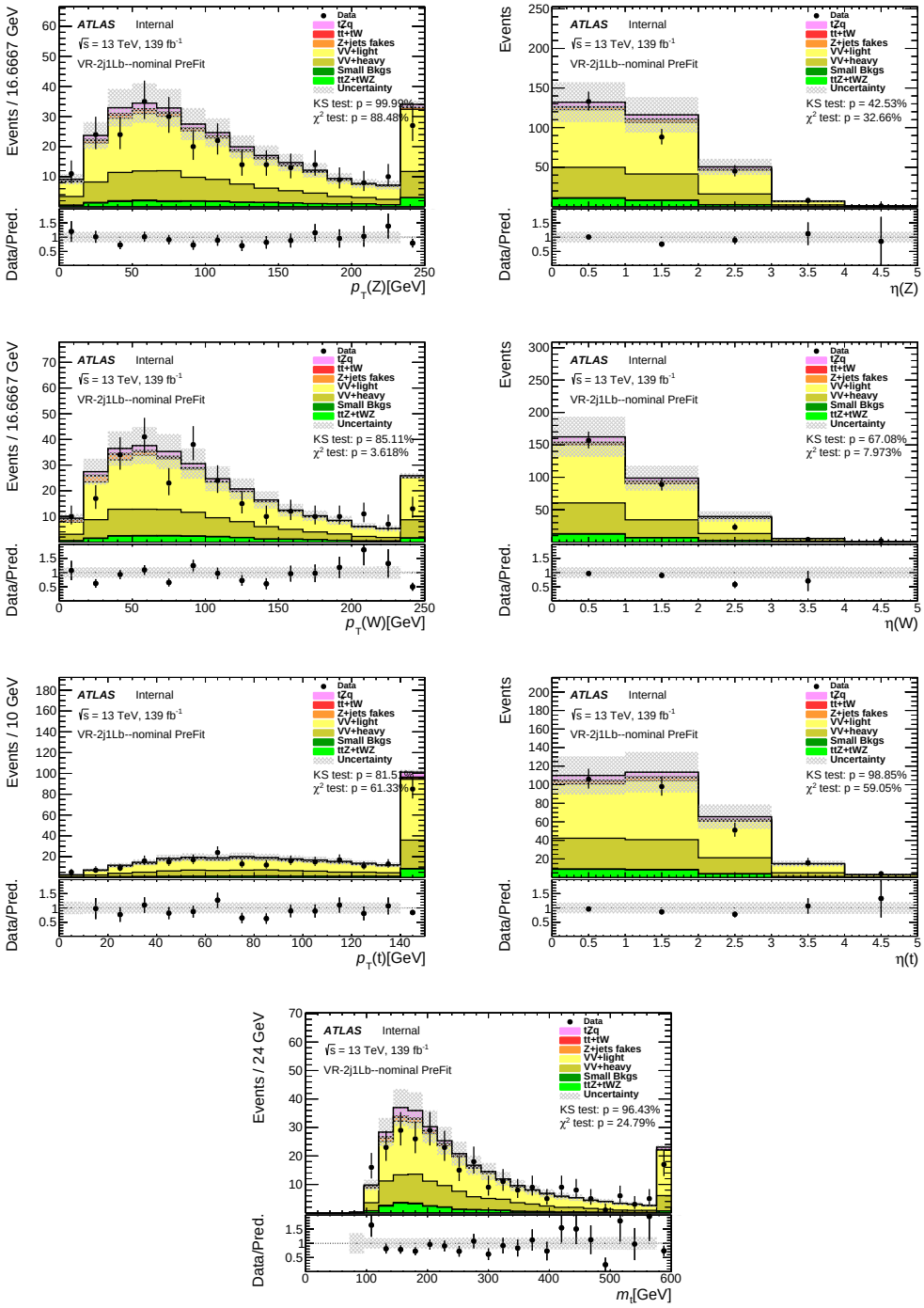


Figure C.3: Comparison of data and predictions for reconstructed event-related quantities for events in the 2j1Lb VR. The uncertainty shown is the backgrounds' modeling uncertainty.

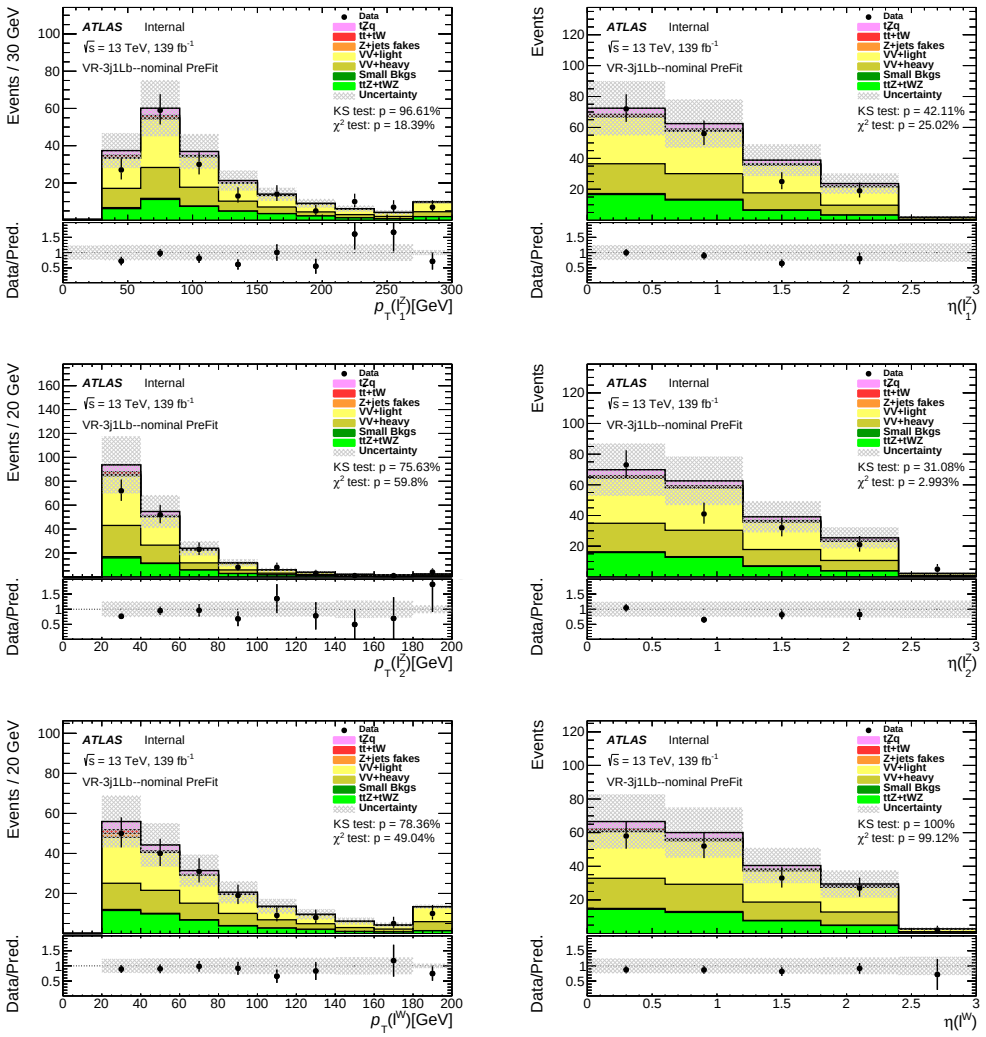


Figure C.4: Comparison of data and predictions for reconstructed lepton-related quantities for events in the 3j1Lb VR. The uncertainty shown is the backgrounds' modeling uncertainty.

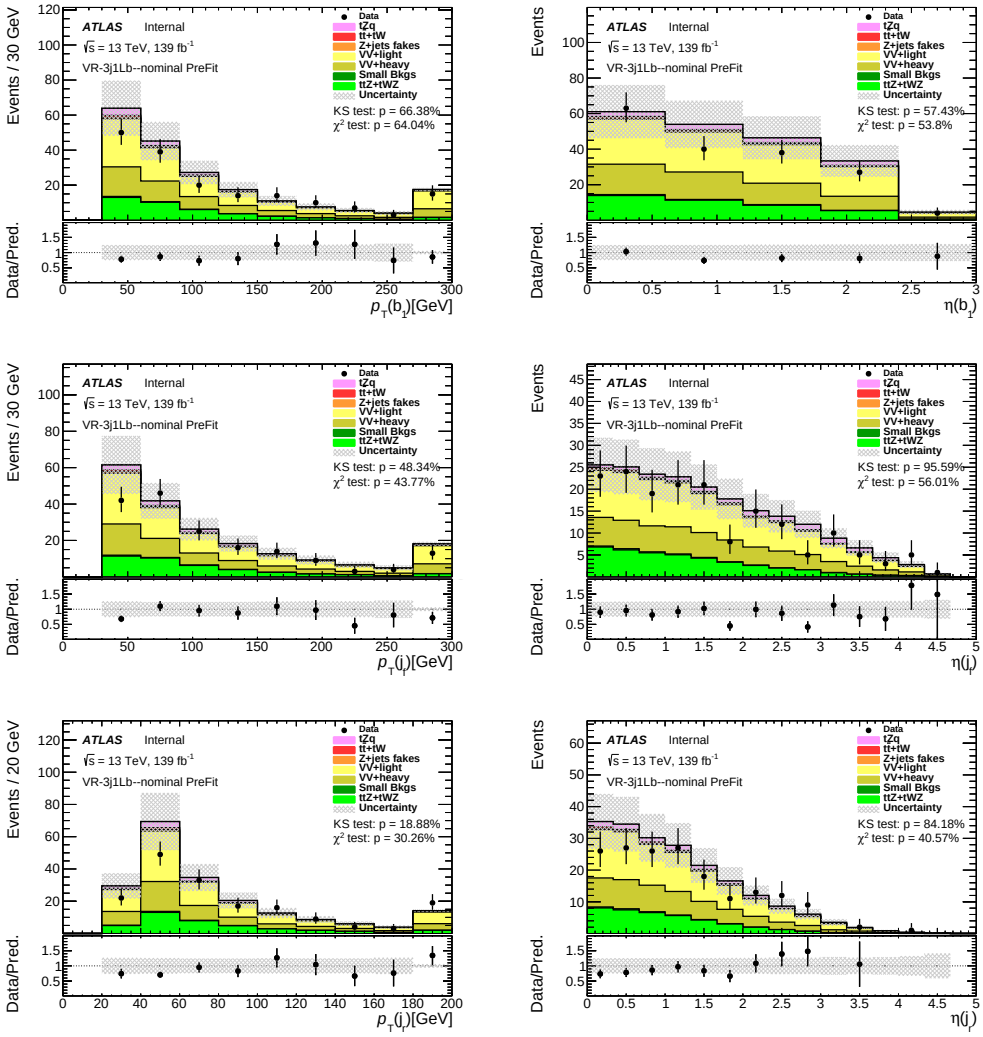


Figure C.5: Comparison of data and predictions for reconstructed jet-related quantities for events in the 3j1Lb VR. The uncertainty shown is the backgrounds' modeling uncertainty.

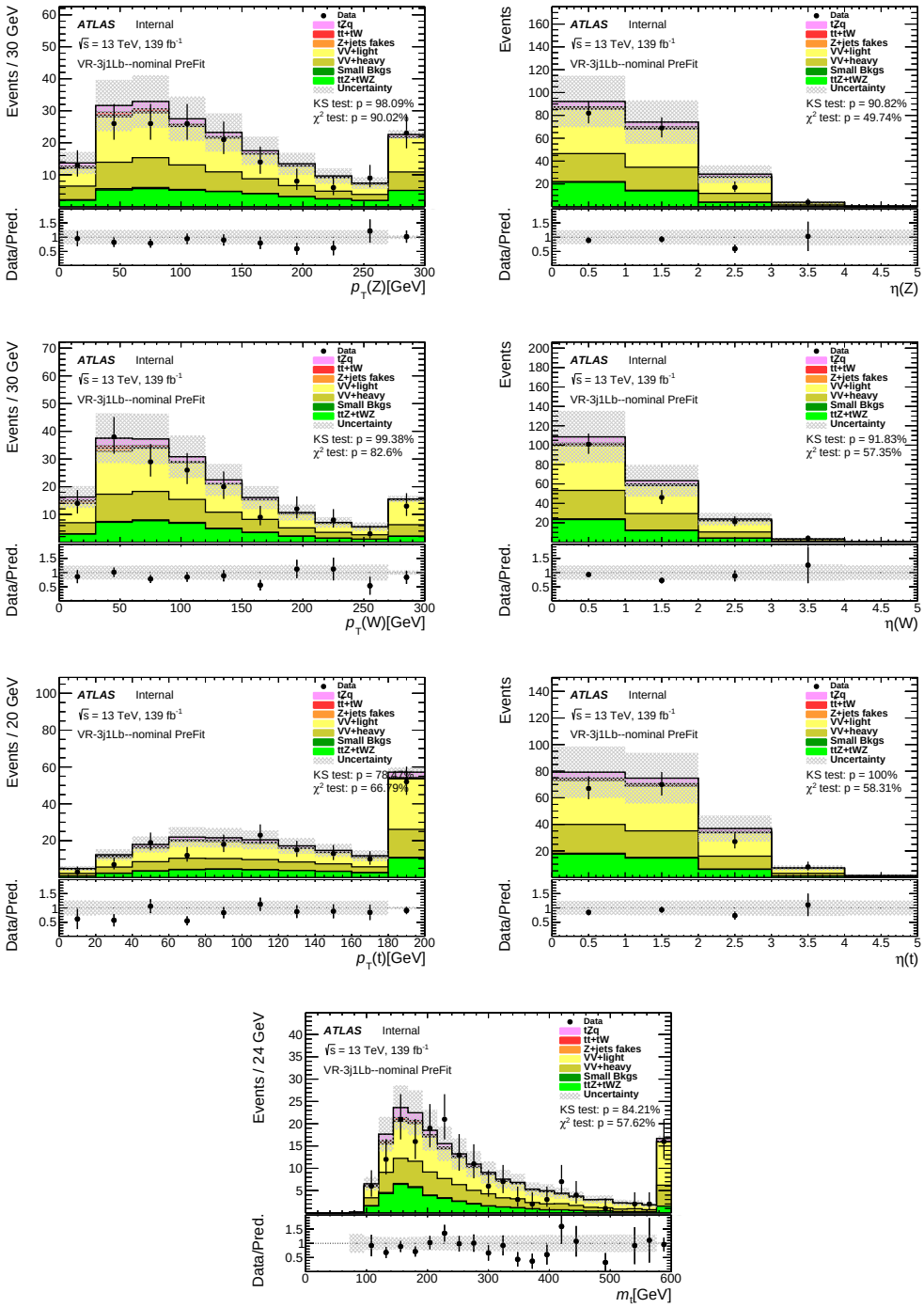


Figure C.6: Comparison of data and predictions for reconstructed event-related quantities for events in the 3j1Lb VR. The uncertainty shown is the backgrounds' modeling uncertainty.

Appendix D

b-jet Replacement Validation Plots

To validate the predicted shape of the b-jet replacement method, the most relavent variables to the neural network as well as the relevant variables to the synthetically generated lepton are compared to data in relevant regions of phase space with inhanced contribution from fake leptons.

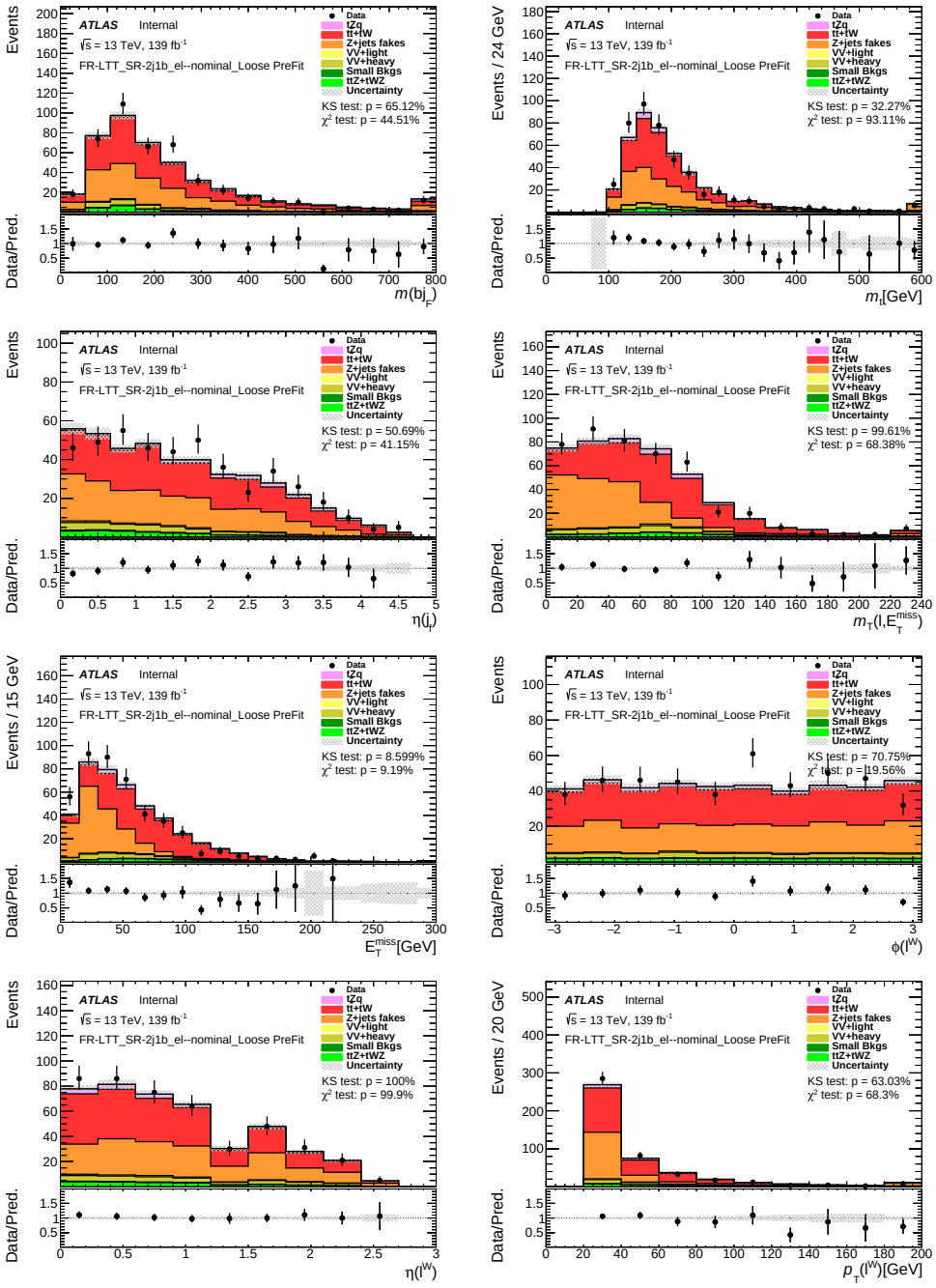


Figure D.1: Comparison of data and MC predictions for reconstructed electron events in the SR-2j1b-LTT.

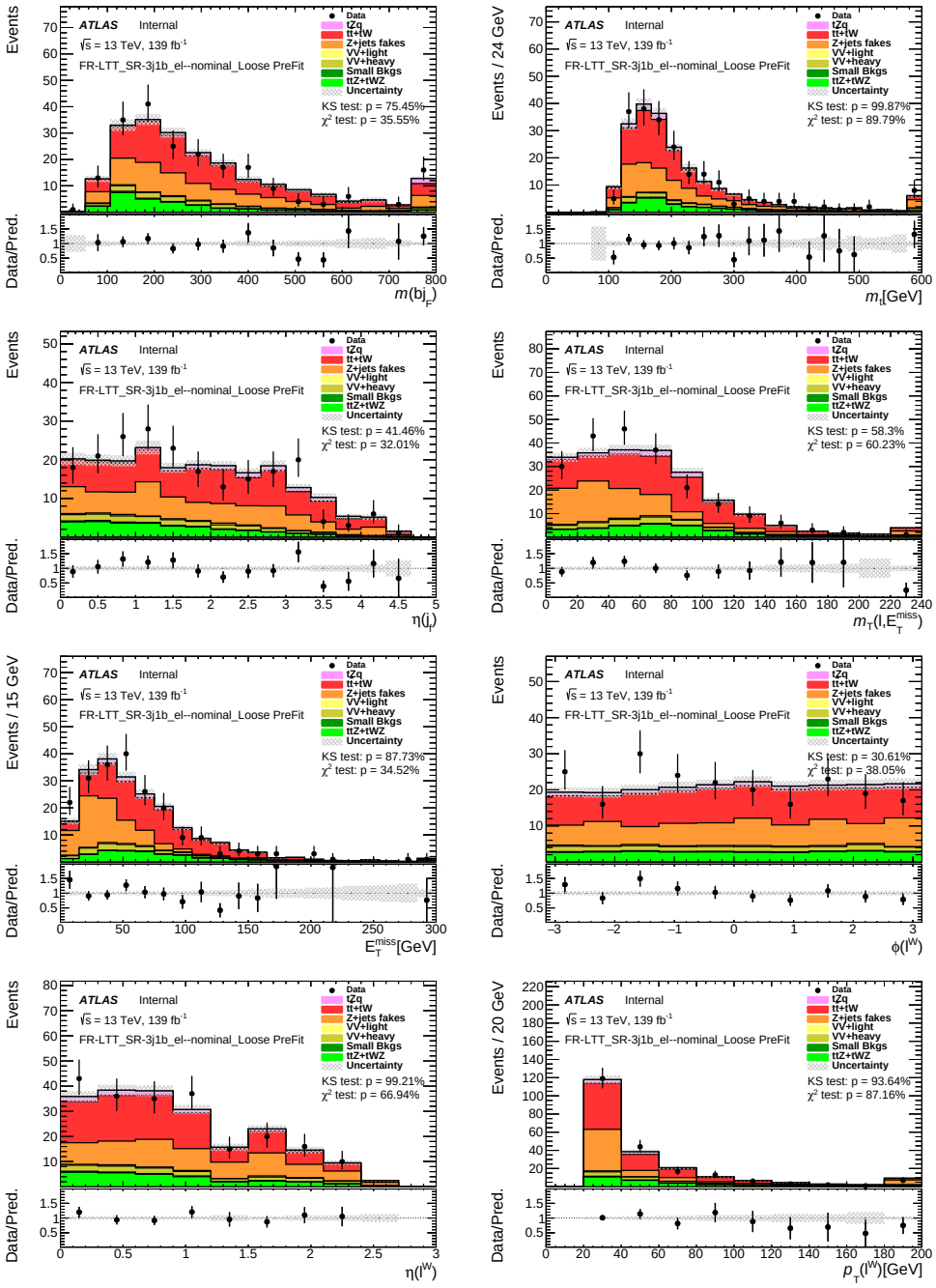


Figure D.2: Comparison of data and MC predictions for reconstructed electron events in the SR-3j1b-LTT.

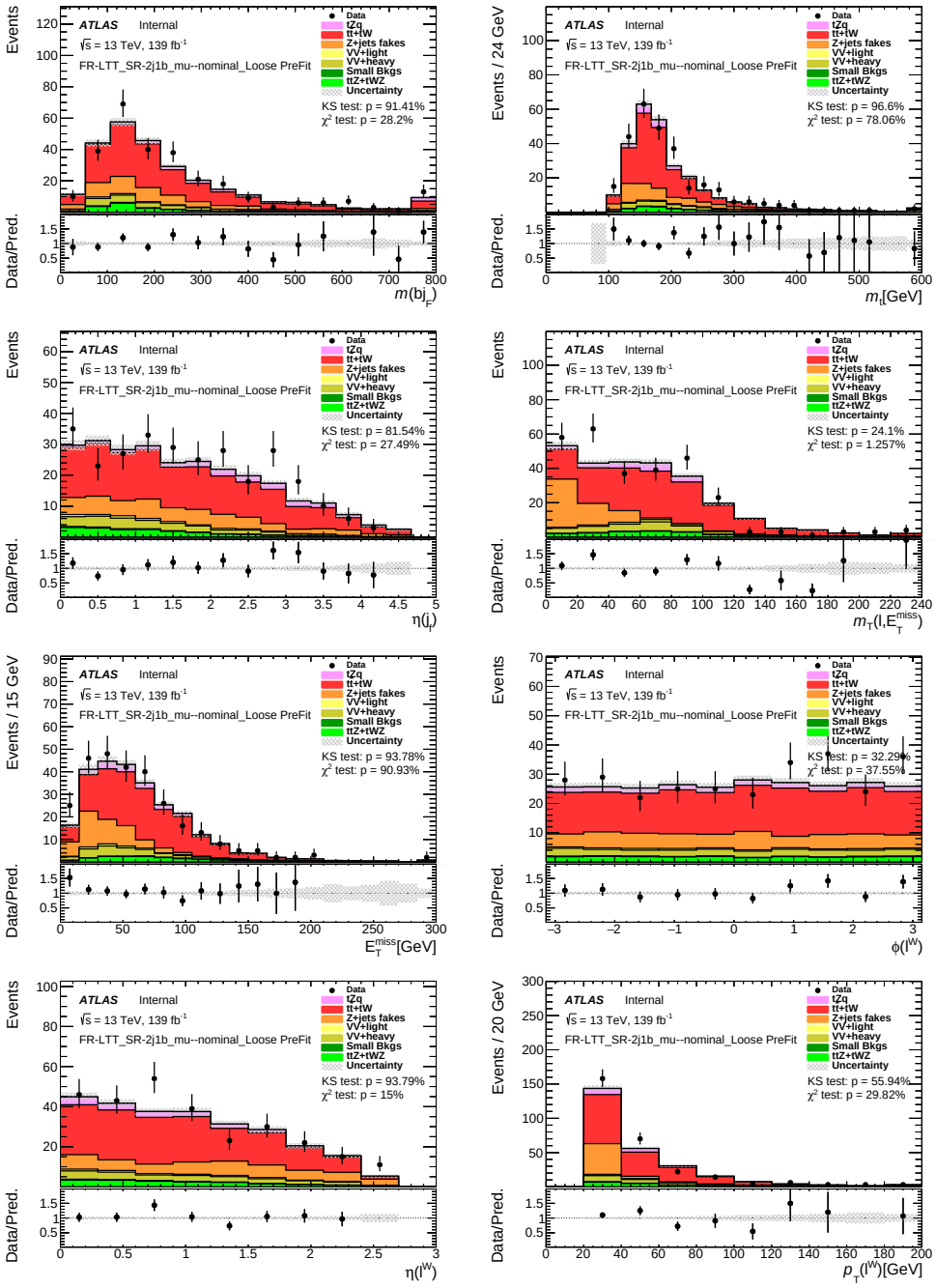


Figure D.3: Comparison of data and MC predictions for reconstructed muon events in the SR-2j1b-LTT.

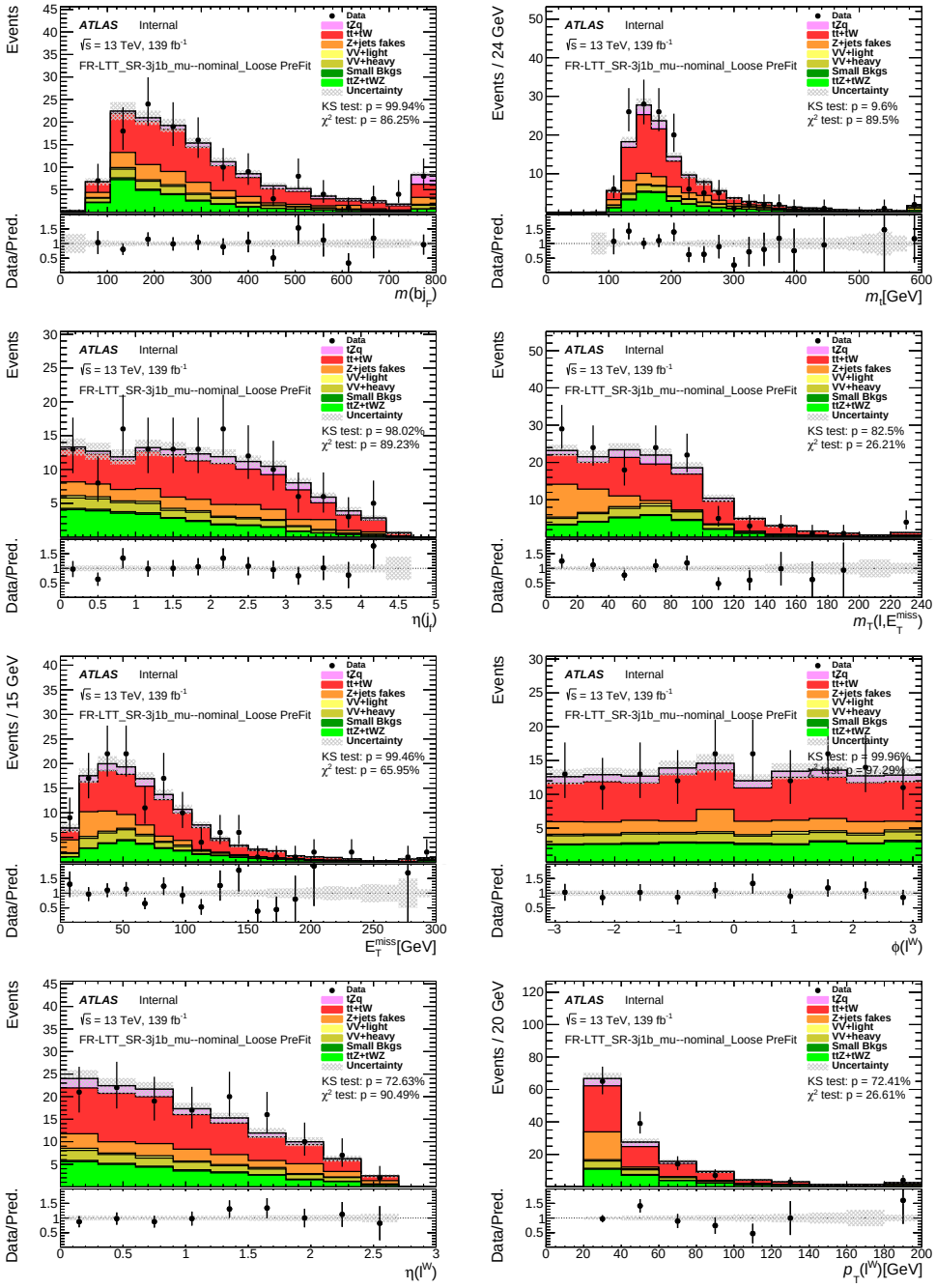


Figure D.4: Comparison of data and MC predictions for reconstructed muon events in the SR-3j1b-LTT.

Appendix E

Supplemental Variable Definitions

Further definitions of the input variables of the neural networks.

Transverse mass : The invariant mass of two or more objects only considering the transverse components of the input vectors.

***b*-tagging score :** The $b-$tagging algorithm for this analysis categorizes jets into 5 discrete bins that are separately calibrated. Each bin represents a different working point. The nominal working point for this analysis is 70%, which inclusively contains the 60% working point bin. To which bin a jet belongs provides a bivariate that can be used to discriminate against backgrounds with light jets.

Electric charge of lepton : The electric charge of a lepton can easily be inferred from the direction of curvature of the particle's track through the inner detector due to the magnetic field. Charge flips, an instance of a lepton emitting a hard photon that then has an energetic daughter lepton of opposite charge, is not considered and are expected to be negligible.

Appendix F

Fit Results Material

The profiled likelihood curve as a function of the POI is given in Fig. F.2. The pull distribution for all nuisance parameters in the fit are given in Fig. F.2.

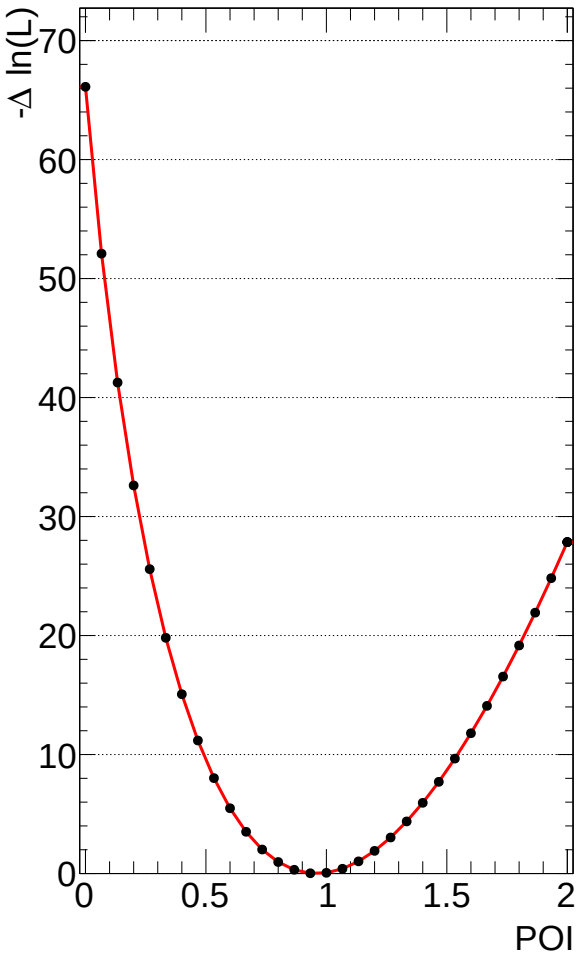


Figure F.1: The profiled likelihood curve as a function of the POI.

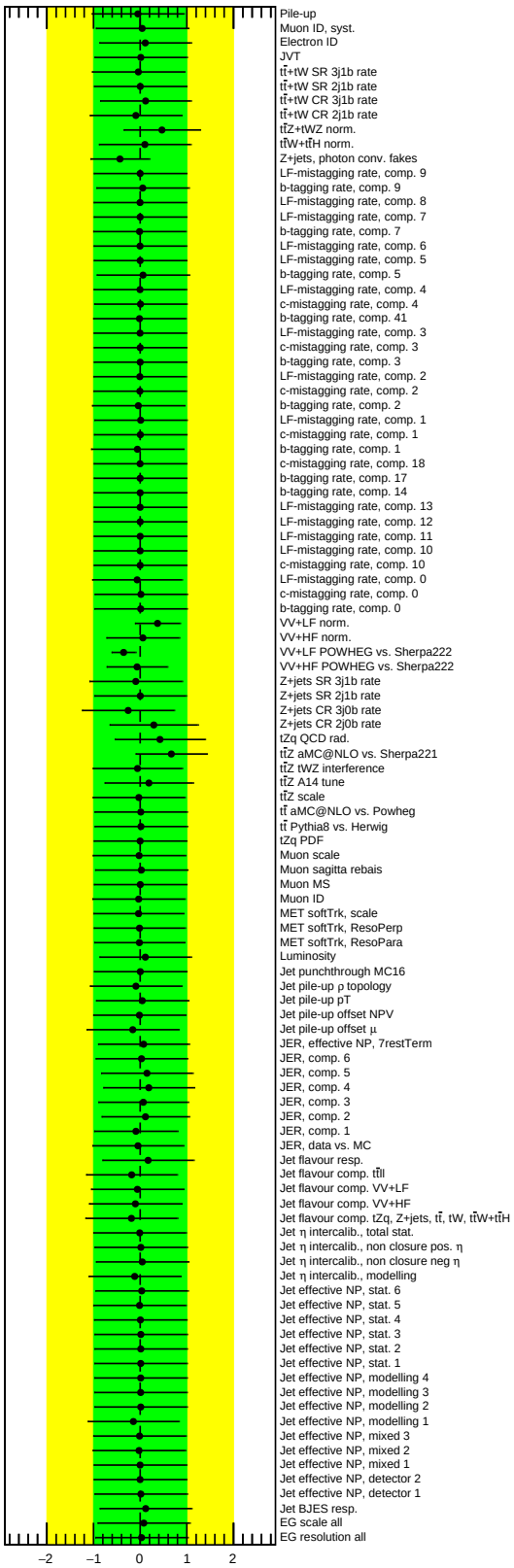


Figure F.2: The pull distributions of all systematic uncertainty parameters.